Radar-based Human Pulse Sensing

by
Michael Moheb Youssef Rizk Riad

A thesis
presented to the University of Waterloo
in fulfillment of the
thesis requirement for the degree of
Master of Applied Science
in
Electrical and Computer Engineering

Waterloo, Ontario, Canada, 2024
© Michael Moheb Youssef Rizk Riad 2024

Author's Declaration

I hereby declare that I am the sole author of this thesis. This is a true copy of the thesis, including any required final revisions, as accepted by my examiners.

I understand that my thesis may be made electronically available to the public.

Abstract

This thesis presents a novel approach where a superstrate is used to re-purpose a commercial off-the-shelf mm-wave 60 GHz radar by Infineon (BGT60TR13C) for near-field human pulse sensing. The superstrate is realized through low-cost printed circuit board (PCB) technology. it consists of couplers, a microstrip line, and a transverse slot in the ground plane. The superstrate was designed using full-wave electromagnetics (EM) simulations, along with a numerical-based model to predict the output of the radar in the presence of the superstrate. The superstrate was fabricated, and the combined sensor was tested on human participants. The preliminary measurement results match the expected theoretical pulse waveform. Hence, proving the feasibility of the proposed approach in near-field pulse sensing applications.

In comparison to the state-of-the-art pulse radar-based wearable sensors, the proposed sensor is more compact due to the superstrate protecting the radar from the detrimental effect of direct skin contact. Moreover, the sensing mechanism changed from capturing the phase changes for the range bin to monitoring the amplitude of the intermediate frequency (IF) spectrum peak. This was possible due to the enhanced signal-to-noise ratio (SNR).

The measured pulse waveforms were compared to a commercial-grade electrocardiogram (ECG) from Frontier. There was an excellent agreement, particularly in the period and timing of the pulses. Therefore, the proposed sensor is feasible for heart rate monitoring and heart rate variability.

Moreover, computer-aided-design-software (CAD)-generated digital twins have shown potential in generating datasets that could be fed to machine learning algorithms for detection and classification. This thesis demonstrates the feasibility of using the Shooting and Bouncing Ray method (SBR+) simulation to model pulse sensing using a commercial mm-wave radar. The time-domain reconstructed pulse waveforms had very good agreement with the input waveform, hence, this demonstrates the feasibility of using mm-wave radars for pulse sensing and the potential of using digital twins for generating diverse datasets to train radars on the signatures of various diseases and health conditions.

Acknowledgments

I would like to express my profound gratitude to my mentors, Prof. Raafat Mansour, and Prof. George Shaker, for their invaluable assistance and guidance throughout my academic journey at The University of Waterloo. Their wisdom and constructive feedback significantly improved the quality of my work.

I also wish to honor the memory of my late supervisor, Prof. Safieddin Safavi-Naeini, who passed away at the beginning of my journey.

My deepest thanks go to my biological and chosen family for their unwavering love, inspiration, and faith in my capabilities. Their steadfast support and understanding have been instrumental in my pursuit of this endeavor.

I extend my heartfelt thanks to my friends for their understanding, patience, and encouragement. Their companionship has made this journey not only academically fulfilling but also enjoyable and unforgettable.

Lastly, I wish to recognize all those who have contributed to my research, either directly or indirectly, particularly my friends and colleagues at the Wireless Sensors and Devices Lab. Your help, cooperation, and motivation have been crucial in the completion of this thesis.

I am grateful to all of you for being part of this significant chapter in my life.

Table of Contents

AUTHOR'S DECLARATION ii

ABSTRACT iii

ACKNOWLEDGMENTS iv

LIST OF FIGURES vii

LIST OF TABLES x

CHAPTER 1 INTRODUCTION 1

1.1 Motivation 1
1.2 Objectives 3
1.3 Thesis Outline 3

CHAPTER 2 LITERATURE REVIEW 6

2.1 Cardiac Cycle Physiological Basis 6
2.2 State-of-the-art Radar-based Cardiovascular Sensors 8
2.2.1 Contactless Sensing *9*
2.2.2 Wearable Sensing *11*

CHAPTER 3 SUPERSTRATE PCB DESIGN 15

3.1 Radar Module (Infineon BGT60TR13C) 15
3.2 Couplers & Bridge Design 19
3.3 Sensor Design 23
3.3.1 Ring Resonator *23*
3.3.2 Defective Ground Structure *29*

CHAPTER 4 RADAR-BASED SIMULATIONS 33

4.1 Shooting and Bouncing Ray Simulations 33
4.1.1 Simulation Setup and Verification *33*
4.1.2 Waveform Reconstruction *38*
4.2 Numerical-based Radar Simulations 42
4.2.1 Calculation Method *43*
4.2.2 Verification Tests *45*
4.2.3 Sensor Calculation *54*

CHAPTER 5 MEASUREMENT CAMPAIGN & RESULTS 60

5.1 Hardware Equipment & Experimental Setup 60
5.1.1 Frontier X activity monitor *60*
5.1.2 Manufactured Prototype *62*
5.2 Radar Measurements and Pulse Waveform Extraction 64
5.2.1 The Effect of the Superstrate on the Radar Response *64*
5.2.2 Pulse Waveform Measurement and Reconstruction *68*
5.2.3 Multiple Participant Study *73*

CHAPTER 6 CONCLUSION & FUTURE WORK 79

6.1 SUMMARY 79
6.2 ONGOING AND FUTURE WORK 79
6.3 PUBLICATIONS 80

REFERENCES 82

APPENDICES 87

APPENDIX A: MATLAB SCRIPTS 87
SBR+ Waveform Reconstruction 87
Numerical-Based Simulations 89
Measurements post-processing 91

List of Figures

Figure 1-1 A graphical overview of the proposed sensor including the radar module, and superstrate. The superstrate consists of two patch antenna couplers connected with a microstrip line with a slot in the ground plane. The fringing fields of the slot would be the sensor for the skin displacement due to the pulse. The PCB size is 40.68 x 25.41 mm^2, and the slot (sensor) size is 0.14 x 1.43 mm^2..... 4
Figure 1-2 Flow Chart Summary for the contributions in this thesis. 5
Figure 2-1 (a) Blood flow through the human body [22] (b) Cardiac conduction system for regulating heartbeat [22]. 9
Figure 2-2 The setup proposed in [6], where the radar module adheres to the chest. 12
Figure 2-3 The experimental setup presented in [7], shows (a) the radar assembly attached to the participant's wrist, and (b) the tonometer placed on the radial artery for ground truth.... 13
Figure 2-4 The experimental setup presented in [8] shows the radar module attached to the left wrist and the ground truth device on the right. 14
Figure 3-1 The Radar PCB (a) Back view (die), (b) Front view (antennas) [29], with its small size of 6.5 x 5.0 x 0.9 mm^3. 16
Figure 3-2 3D encrypted model of BGT60TR13C as provided by Infineon in HFSS. 16
Figure 3-3 Simulated S-parameters of the radar module across the operation frequency band before introducing the superstrate and SUT. 17
Figure 3-4 Simulated far-field 3D radiation pattern of the Tx antenna of the radar module at 60 GHz before introducing the superstrate and SUT. 18
Figure 3-5 X-Ray of the radar module showing the antenna structure including surrounding vias, slot line feeding, and the input microstrip line with matching stub [33]. 19
Figure 3-6 Mesh View on the top surface of the 3D HFSS model provided by Infineon. 19
Figure 3-7 Other attempts of using PCBs as sensing mechanisms alongside (a) radars [9], and (b) Wi-Fi access points [10]. 20
Figure 3-8 The proposed sensor architecture. 20
Figure 3-9 A sample 3D model of the proposed architecture. 21
Figure 3-10 Couplers design phase. 22
Figure 3-11 Bridge design phase; (a) Design, (b) Field power flow on the bridge. 22
Figure 3-12 The transmission coefficient between Tx and Rx2 w/ & w/o the bridge. 23
Figure 3-13 Proposed split ring resonator sensor. 24
Figure 3-14 S21 (magnitude and phase) of the resonator shown in Figure 3-13. 25
Figure 3-15 The transmission coefficient between the transmitter and receiver of the radar at different stages in the sensor design. 25
Figure 3-16 The field configuration on the bridge, SRR, and sensing region. 26
Figure 3-17 The model for the skin layer and pulse box. 27
Figure 3-18 The reference displacement waveform described by (3-1). 27
Figure 3-19 The transmission coefficient vs. Frequency for different time points. 28
Figure 3-20 The value of the transmission coefficient at 58.75GHz compared to the input reference waveform. 28
Figure 3-21 Proposed defective ground structure sensor. 29
Figure 3-22 The response of the sensor before introducing the sample. 30

Figure 3-23 The transmission coefficient vs Frequency for different time points (t, from 0 to 1s, with a step of 0.1s). 31
Figure 3-24 The (a) magnitude, (b) phase; of the transmission coefficient at 62.7 GHz compared to the input reference waveform. 31
Figure 3-25 The Phase of the transmission coefficient at 62.7 GHz after tightening the convergence criteria. 32
Figure 3-26 The effect of the varying dielectric properties of the skin on the performance of the sensor. The legend shows the values of $\boldsymbol{\varepsilon'}$ / $\boldsymbol{\sigma}$ respectively. 32
Figure 4-1 The result of the calibration large signal test case showing (a) Range, and (b) Doppler Velocity as a function of time. 35
Figure 4-2 The result of the reduced displacement calibration test case showing (a) Range, and (b) Doppler Velocity as a function of time. 36
Figure 4-3 The result of the pulse waveform test case showing (a) Range, and (b) Doppler Velocity as a function of time. 36
Figure 4-4 The setup for the pulse SBR+ simulation, showing the hand model, and radar beam pattern. The red triangle represents the oscillating object that corresponds to the pulsating radial artery. 37
Figure 4-5 The result of the pulse on wrist test case showing (a) Range, and (b) Doppler Velocity as a function of time. 37
Figure 4-6 The result of the pulse on wrist test 1 cm away from the skin case showing (a) Range, and (b) Doppler Velocity as a function of time. 38
Figure 4-7 Imported data from HFSS showing power vs velocity & time. 38
Figure 4-8 The Detected 20 Contours, 10 on each side of the zero-velocity bin. 39
Figure 4-9 Reconstructed velocity plot after DC offset removal. 40
Figure 4-10 Reconstructed displacement waveform obtained from integration of velocity with the minimum set to zero. 40
Figure 4-11 Reconstructed displacement waveform after applying curve fitting. 41
Figure 4-12 Comparison between the reconstructed and original displacement waveform after scale calibration. 42
Figure 4-13 Comparison between the reconstructed and original displacement waveform with two different maximum distension while maintaining the same scaling factor. 42
Figure 4-14 An overview of the general system architecture of an FMCW radar, the highlighted portion represents the Tx/Rx antennas and target that could be represented by the S-parameters. 44
Figure 4-15 The (a) spectrogram, and (b) spectrum; of the generated Tx chirp. 45
Figure 4-16 Circuit diagram of a transmission line with length L terminated by a short circuit. 46
Figure 4-17 The (a) spectrogram, and (b) spectrum; of the calculated Rx chirp for L=200 meters. 48
Figure 4-18 Spectrum of the calculated IF signal for the shorted transmission line test case at (a) L=200 meters, (b) L=400 meters, (c) L=600 meters. 49
Figure 4-19 The (a) spectrogram of the Rx, and (b) spectrum of the IF; signals for the mismatched transmission line test case showing multiple reflections with decaying amplitudes. 50

Figure 4-20 The (a) schematic, and (b) calculated spectrogram of the Rx signal, for the bandpass filter test case. 51
Figure 4-21 Spectrum of the calculated IF signal for the bandpass filter test case at (a) L=1 mm, and (b) L=100 meters. 52
Figure 4-22 The (a) 3D-model, (b) spectrogram of the Rx signal, and (c) spectrum of the IF signal; for the bare radar test case. 53
Figure 4-23 (a) 3D model of the radar w/plate test case, and The IF spectrums with the plate at (b)12 mm, (c) 25 mm, and (d) comparison with the bare radar. 55
Figure 4-24 The Spectrum for the IF signal w/ & w/o different superstrate elements. 56
Figure 4-25 (a) The 3D model of the proposed DGS superstrate including the skin layer and pulse box. (b) The amplitude of the IF spectrum at different slow time points, and (c) The amplitude of the IF spectrum peak compared to the input displacement waveform. 58
Figure 4-26 A comparison between the (a) S-parameters, and (b) IF spectrum in the response of the superstrate vs bare radar in response to the pulse stimuli. 59
Figure 5-1 Frontier X2 health monitor by Fourth Frontier [47]. 61
Figure 5-2 The definition of R-R Interval in ECG [49]. 61
Figure 5-3 Photograph of the radar PCB including the USB evaluation board. 62
Figure 5-4 Layout of the PCB superstrate sent for fabrication. 63
Figure 5-5 Layout of the solder mask cut-outs relative to the slot. 63
Figure 5-6 3D Model of the PCB standoff and mounting bracket. 64
Figure 5-7 A photograph of the assembled prototype. 64
Figure 5-8 Comparison between the raw output of the radar before and after the introduction of the superstrate. 66
Figure 5-9 The measured IF spectrum after mean removal w/ & w/o superstrate. 66
Figure 5-10 A comparison between the response of the radar before and after contact with the skin. 67
Figure 5-11 (a) the amplitude of the peak for the pulse measurement on the wrist and (b) the corresponding spectrum of the signal obtained in (a). 69
Figure 5-12 Measured pulse signal compared to the corresponding ECG ground truth for PT#1. 70
Figure 5-13 The power of the received signal at 61.125 GHz compared to the corresponding ECG ground truth for PT#1. 71
Figure 5-14 The measured pulse waveform for PT#1 using three different samples at different frequencies; (a) 60.34/30, (b) 60.5/32, and (c) 62.6/59; GHz/Sample. 72
Figure 5-15 A comparison between the performance of the sensor at different locations on the wrist for PT#1. 73
Figure 5-16 The two-finger technique used in locating the pulse on the wrist [56]. 74
Figure 5-17 Measured pulse signal compared to the corresponding ECG ground truth for (a) PT#2, and (b) PT#3. 75
Figure 5-18 The detected peaks in the (a) ECG and (b) Pulse waveforms for PT#2. 76
Figure 5-19 The error distribution of the measured pulse against its ECG benchmark for PT#2, and PT#3. 77
Figure 5-20 Measured pulse signal compared to the corresponding ECG ground truth for PT#4 as an example of a poor signal-to-noise ratio measurement. 78

List of Tables

Table 4-1 Input and Calculated Radar Parameters for the SBR+ Simulation. 34
Table 4-2 HFSS simulation parameters. 57
Table 5-1 Radar Configuration in Measurements. 65
Table 5-2 Summary of the heart rates obtained in the experiment. 76

Chapter 1

Introduction

1.1 Motivation

The escalating prevalence of cardiovascular diseases, which are leading causes of mortality and disability globally, underscores the growing need for effective monitoring of the heart. This need has been further amplified by the COVID-19 pandemic, given emerging evidence of its potential to compromise heart function, particularly among older adults and those with pre-existing health conditions [1].

Cardiovascular diseases (CVDs) are a significant health concern worldwide. They are the leading cause of death globally, with an estimated 17.9 million people dying from CVDs in 2019, representing 32% of all global deaths [2]. More than half a billion people around the world continue to be affected by cardiovascular diseases, which accounted for 20.5 million deaths in 2021 [3].

In Canada, heart disease is the second leading cause of death [4]. According to 2017–2018 data from the Canadian Chronic Disease Surveillance System (CCDSS), about 1 in 12 (or 2.6 million) Canadian adults above the age of 20 live with diagnosed heart disease [4]. Every hour, about 14 Canadian adults ages 20 and over with diagnosed heart disease die [4]. However, there has been a decline in the number of Canadian adults newly diagnosed with heart disease from 217,600 in 2000–2001 to 162,730 in 2017–2018 [4]. The death rate, or the number of deaths per 1,000 individuals with a known heart disease, has decreased by 21% [4]. These statistics highlight the global and national impact of cardiovascular diseases and the importance of continued efforts in prevention and treatment.

Traditional vital sign (VS) measurement techniques, such as electrocardiograms (ECG) and spirometry, present several challenges. These include their complexity, the discomfort they may cause due to the use of adhesive or pressure, their reliance on patient cooperation, and

their inability to provide continuous, non-invasive measurements of heart rate (HR), and heart rate variability (HRV).

Vital signs monitoring using radars is nothing new, however, most of the work in this area focuses on remote vital signs monitoring [5]. This means that radar is fixed somewhere, and it can extract information like heart and breathing rate from the reflections coming from an individual's torso. Although many works in literature verified the feasibility of remote monitoring, it is usually applied in very controlled environments where a limited number of individuals are present as well as limited chaotic motion of a real-world environment. Any general motion of the individual or the surroundings can result in noise that may dominate an already weak heart rate signal [5].

Radar-based VS monitoring offers a promising alternative and has been recently used for wearable [6], [7], [8]. In [6], a radar placed as a wearable belt was used to measure the breathing and heart rate. In [7], [8], a wrist wearable radar was proposed for pulse monitoring. However, the radar module was elevated from the surface of the skin for a distance of 1 cm in [7], and 3 mm in [8] to allow for quasi-near-field sensing, resulting in an overall bulky design despite the radar module itself being compact.

There were other attempts for using printed circuit board (PCB) sensors along with off-the-shelf devices such as radars [9], and Wi-Fi access points [10]. In [9], [10], a resonator-based sensing PCB was connected using cables/connectors. However, this was only feasible due to the low frequency of operation (2.4 GHz). In contrast, wired connections are not feasible in mm-wave sensors as they would require costly cables and connectors to minimize losses. Moreover, it would require custom radar modules with bulky cable connections, thus, unsuitable for integration into wearable sensors.

In this work, we present a similar implementation for the concept presented in [9], [10]. However, the connection between the radar board and the sensing circuit would be based on near-field capacitive coupling between the transmitter and receiver antennas of the radar and the corresponding pair of coupling antennas on a suspended superstrate as illustrated in Figure 1-1. This implementation can be highly compact; therefore, it can be easily integrated into wearables. Figure 1-1 presents an overview of the proposed sensor including its placement on the wrist and the overall design of the superstrate. Figure 1-1 also shows the expected dual

harmonic pulse waveform as described in [7]. Furthermore, the radar module is placed just 1.2 mm from the surface of the skin, hence the overall sensor package is compact. Moreover, the superstrate design features a ground plane preventing undesirable effects on the performance of the radar module antennas due to the proximity to the surface of the skin.

A high-level summary of the activities conducted within the scope of this thesis is shown in Figure 1-2.

1.2 Objectives

The primary objective of this thesis is to build a wrist-wearable radar-based sensor that can capture the heart pulse waveform. This sensor should yield results comparable to existing cardiovascular monitors such as electrocardiogram (ECG), or Photoplethysmography (PPG). The sensor would make use of an off-the-shelf commercially available radar module and repurpose it to near-field sensing using a proxy superstrate.

There are four main contributions to this thesis:

- Design a resonator-based superstrate that includes a sensing mechanism for a human pulse.
- Build and verify a mathematical model to map the S-parameter output from HFSS to realistic radar-based output such as beat frequency.
- Verify the feasibility of using the Shooting and Bouncing Ray method in HFSS in generating digital twins for pulse sensing applications.
- Conduct evaluation measurements for the designed sensor, comparing the results with the simulation results and comparing with a golden standard.

1.3 Thesis Outline

The layout of this thesis is organized as follows:

- Chapter 2: This chapter provides a review of the literature on radar-based cardio monitoring techniques with a focus on wearable vital signs.
- Chapter 3: This chapter introduces the superstrate as a sensing proxy concept. It includes a detailed description of the design process and presents two possible designs for the sensor.

- Chapter 4: This chapter introduces two simulation methodologies; electromagnetic and numerical-based algorithms to model the response of the radar under the pulse stimuli in the near field.
- Chapter 5: This chapter describes the experimental setup and results for the superstrate-adapted radar when tried on a human participant.
- Chapter 6: This final chapter offers concluding remarks as well as suggestions for future work to improve the system's performance.

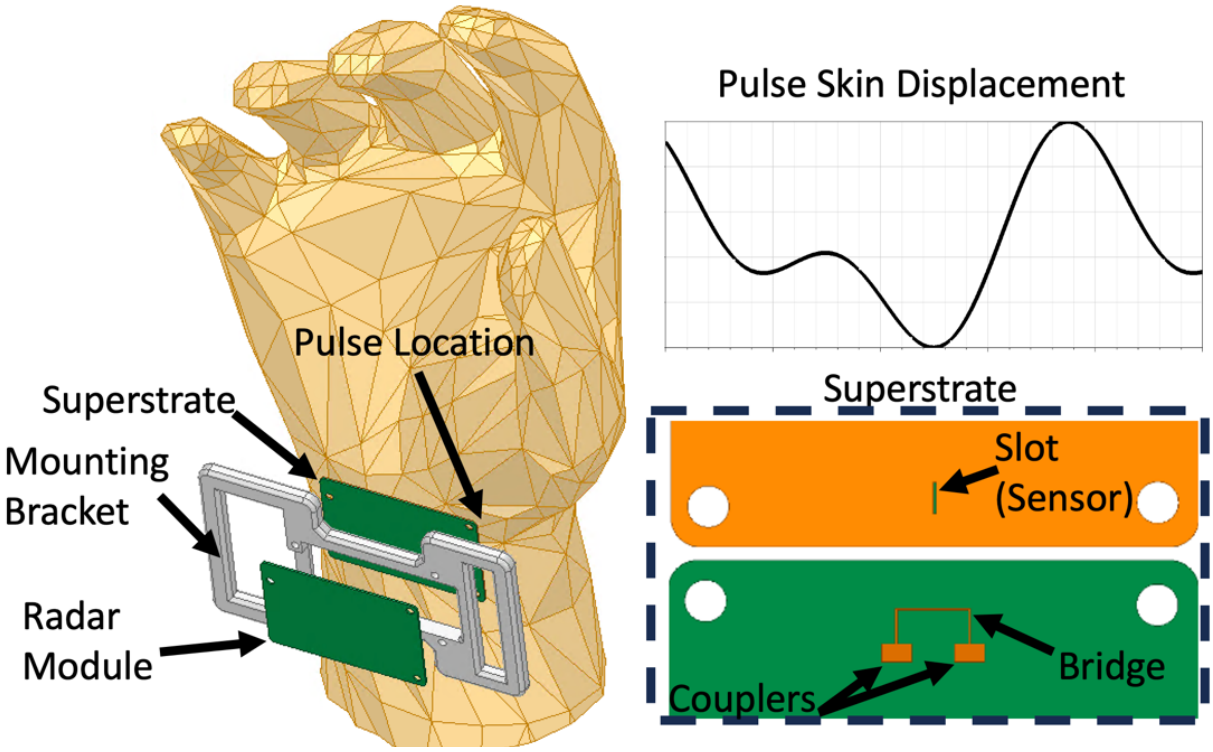


Figure 1-1 A graphical overview of the proposed sensor including the radar module, and superstrate. The superstrate consists of two patch antenna couplers connected with a microstrip line with a slot in the ground plane. The fringing fields of the slot would be the sensor for the skin displacement due to the pulse. The PCB size is 40.68 x 25.41 mm^2, and the slot (sensor) size is 0.14 x 1.43 mm^2.

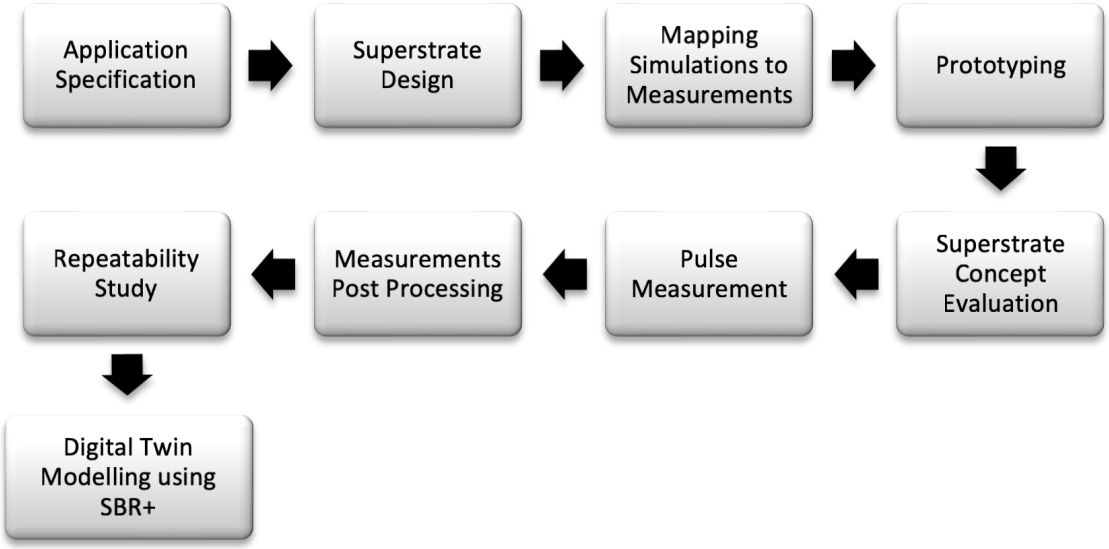


Figure 1-2 Flow Chart Summary for the contributions in this thesis.

Chapter 2

Literature Review

This chapter presents an overview of the current state-of-the-art radar-based sensors for vital signs monitoring with a focus on cardiac health monitoring such as heart rate or heart rate variability. Moreover, this chapter also provides a high-level summary of the different stages of the cardiac cycle.

2.1 Cardiac Cycle Physiological Basis

The heart is a vital organ that circulates the blood throughout the human body. A heartbeat is a complex process that involves a series of coordinated contraction and relaxation events of the cardiac muscles (myocardial cells) along with the closure of cardiac valves.

There are two distinct phases for a heartbeat: the diastole and systole [11]. In the diastole phase, the heart muscles relax resulting in the heart chambers getting filled with blood. Therefore, the diastole is often described as the resting phase of the cardiac cycle. In the systole phase, on the other hand, the cardiac muscles contract and pump the blood. First, the atria would contract pushing the blood into the ventricles this is followed by a forceful contraction of the ventricles to pump the blood to the rest of the body. It is also worth noting that each half of the heart is filled either oxygenated or deoxygenated depending on the destination as shown in Figure 2-1a.

The cardiac muscle activity is accompanied by electrical signals starting from the sinoatrial node in the right atrium as shown in Figure 2-1b. These electrical impulses prompt the muscles to contract, hence, the sinoatrial is also called the natural pacemaker of the heart. As these electrical signals propagate through the muscles, it is delayed by the atrioventricular node located between the atria as shown in Figure 2-1b. This delay allows efficient blood transfer between the atria and ventricles. Moreover, there is an additional delay between the arterial and ventricular contractions as the signal passes through the *Bundle of His* down the septum

into the Purkinje fibers where it reaches the ventricles. In addition to the muscular contractions, the flow of blood through the heart is regulated by four valves: the tricuspid valve, the pulmonary valve, the mitral valve, and the aortic valve. The main function of the valves is to ensure that the blood flows in a single direction, thus, preventing backflow [11].

These electrical signals are the fundamental principle of operation for electrocardiogram (ECG) sensors as they can be detected using electrical leads on the surface of the skin. There are a total of 12 leads in a standard diagnostic ECG. However, a smaller number of leads can be used depending on the level of information required. For example, a 6-lead ECG would be sufficient to monitor cardiac activity during exercise, while a single-lead ECG is only good for temporary heart rate monitoring during emergencies [12]. ECGs are used to diagnose and measure various cardiac conditions such as arrhythmia, valve disorders, and heart failure [13] as they carry information about the timing and regularity of cardiac conduction [14].

After the blood leaves the heart, it embarks on a journey through the circulatory system. It is first pumped out of the left ventricle into the aorta, the largest artery in the body. From the aorta, the oxygen-rich blood travels into progressively smaller arteries, then arterioles, and finally reaches the capillaries. It is in the capillaries where the exchange of oxygen and nutrients for carbon dioxide and waste products occurs with the body's tissues. After this exchange, the now oxygen-depleted blood begins its return journey. It moves from the capillaries into venules, then veins, and finally into the two largest veins (the superior and inferior vena cava), which carry it back to the heart. However, it is possible to feel a pulse at the surface of the skin in areas where the arteries get closer to the skin such as the neck or wrist. This pulse is the pressure wave generated by the heart's contraction propagating through the arterial system. This wave is transmitted through the blood and the elastic walls of the arteries, reaching the peripheral arteries including the radial artery in the wrist [15].

Pulse wave analysis is a method that involves mathematically analyzing the arterial blood pressure waveform, which can estimate cardiac output (CO) continuously and in real-time [16]. The arterial blood pressure waveform is a complex signal determined by various physiological factors, including left ventricular stroke volume, aortic compliance, vascular resistance, and wave reflection phenomena.

These pulse wave analysis systems such as the VolumeView [17], or PiCCO [18] systems require an arterial catheter (commonly inserted in the radial artery) and are therefore referred to as “minimally invasive” methods. However, they may become unreliable in patients whose biometric (e.g., weight, height), demographic (e.g., age, sex), and hemodynamic data used for statistical calibration are not in the standard range of the underlying database or physiological assumptions of the pulse wave analysis system.

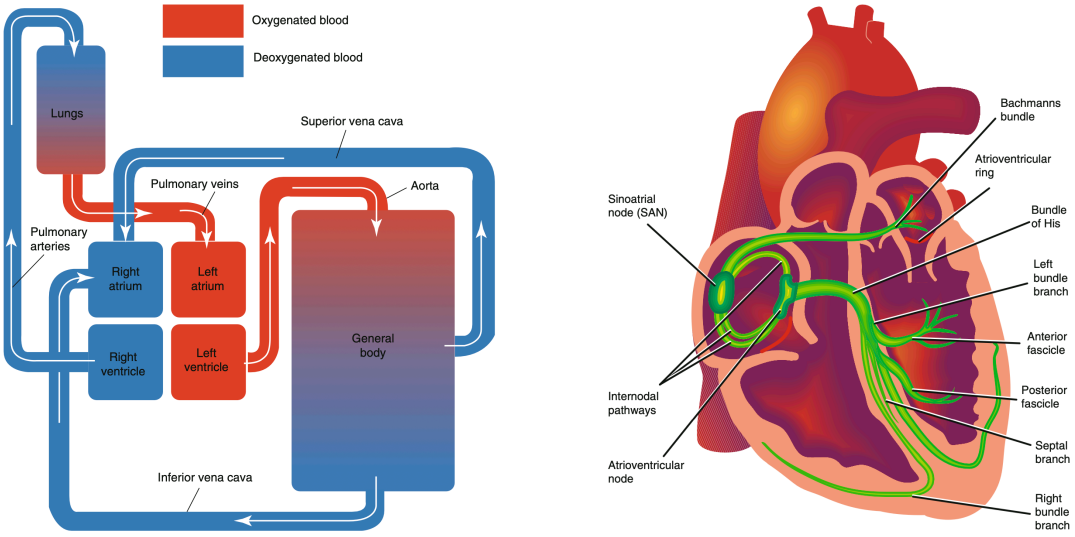
In addition to CO, pulse wave analysis allows for assessing dynamic cardiac preload variables, i.e., pulse pressure variation and stroke volume variation related to positive pressure ventilation [19]. In patients with sinus rhythm and controlled mechanical ventilation with a tidal volume of at least 8 ml/kg predicted body weight, pulse pressure variation, and stroke volume variation can be used to predict fluid responsiveness (i.e., an increase in CO by fluid administration) [19].

So, while it’s not an ECG, pulse wave analysis can provide valuable real-time information about the cardiovascular system. However, it’s important to note that this method has its limitations and may not be suitable for all patients or conditions as it is also sensitive to other non-cardiac diseases [20].

The arterial pressure can cause small vibrations ranging from at the surface of the skin. In this work, we aim to use a mm-wave radar to detect and quantify the motion of the surface of the skin due to the arterial pulse to be used by health professionals for diagnosis. In [7], Johnson et al reported that the skin distension at the wrist ranged from 50 to 300 um in an internal study by Blumio (acquired by CardieX [21]). Moreover, they also reported that the width of this distension ranges from 0.5 to 3 mm [7].

2.2 State-of-the-art Radar-based Cardiovascular Sensors

Recently radio-frequency, microwaves, and mm-waves have attracted research attention to its potential use in biomedical sensors. Radar technology had sensing as its primary goal since its inception. However, the scope of radars was to sense macro-scale motions for aviation and automobile applications. This work makes use of radar technology for vital signs monitoring specifically cardiovascular health. In this section, we will present the state-of-the-art radar sensors segregated into two categories contactless, and wearable/contact.



(a) (b)

Figure 2-1 (a) Blood flow through the human body [22] (b) Cardiac conduction system for regulating heartbeat [22].

2.2.1 Contactless Sensing

Radars have been quite popular recently in vital signs monitoring, due to being unobtrusive. The majority of work in the literature in this area focuses on contactless or remote vital signs sensing, where the radar is placed somewhere in the room and the reflected signals from the human body are analyzed to extract the vital signs. Many radar modulation schemes can be used for vital signs sensing such as Pulsed radars, Continuous wave (CW), and Frequency Modulated Continuous Wave (FMCW). In terms of the simplicity of hardware implementation, CW radars are much simpler than FMCW radars [23]. However, FMCW radars offer the ability to detect the range and multiple targets while being simpler than pulsed radar modules [23]. Although CW radars have been used previously for vital signs monitoring, they are not adaptable to handle reflections from multiple objects, hence, they require a higher signal-to-noise ratio [23].

FMCW radars, on the other hand, change the frequency of the transmitted signal v.s. time and through the mixing of the transmitted and received signals, it is capable of separating reflections from different targets (at different ranges) into separate range bins through spectral

analysis of the intermediate frequency (IF) signal. The main principle of using FMCW vital signs monitoring is through the detection of the phase modulation in the IF peaks caused by micromotions of the human body due to vitals such as breathing or heart rate [23].

However, multiple challenges face FMCW radar-based vital sign remote sensors. First of all, is the relative position between the radar and the subject as a radar facing a subject face-on would observe a significantly higher radar cross-section (RCS) than the same radar observing the same subject from a side-view [23]. Hence, the ability to detect vital signs is hindered.

Another challenge that faces the accuracy of radar-based vital signs is random body movement (RBM) as they can have relatively similar signatures to the vital sign signatures, hence, traditional harmonic-based filtration techniques fail [23]. For example, if the person is not standing perfectly still but fidgeting back and forth, this could be interpreted as a breathing cycle due to the lack of ground truth. It is possible to account for random body motion using advanced post-processing techniques, for example, in [24], a two-step motion compensation algorithm used correlation and realignment in the range-azimuth map to account for larger movements, then eliminating small movements using smoothing functions. In [25], two radars were used simultaneously to measure vital signs and to compensate for the effects of body motion to an extent.

Although FMCW radars can, in principle, separate between multiple targets, the main specifications that handle this are the range, or azimuth (angle of arrival) resolution which determines the minimum distance that two targets could be separated. Many works in the literature claim to measure the vital signs of multiple targets in proximity by combining different measurements from range, azimuth, elevation, and Doppler velocity [26]. However, these techniques are quite limited when the targets start moving. Therefore, some researchers aim to detect if the participant(s) is moving, and only attempt to capture vital signs when the participant(s) are stationary [27].

In this work, the radar module is used as a wearable which solves many of the challenges that face contact-less vital signs sensing. The field of view (FOV) of the wearable radar is constant. Consequently, there is no need to account for changes in the relative position of the radar and the body. Moreover, the radar is usually not affected by generic random body movement except if the area under observation is directly moved. For example, a radar that is

mounted on the chest will not be affected by wrist motion and vice versa. However, it is worth noting that motion in the same area of interest may have an amplified effect.

However, other challenges affect wearable radars, mainly that an off-the-shelf radar module is meant to operate in free space. Consequently, direct contact with the skin represents a very harsh environment that can lead to unpredictable consequences. We will discuss some relevant examples of wearable sensors in the literature in subsection 2.2.2.

2.2.2 Wearable Sensing

In this work, the focus is primarily on a wearable cardiovascular sensor. Compared to contactless sensing, wearable sensing significantly reduces the effect of environmental noise from other objects or multiple targets due to two or more people within the radar's field of view (FOV). However, due to the proximity to the skin, wearable sensors can be described as near-field sensors where the radiated fields are not yet established. Hence, the sensing mechanisms need to be verified and adapted to accommodate this new environment. In this subsection, we will present the current state-of-the-art radar-based wearable vital signs sensors in the literature.

First, there has been previous work by our group to monitor the breathing and heart rate waveforms through a chest adhesive patch as shown in Figure 2-2. In their thesis [28], Abu-Sardnah *et al*. were able to detect the breathing rate accurately when regulated using a metronome that the participants were asked to follow. Moreover, they were able to measure the heart rate and heart rate variability with up to 95% accuracy when the participants held their breath [28]. However, the cardiac waveforms were found to be significantly weaker than the accompanying breathing signal [28]. Hence, it required a band-pass filter to cancel the effect of the breathing waveform [28]. Moreover, the acquired waveforms despite their correlation to the ECG ground truth in terms of repetition rate, don't resemble an existing diagnostic protocol and there is skepticism if the physiological interpretations presented in [28] are accurate.

In this work, the sensor is placed on the participant's wrist, hence, the effect of the breathing waveform is insignificant. This presents a natural trade-off between scope and accuracy, the proposed work would have a narrower scope in terms of the target application than the work

presented in [28], focusing primarily on cardiac waveforms. However, the obtained waveforms are held to a higher level of scrutiny as they are required to resemble the pulse waveform. Nonetheless, the proposed methodology of using PCB superstrates could be generalized to serve other goals such as breathing rates.

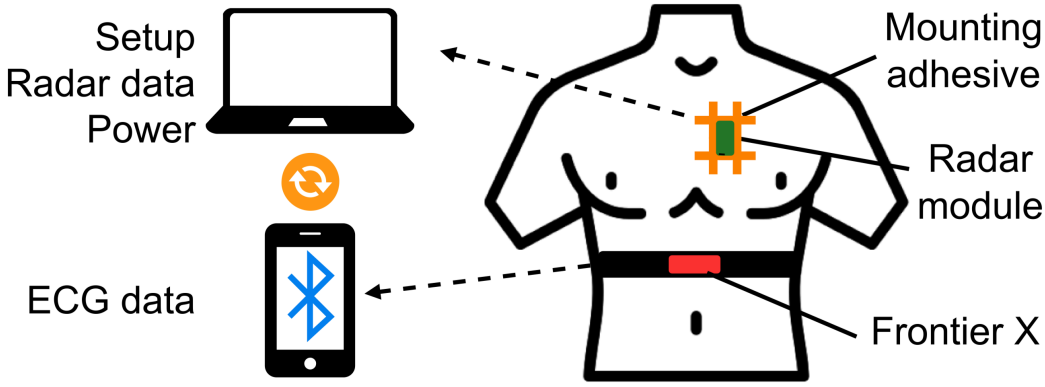
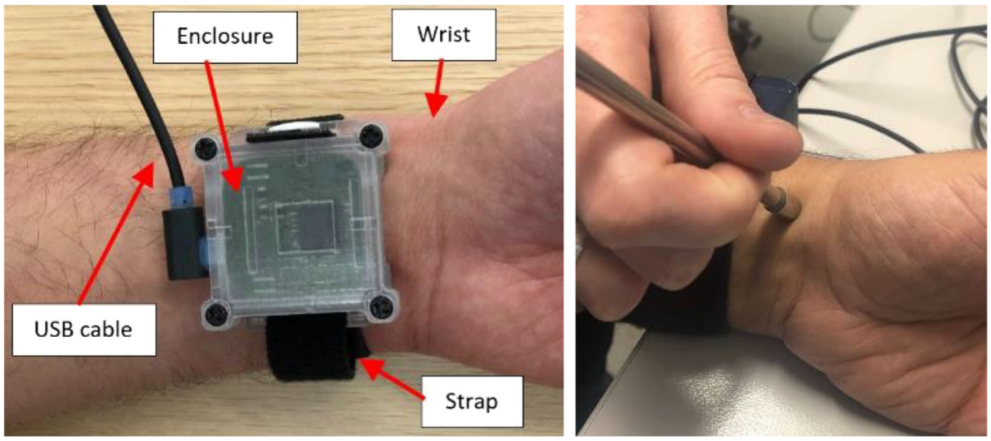


Figure 2-2 The setup proposed in [6], where the radar module adheres to the chest.

There were other successful attempts to measure placing a mm-wave radar on the wrist, especially in [7], [8]. In [7], Johnson et al place a 60 GHz mm-wave radar in a wrist wearable enclosure as shown in Figure 2-3a. Moreover, they used a tonometer (pressure sensor) placed by an expert user for the ground truth. The measured pulse waveforms had a high correlation to the ground truth for some participants. However, the radar was placed on 1 cm stand-offs from the surface of the skin to place the sensor in the radiative near-field (quasi near-field) [7]. As claimed in [7], this is to protect the radar from the unpredictable skin with the skin in the near-field reactive region. In Chapter 5, we will show the detrimental effect that direct skin contact has on the radar's operation. In this work, we use a PCB superstrate placed less than 1mm away from the antennas. The superstrate features a ground plane that shields the radar from unpredictable interactions with the skin surface, instead, the power is guided through a deterministic transmission line whose transmission coefficient is changed by the motion on the surface of the skin.



(a) (b)

Figure 2-3 The experimental setup presented in [7], shows (a) the radar assembly attached to the participant's wrist, and (b) the tonometer placed on the radial artery for ground truth.

In [8], researchers from Infineon proposed measuring blood pressure by capturing the pulse waveform using a 60 GHz radar module. The radar was held to the participant's wrist using a Velcro strap as shown in Figure 2-4. The distance between the radar module and the surface was 3 mm created by standoffs built into its 3D-printed enclosure. The measured waveforms had a good correlation with the ground truth for some participants while the radar captured only noise for others.

In [8], the authors highlighted the problem of using traditional FMCW techniques for displacement extraction in such proximity to the radar. The motion is only 3 mm away from the radar, while the first range bin is at 2.7 cm (dictated by the radar specifications such as bandwidth). They reported that this is a likely cause for a "**tremendous**" impact on signal quality [8]. This is because it assumes that the motion is around a much further away bin causing distortion.

In this work, we proposed using a PCB sensor on a superstrate as a proxy sensing mechanism for the pulse. This changed the processing from detecting the phase changes in the range bin to measuring the power changes in the superstrate's insertion loss due to the pulse. This is an attempt to circumvent the caveat described in [8]. Additionally, our radar module is placed just 1.2 mm from the surface of the skin (of which 0.5mm is the thickness of the superstrate itself), which is more than 50% improvement compared to the 3 mm presented in [8].



Figure 2-4 The experimental setup presented in [8] shows the radar module attached to the left wrist and the ground truth device on the right.

Chapter 3

Superstrate PCB Design

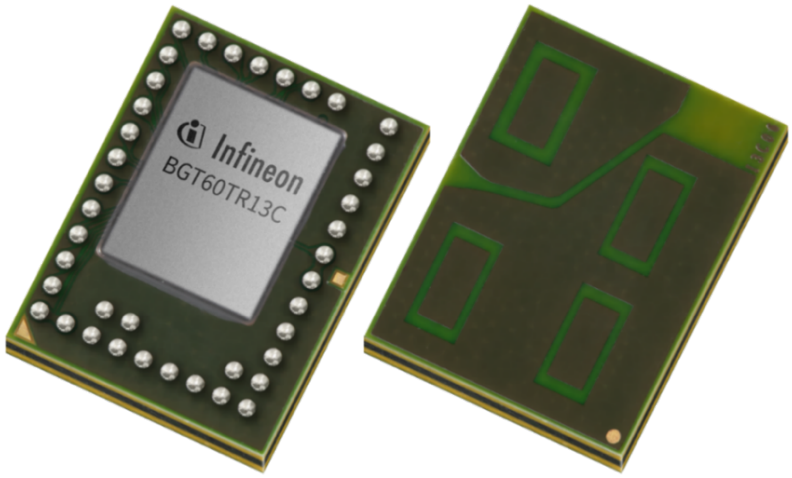
The hypothesis of this work is the use of a proxy for near-field sensing. One form of proxy is suspended printed circuit board (PCB) superstrates placed between the radar board and the sample-under-test (SUT). We opted to use a divide-and-conquer approach by dissecting the superstrate design into three phases; near-field-capacitive-couplers designed to maximize the power transfer between the radar board and the superstrate, a transmission-line-based bridge to transfer the power between the couplers and sensors, finally, the sensors themselves which would control the sensing mechanism/performance. In this chapter, we will explain the design process used for superstrate PCB that would be used in our experiments.

3.1 Radar Module (Infineon BGT60TR13C)

Although the design of the sensor component can be independent of the exact model of the radar module given that they operate in a similar frequency band. The backbone of the design process of the couplers and bridges is to have a relatively accurate 3D model of the radar board to properly design a near-field component. Consequently, we imported the 3D model of the 60 GHz frequency-modulated-continuous-wave (FMCW) radar module from Infineon (BGT60TR13C) [29] shown in Figure 3-1 into Ansys HFSS [30] as shown in Figure 3-2.

This radar module consists of one transmitting (Tx) and three receiving (Rx) antennas. It comes in a very small package (6.5 x 5.0 x 0.9 mm^3) [29] which makes it convenient for wearables integration. Moreover, it can consume very low power (<5 mW) [29] if configured properly. Thus, it is suitable for battery operation. Finally, Infineon product placement recommends it for vital signs monitoring as well as sub-millimeter motion detection [29]. It is worth mentioning that this radar module was integrated into the Google Pixel 4XL smartphone for gesture recognition also known as Project Soli [31]. Furthermore, as presented in Chapter

2, this radar module was also used to power multiple wearable pulse or blood pressure sensors in the literature [6], [8], [32].



(a) (b)

Figure 3-1 The Radar PCB (a) Back view (die), (b) Front view (antennas) [29], with its small size of 6.5 x 5.0 x 0.9 mm^3.

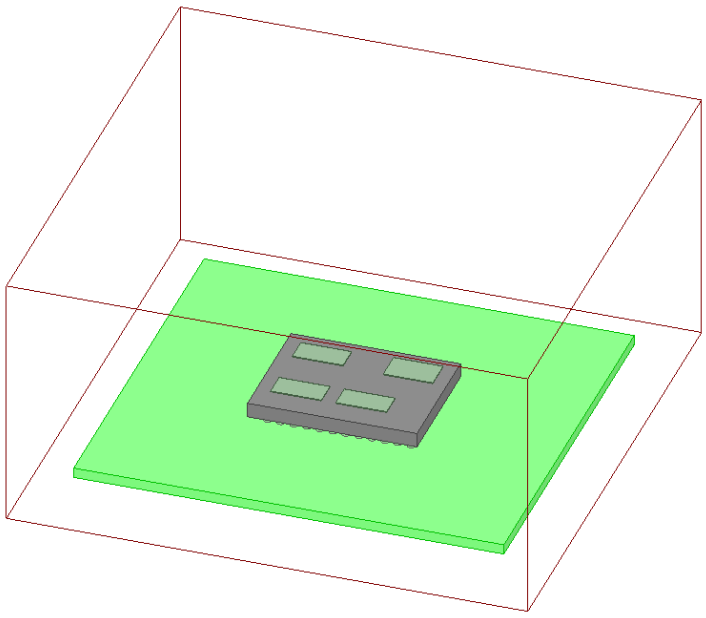


Figure 3-2 3D encrypted model of BGT60TR13C as provided by Infineon in HFSS.

After importing the model into Ansys HFSS v.2022R2, we ran a baseline simulation to understand the performance of the radar module under normal, ideal, and unaltered conditions. Some of the S-parameters are shown in Figure 3-3.

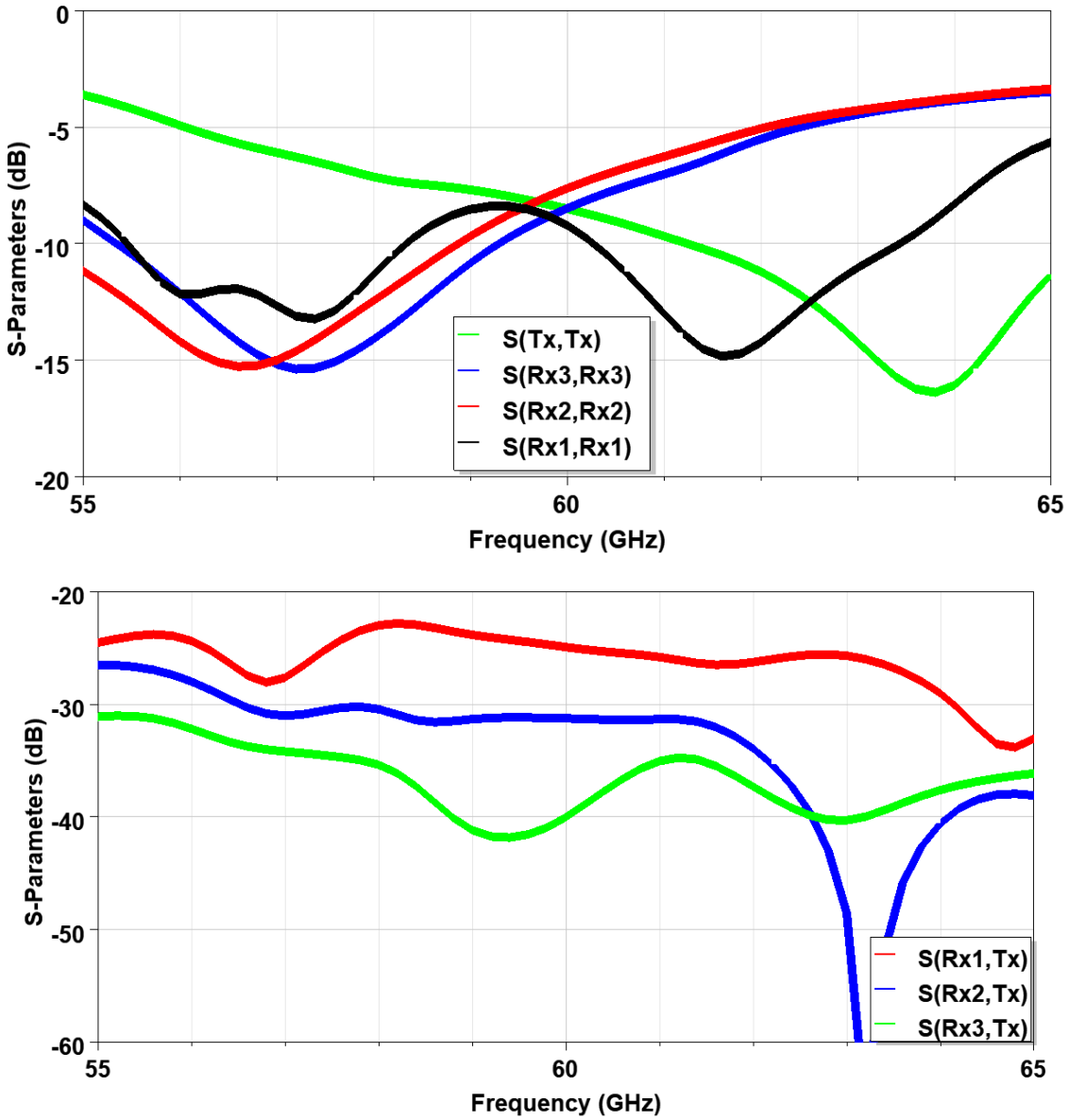


Figure 3-3 Simulated S-parameters of the radar module across the operation frequency band before introducing the superstrate and SUT.

Although the matching performance of the Tx, Rx2, and Rx3 antennas is not ideal, it is still operational especially since there might be additional matching components that were not

included in the model provided by Infineon. The isolation, on the other hand, shows great performance with at least 20 dB isolation between the Tx antenna and the Rx antennas across the frequency range. In this proposal, we would focus more on Rx2 compared to the other two receivers. Therefore, it is worth noting that it achieved 30 dB isolation at 60 GHz. Figure 3-4 shows the far-field radiation pattern, although it is not directly related to pulse sensing in the near-field, it can provide insight into how our proposed superstrate would impact the far-field performance of the radar module.

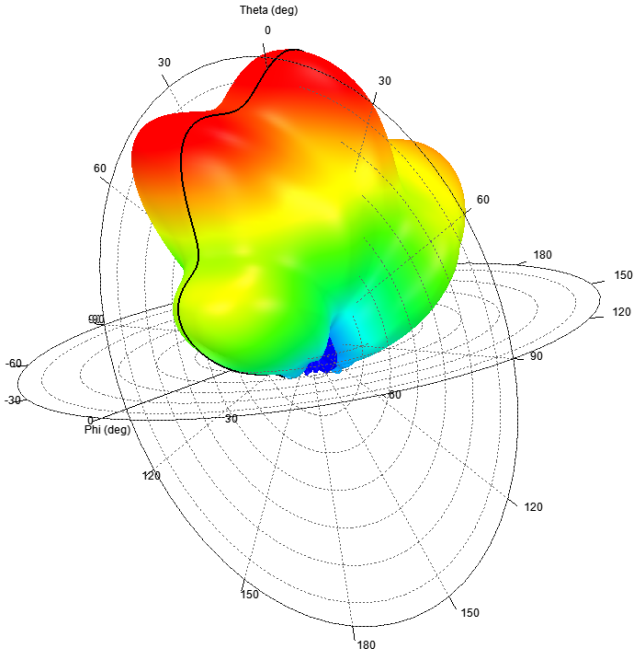


Figure 3-4 Simulated far-field 3D radiation pattern of the Tx antenna of the radar module at 60 GHz before introducing the superstrate and SUT.

To further understand the performance of the radar module antennas, we investigated its construction further. Since the 3D model provided by Infineon is encrypted, we were initially not able to observe the true geometry of the antennas, vias, and excitation instead we were limited to the details shown in Figure 3-2. In [33], the Yole group (formerly known as SystemPlus Consulting) conducted a reverse costing teardown of the radar module showing some X-rays as shown in Figure 3-5. Unfortunately, we are not able to verify which details were included in the model provided by Infineon. However, from the meshing shown in Figure

3-6, it is clear that at least the top layer in the model provided by Infineon accurately represents the corresponding physical features of the radar module.

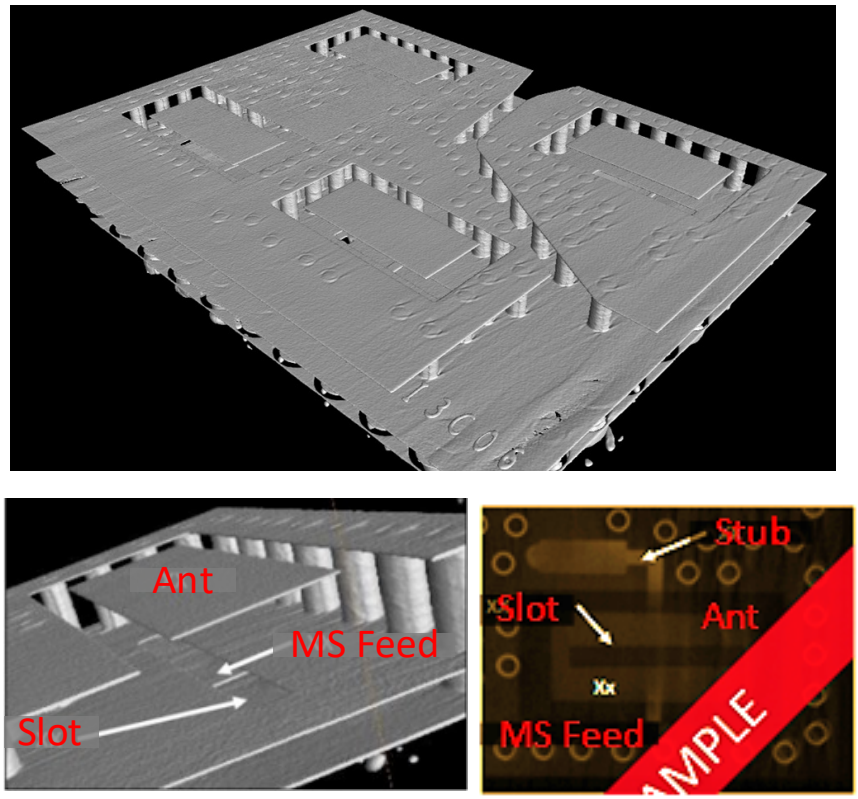


Figure 3-5 X-Ray of the radar module showing the antenna structure including surrounding vias, slot line feeding, and the input microstrip line with matching stub [33].

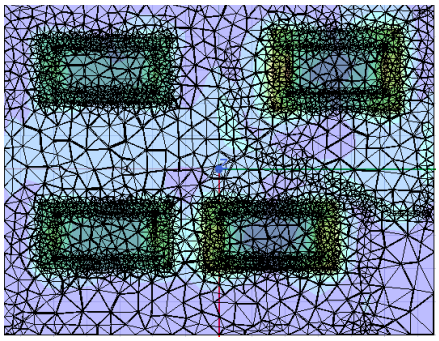
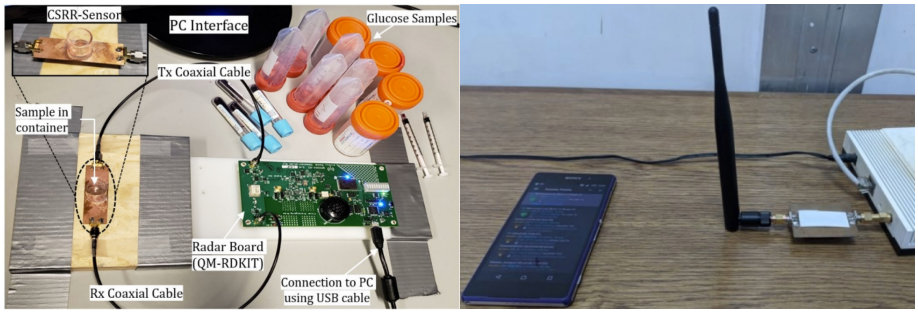


Figure 3-6 Mesh View on the top surface of the 3D HFSS model provided by Infineon.

3.2 Couplers & Bridge Design

There were other attempts for using printed circuit board (PCB) sensors along with off-the-shelf devices such as radars [9], and Wi-Fi access points [10]. In [9], [10], a resonator-based

sensing PCB was connected using cables/connectors as shown in Figure 3-7. However, this was only feasible due to the low frequency of operation (2.4 GHz). In contrast, wired connections are not feasible in mm-wave sensors as they would require costly cables and connectors to minimize losses. Moreover, it would require custom radar modules with bulky cable connections, thus, unsuitable for integration into wearable sensors.



(a) (b)

Figure 3-7 Other attempts of using PCBs as sensing mechanisms alongside (a) radars [9], and (b) Wi-Fi access points [10].

In this work, we present a similar implementation for the concept presented in [9], [10]. However, the connection between the radar board and the sensing circuit would be based on near-field capacitive coupling between the transmitter and receiver antennas of the radar and the corresponding pair of coupling antennas on a suspended superstrate as illustrated in Figure 3-8. This implementation can be highly compact; therefore, it can be easily integrated into wearables.

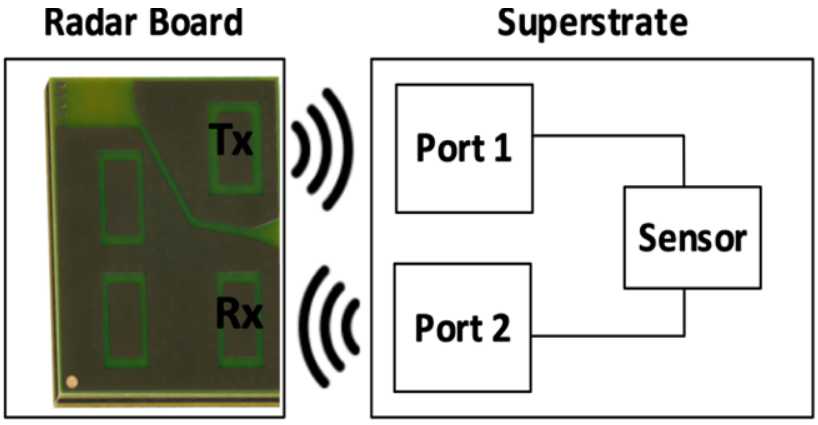


Figure 3-8 The proposed sensor architecture.

It is worth noting that although this radar module consists of one Tx antenna and three Rx, for this work, only one Rx antenna would be used for sensing through the superstrate. Consequently, other receivers along with the MIMO capabilities of the radar can be reserved for more complex sensing.

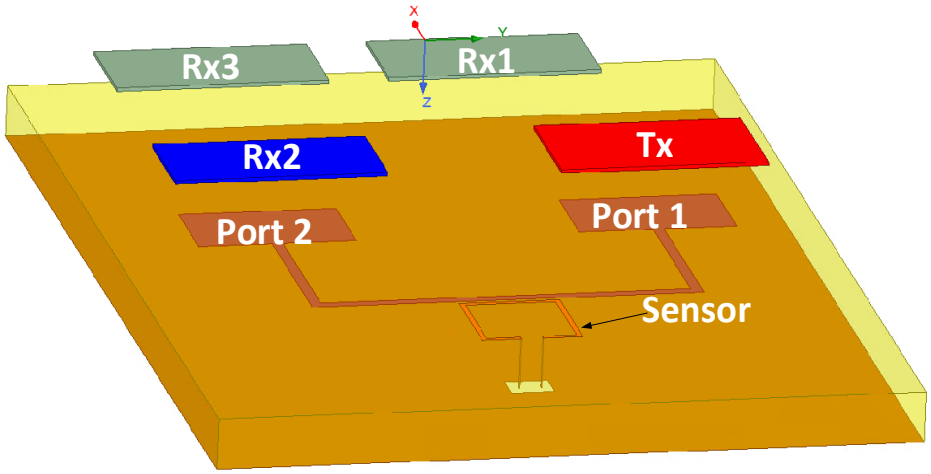


Figure 3-9 A sample 3D model of the proposed architecture.

Figure 3-9 shows a sample 3D model of the proposed sensor, where the transmitter and receiver antennas of the radar are represented as TX and RX respectively. The corresponding coupling antennas are labeled Port 1 and 2 respectively. The coupling antennas are connected by a microstrip line bridge that is connected to the sensor. In this section, we will discuss the design of the couplers and bridge while the sensor design is discussed in section 3.3.

First, we started by designing the couplers. Given the patch geometry of the antennas on the radar module, it made sense that the couplers would have a similar geometry. Therefore, we started with a pair of metallic patches and a ground plane on an FR4 substrate with an assumed $\varepsilon_r = 4.4$ at 60 GHz. Moreover, the substrate had a height of 0.5 mm, the spacing between both substrates was 0.7 mm. The separation was intended to be sufficiently small so that it remains near field coupling while being non-zero to avoid changing to inductive coupling and being DC-connected. A pair of lumped ports with 50-ohm impedance were placed at the middle of the edge to mimic an edge-fed (no inset) patch antenna as shown in Figure 3-10. Then, we conducted a series of parametric sweeps on the position and size of the antennas to maximize

the power transfer between the original ports of the radar module and the lumped ports on the couplers.

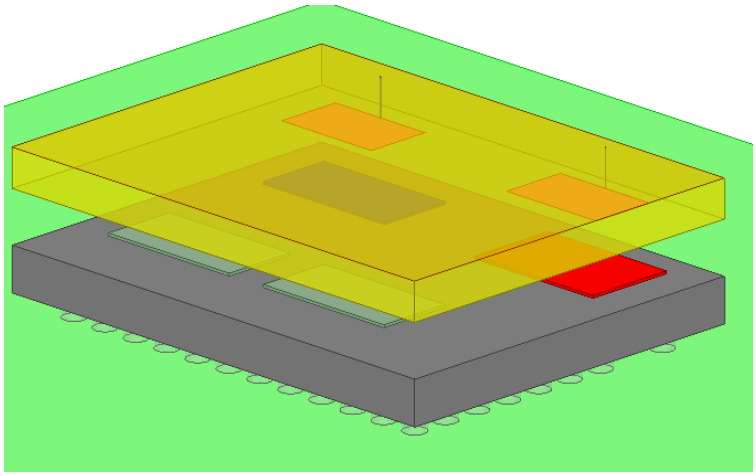
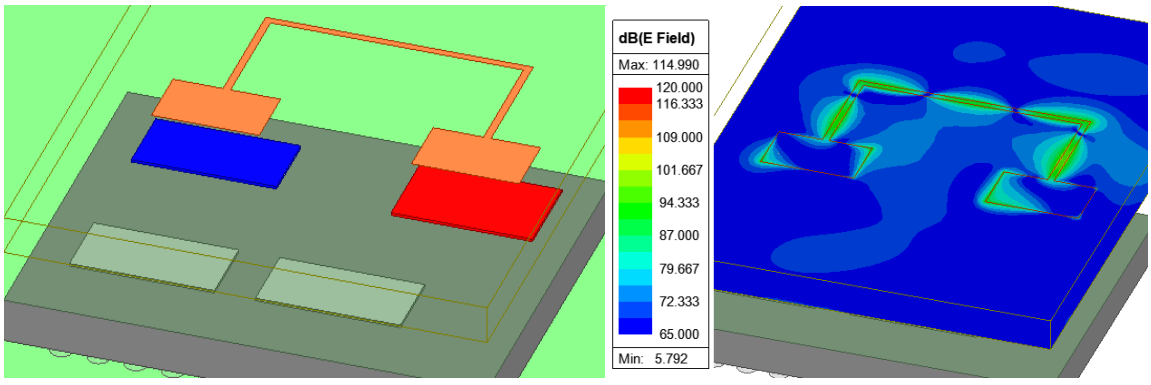


Figure 3-10 Couplers design phase.

The next phase was the design of the bridge, we decided to go with a microstrip line for simplicity. The width of the microstrip is 100 um which corresponds to a characteristic impedance of 146 ohms for this substrate. The length of the bridge was then tuned to maximize the power transfer between the Tx and Rx2. The optimized bridge structure is shown in Figure 3-11a while Figure 3-11b shows the field power flowing on the bridge due to excitation from the Tx antenna.



(a) (b)

Figure 3-11 Bridge design phase; (a) Design, (b) Field power flow on the bridge.

Figure 3-12 shows the transmission coefficient between the Tx and Rx2 antennas before and after the introduction of the couplers and bridge. We can see that there is a 20 dB improvement across the frequency range of interest.

It was worth noting that despite the design process for the couplers and bridge focusing on increasing/optimizing the coupling coefficient, it is important to remember that the power required for the operation of the receiver is significantly lower than the transmitted power. Hence, the 10 dB insertion loss is very acceptable even if the design could have been optimized further to improve the coupling. This is demonstrated further in Chapter 5 where the Tx power level of the radar had to be nerfed to avoid saturating the analog-to-digital-converter (ADC) of the receiver.

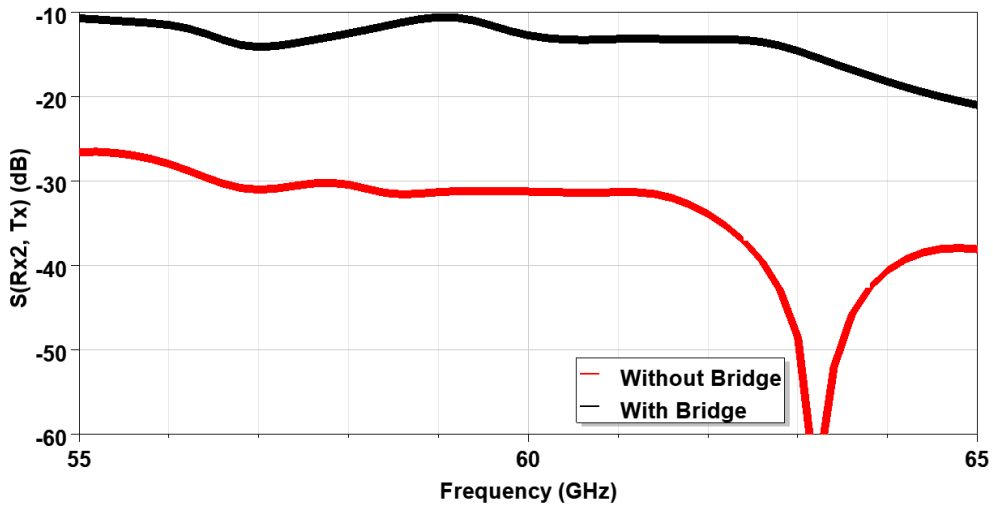


Figure 3-12 The transmission coefficient between Tx and Rx2 w/ & w/o the bridge.

3.3 Sensor Design

At this point, we have the power flowing from the transmitter antenna, through the coupler and bridge, to the receiver. Since the bridge is made of a transmission line section, we can defer to the literature on PCB microwave sensors discussed in section 2.2 for the sensor design. In this section, we propose two possible sensor implementations as a proof-of-concept.

3.3.1 Ring Resonator

The first geometry that we proposed using is an edge-coupled split-ring-resonator (SRR) as shown in Figure 3-13. Ring resonators have been widely used in many microwave-based

material sensors due to their ease of modeling and well-understood behavior [34]. Moreover, the gap of the split ring resonator acquires the highest sensitivity to the sample properties [34]. Two vias are placed in the gap of the split ring resonator leading to an etched area of the ground plane. The purpose of the vias is to transfer the field to the other side of the substrate where it would interact with the sample. The etched area in the ground plane serves as the sensing region where the sample would be placed for sensing. The concept of using vias can be looked at as increasing the capacitance which would be perturbed by the sample. A similar concept was done by Ramahi *et al* [35], where aluminum blocks were soldered on top of a PCB to increase the capacitance and ultimately, improve the sensitivity.

The dimensions of the ring resonator were a direct trade-off between the resonance frequency and the feasibility of fabrication. To have a first harmonic in the band of interest, the perimeter of the resonator would have been too small, thus, requiring a smaller trace width adding a constraint on the minimum feature size of the fabrication process and significantly increasing the cost of the sensor. Therefore, we designed the sensor such that its third stopband is in the band of operation as shown in Figure 3-14. It is worth noting that, unlike the dimensions of the resonator, the design process is independent of the dielectric properties of the substrate. Hence, it is expected that the dimensions of the final tape-out design would need to be re-tuned to work on the selected manufacturing substrate.

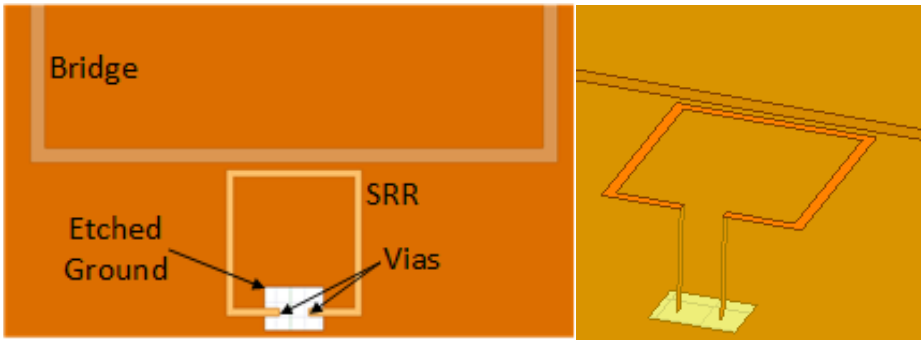


Figure 3-13 Proposed split ring resonator sensor.

Figure 3-15 shows the transmission coefficient between the transmitter and receiver antenna of the radar board in three different design phases. As shown in Figure 3-15, the stopband caused by the introduction of the ring resonator can be seen around 58 GHz. The frequency shift can be explained by the pull/push from the multiple resonators involved including the

couplers and bridge. Figure 3-16 shows the field configuration due to excitation from the radar module transmitter antenna the field goes through the couplers, bridge, and resonator and towards the sensing area through the vias.

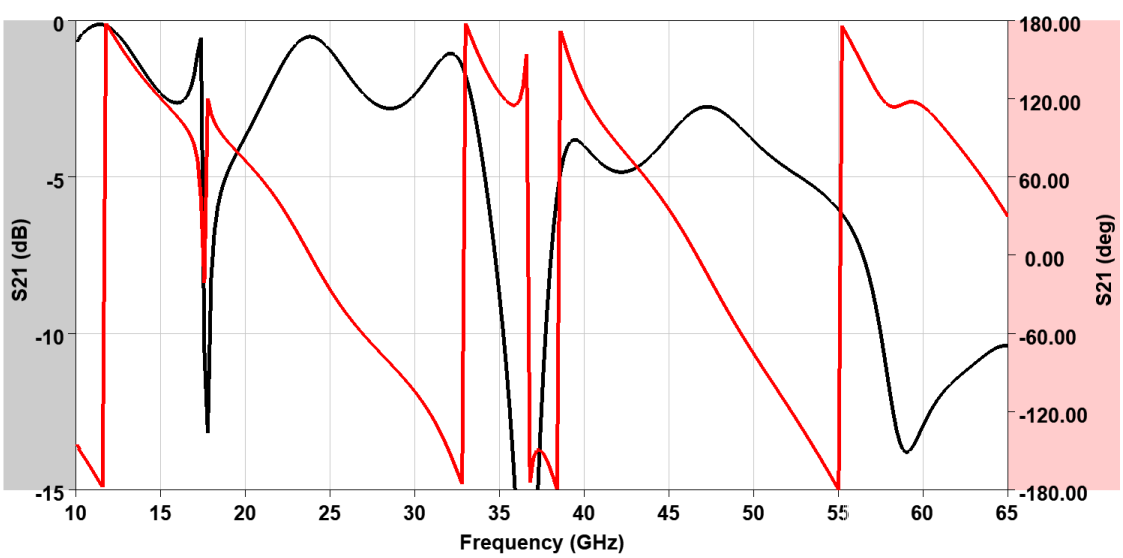


Figure 3-14 S21 (magnitude and phase) of the resonator shown in Figure 3-13.

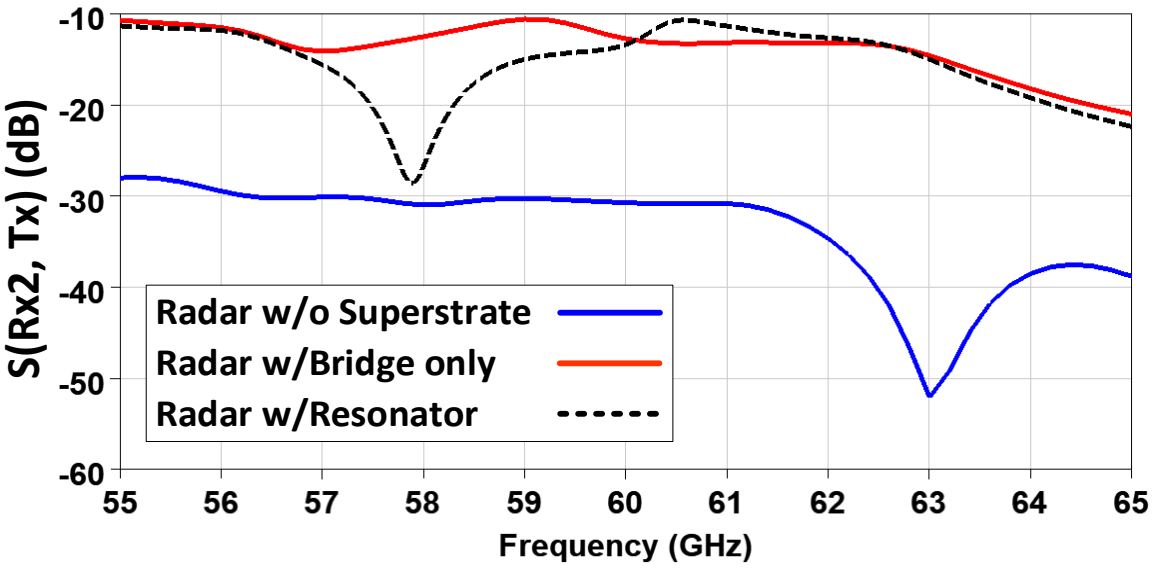


Figure 3-15 The transmission coefficient between the transmitter and receiver of the radar at different stages in the sensor design.

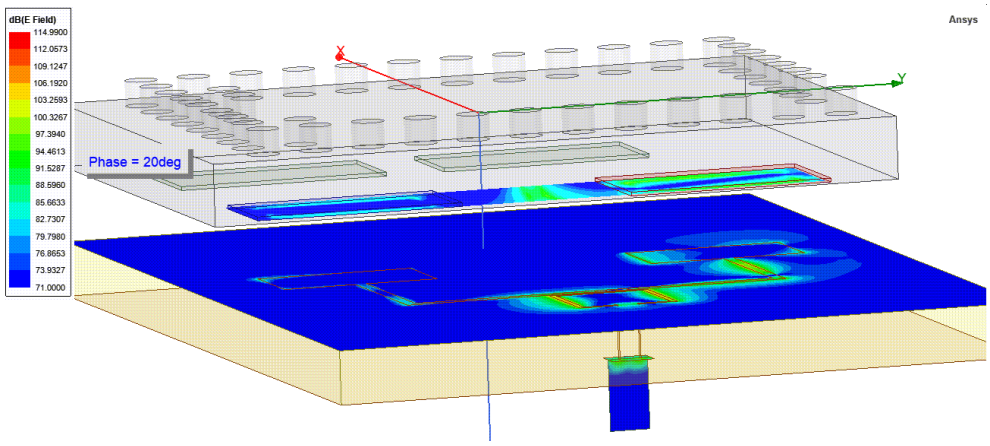


Figure 3-16 The field configuration on the bridge, SRR, and sensing region.

After the initial resonator was designed, it was time to introduce the sample to the simulation. First, we used the dielectric properties of the human skin proposed by Chahat *et al* in [36] which was then used to calculate the dielectric properties of skin at 60 GHz in [37] as $\varepsilon' = 7.98$, and $\sigma = 36.38$ S/m. To simulate the skin layer, we have added a 2 mm skin layer 100 um away from the surface of the lower side of the superstrate. Although the 2 mm thickness may seem small, it is almost 3 times the wavelength which is sufficient for the field to completely decay. Additionally, the sensing area is not radiative as demonstrated by the field configuration shown in Figure 3-16. Representing the skin displacement due to the radial artery pulsating, we added a box with the same skin properties as shown in Figure 3-17. The width of the pulse box was 0.5 mm while the height was parametrized vs time as (3-1) [7] where D is the displacement as a function of time (t), H is the maximum displacement, and HR is the heart rate in beats per minute (bpm). For these simulations, we used $H = 0.05$ mm, $width = 0.5$ mm which corresponds to a worst-case scenario of a small and narrow variation [7], and a sample $HR = 75$ bpm.

$$D(t) = H \cdot \frac{\cos\left(2\pi t \cdot \frac{HR}{60}\right) + 0.7\cos\left(4\pi t \cdot \frac{HR}{60} - 200\right) + 1.32}{2.92} \tag{3-1}$$

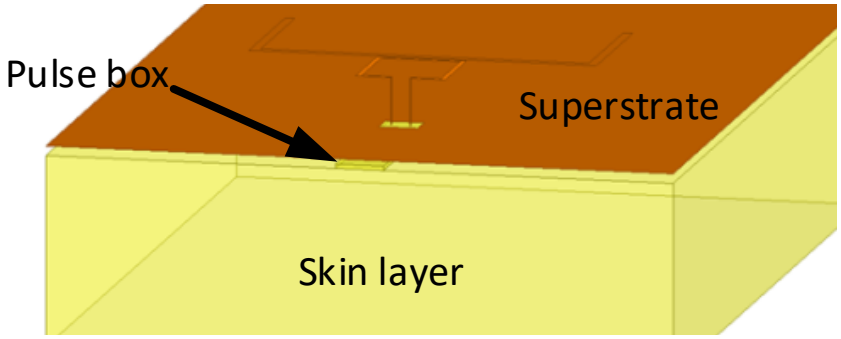


Figure 3-17 The model for the skin layer and pulse box.

To get the response of the sensor under the time-varying phenomena of the pulsating artery, we swept the time variable in HFSS. The time was swept from 0 to 1 sec, thus, covering more than a period of the pulse waveform (0.8 sec). Each of these iterations represents the S-parameters of the sensor in slow time i.e., assuming it to be stationary within the duration of the radar chirp. It is worth noting that for the sake of efficiency, the sweep is conducted on the simplified model of the sensor with bridge only as including the radar module and couplers increases the simulation time significantly. It is fair to assume that the changes observed in the simplified simulation would be indicative of the changes in the whole thing. Figure 3-18 shows the reference displacement waveform as described by (3-1).

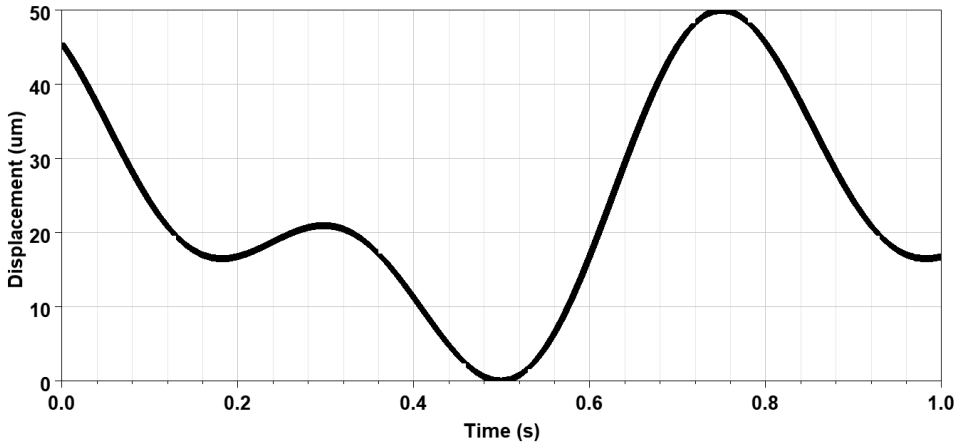


Figure 3-18 The reference displacement waveform described by (3-1).

Figure 3-19 shows the transmission coefficient (S_{21}) vs frequency for the different time points. It may seem that the motion of the artery would cause slight shifts in the resonance

frequency of the sensor. However, As shown in Figure 3-20, there is no obvious correlation between the input waveform and the insertion loss at the resonance frequency (58.75 GHz).

At this point, a design change was required. However, we needed to understand why this sensor design had poor sensitivity despite using an SRR. By observing the geometry and the equivalent circuit pi-model of the microstrip-line gap, we can see that it is composed of two shunt capacitances to the ground and a series capacitance between both strips [38]. By using the vias, we have managed to increase the series capacitance, however, we have inadvertently significantly increased the shunt capacitance to the point that they started behaving as a perturbed short circuit. Consequently, although the field is interacting somewhat with the sample, it is not responding well from a circuit performance perspective.

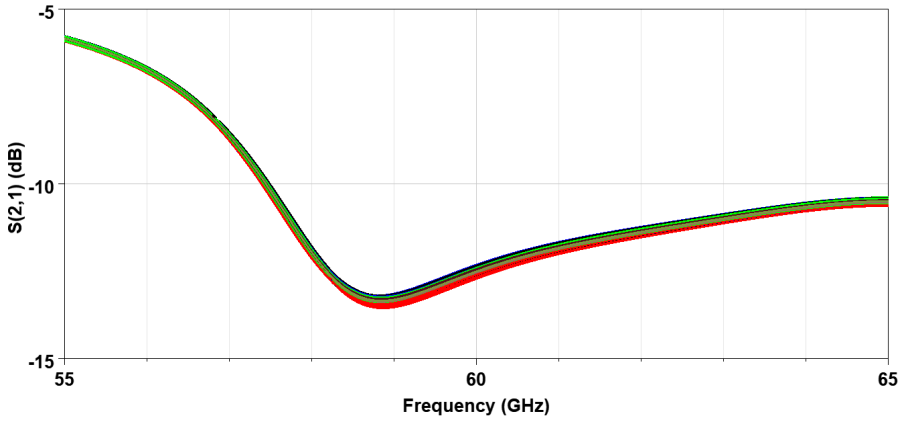


Figure 3-19 The transmission coefficient vs. Frequency for different time points.

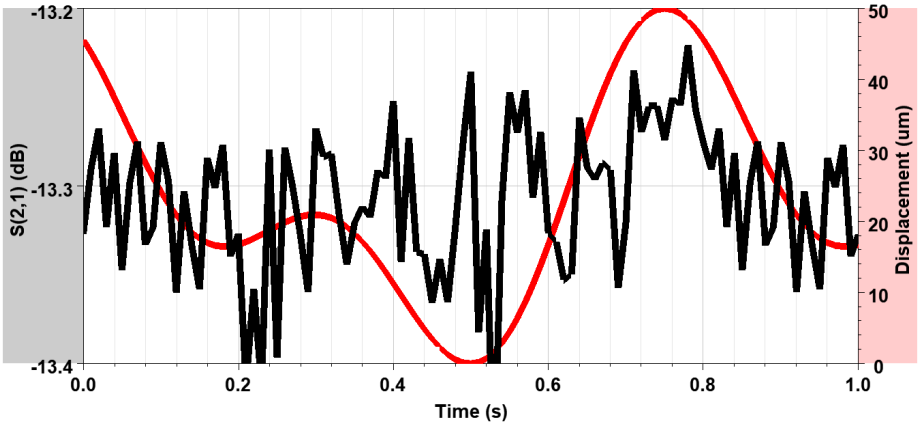


Figure 3-20 The value of the transmission coefficient at 58.75GHz compared to the input reference waveform.

3.3.2 Defective Ground Structure

In the previous subsection, we proposed an SRR-based design for the superstrate radar module sensor. However, we have found its sensitivity to be underwhelming. Therefore, in this subsection, we will introduce another design that considers the drawbacks of the previous design. The proposed design would make use of defective ground structures for interaction with the sample. Although it is possible to use complementary split ring resonators (CSRRs), they are electrically similar as circuit elements to their linear counterparts [39] with less parasitic effects due to the bending of the slot.

Figure 3-21 shows the structure of the proposed sensor, it consists of a longitudinal slot etched in the ground plane of the bridge. The slot is known to act as two parallel short-circuited stubs connected in series to the host microstrip line [39]. Placing SUT in the reactive near-field region of the slot would introduce losses and therefore, add a resistive component in series to the bridge. The value of this resistance would change the level of power transfer across the bridge due to changes in the quality factor of the resonator; thus, a sensing decision can be made from the amplitude [39]. Moreover, the sample would affect the complex part of the propagation constant (β) causing its resonance frequency to shift [39].

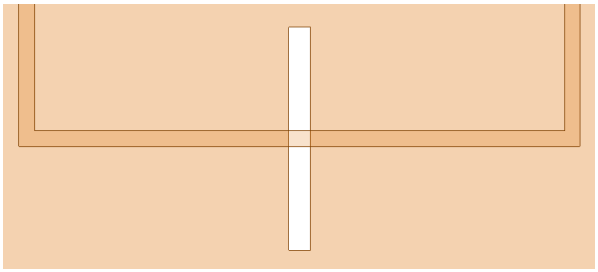


Figure 3-21 Proposed defective ground structure sensor.

To design the DGS, we started with a length that would provide a resonance frequency of around 60 GHz (odd multiples of $\lambda_g/2$), then to decide on the slot width to maximize sensitivity, we added a 180-um layer and swept its *tan* δ for comparison. Although this is not a direct mapping to the pulse problem, it can offer a straightforward method for sensitivity assessment. We have decided on a slot dimension of 0.14 x 1.43 mm^2 for a trade-off between bandwidth and sensitivity. Figure 3-22 shows the response of the sensor before the introduction of the sample, with a stopband behavior in the band of operation.

Then, we added the pulse sample as described in section 3.3.1 and shown in Figure 3-17. The resulting magnitude of the transmission coefficient is shown in Figure 3-23. Both the resonance frequency and insertion loss are affected by the pulse. However, the effect on the insertion loss is more pronounced. By comparing the magnitude and phase of the transmission coefficient to the input displacement waveform at 62.7 GHz (for max pk-pk variation) as shown in Figure 3-24, we can see a clear correlation. It is worth noting that the similarity in the amplitude and phase response to the motion is specific to this sensor design and shouldn't be generalized to the concept of superstrate. It is worth noting that the oscillations in the behavior of the phase response shown in Figure 3-24b are primarily due to the amplitude error being the convergence criteria therefore, there is a residual numerical error in the phase response. Although tightening the convergence criteria to a max amplitude delta of 0.005 removes these ripples as shown in Figure 3-25, it is not recommended as the simulation time increases significantly to get this level of accuracy with diminishing outcome. During the measurements in Chapter 5, we would rely primarily on the changes in the amplitude (power).

At this point, we have shown a correlation between both the phase and amplitude response of the sensor. However, we haven't discussed how the sensitivity of the sensor compares to the basic sensitivity of a 60 GHz radar, so we used HFSS v.2022R2's Shooting and Bouncing Ray (SBR+) solver to obtain the transmission coefficient phase response for a similar motion. The 50-um pulse motion resulted in a peak-to-peak phase variation of 2.1 degrees while the DGS sensor achieved a phase variation of 3.27 degrees as shown in Figure 3-24b, this is an impressive 55% improvement. The details of the SBR+ simulations are discussed in section 4.1.

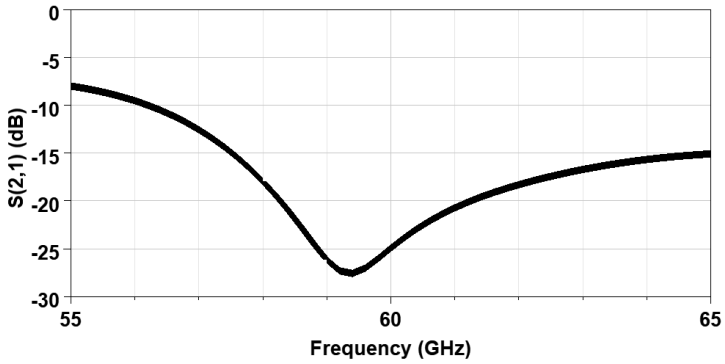


Figure 3-22 The response of the sensor before introducing the sample.

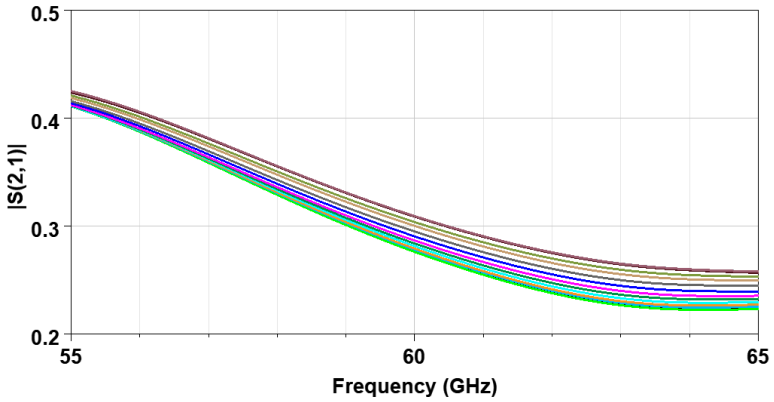
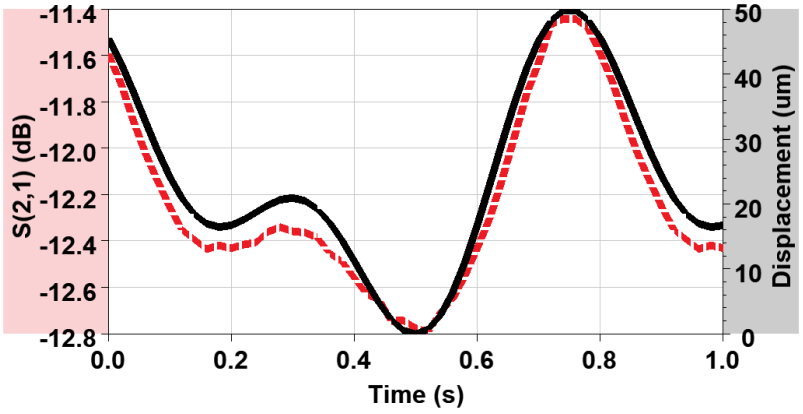
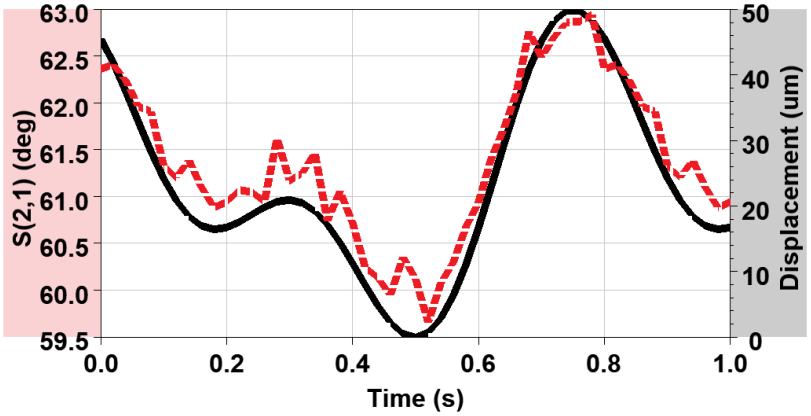


Figure 3-23 The transmission coefficient vs Frequency for different time points (t, from 0 to 1s, with a step of 0.1s).



(a)



(b)

Figure 3-24 The (a) magnitude, (b) phase; of the transmission coefficient at 62.7 GHz compared to the input reference waveform.

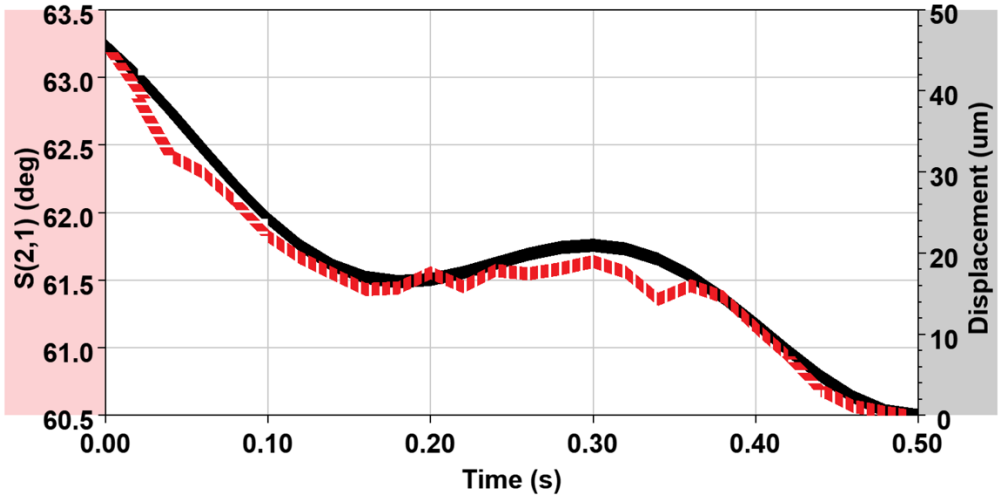


Figure 3-25 The Phase of the transmission coefficient at 62.7 GHz after tightening the convergence criteria.

It is also important to understand how changes in the dielectric properties of the skin may affect the performance of the sensor. These changes could be due to many physiological factors including age, race, gender, hydration status, blood glucose level, etc. Therefore, we repeated the simulation while varying the dielectric properties (ε', σ) of the skin by +/- 10%. The result of this study is shown in Figure 3-26 which shows that despite the sensitivity to the dielectric properties, it is not detrimental to the performance.

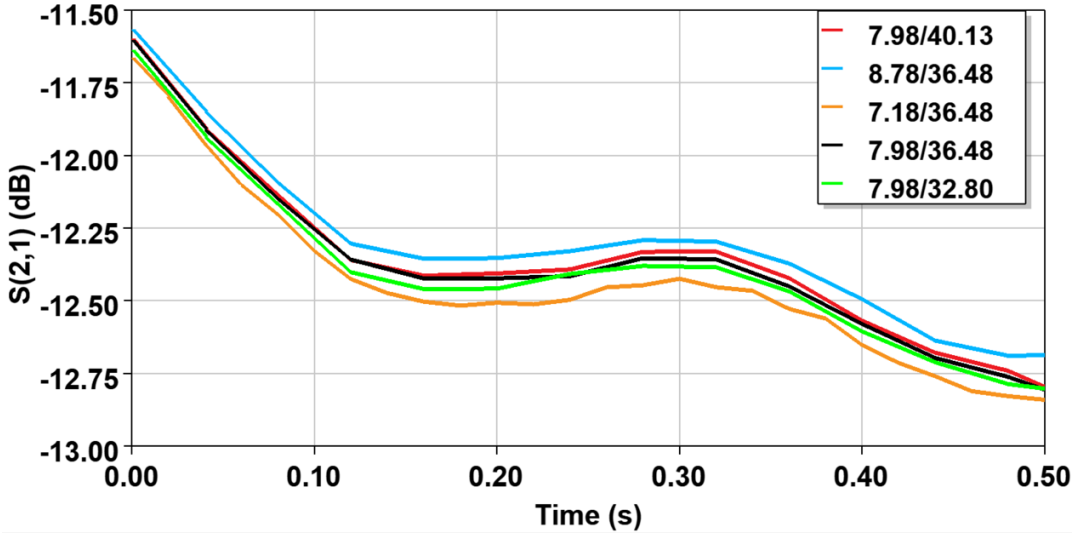


Figure 3-26 The effect of the varying dielectric properties of the skin on the performance of the sensor. The legend shows the values of $\boldsymbol{\varepsilon'}$ / **σ** respectively.

Chapter 4

Radar-based Simulations

4.1 Shooting and Bouncing Ray Simulations

Ansys HFSS [30] is known in the microwave community for its frequency and time domain finite element method (FEM) solver. The FEM solver is widely used for solving Maxwell's equations for the design of high-frequency circuits and components. However, FEM is notoriously slow, therefore, running simulations with large footprints (relative to the wavelength) can extend across multiple days, thus, making true optimization unattainable. The SBR+ solver, on the other hand, offers acceptable accuracy for radar applications but at a much-improved performance. Moreover, it is possible to use the radar specifications to directly predict the range, doppler, and micro-doppler of a specified test scenario [32], [33]. It is worth noting that to our knowledge, we are the first to attempt to use SBR+ simulations in a biomedical application such as pulse sensing.

In this section, we aim to use an SBR+ test bench to create a digital twin for pulse sensing applications using mm-wave radars. Due to the high performance of SBR+ simulations, it can be used to simulate the effects of multiple sources of variability including pulse location, maximum height of distension, width of distention, as well as some abnormality in the pulse waveform.

4.1.1 Simulation Setup and Verification

The first step in setting up an SBR+ simulation is to set the parameters of the antenna/power source. Table 4-1 shows the input parameters for the radar, these parameters represent the recommended parameters from Infineon for short-range applications [42]. The Infineon radar was specifically selected in these simulations because its ability to capture the pulse waveform has been experimentally verified in [8]. The other setting was the radiation pattern properties, we opted for a generic parametric beam as the effects of polarization, and angles of incidence

are not relevant for this section. The properties of the beam were as follows; vertical and horizontal beam widths are 30 and 60 degrees respectively, the polarization is vertical, and the port impedance is 50 ohms.

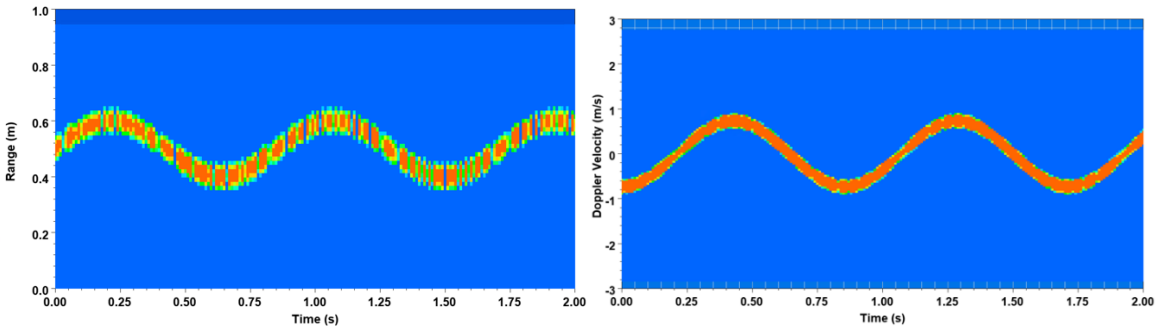
Table 4-1 Input and Calculated Radar Parameters for the SBR+ Simulation.

	Parameter	Value	Unit
Input	Center Frequency	60	GHz
	Range Resolution	3	cm
	Range Period	96	cm
	Velocity Resolution	0.089	m/s
	Minimum Velocity	-2.84	m/s
	Maximum Velocity	2.84	m/s
Calculated	Bandwidth	5	GHz
	Chirp Duration	64	μs
	Number of Chirps per frame	64	-
	Chirp Duty Cycle	14.6	%

There are three main outputs for an SBR+ simulation: range, doppler velocity, and S-parameters. The range and Doppler outputs are in the form of a matrix where for each possible value of range and Doppler (as dictated by the radar specifications) there is an intensity (power) value for each time point. Consequently, it is not possible to visualize all the data in a single 2-D report/color map, therefore, for any of the presented results in this sub-section, we will show plots at a single point in time/range/doppler. This is important as the exact hues of the colors may give an incorrect impression if the sampling of the third variable is not considered.

To start the test, we needed to verify that we are getting meaningful results from the simulation. We started with a basic setup of an oscillating metallic plate placed 0.5 meters away from the radar with a sinusoidal motion with an amplitude of 0.1 meters and a frequency of 70 cycles per minute (around the resting heart rate frequency). The time variable was swept from 0 to 2 sec with a step of 0.01 sec. Figure 4-1 shows the range and velocity results for this

oscillating plate test case. As seen in the results, the motion has a peak-to-peak displacement of 0.2 meters. Moreover, the velocity has the correct phase and amplitude. It is worth noting that to plot the images shown in Figure 4-1, the color map scale was particularly set to provide high contrast between the main signal and the background fringes.



(a) (b)

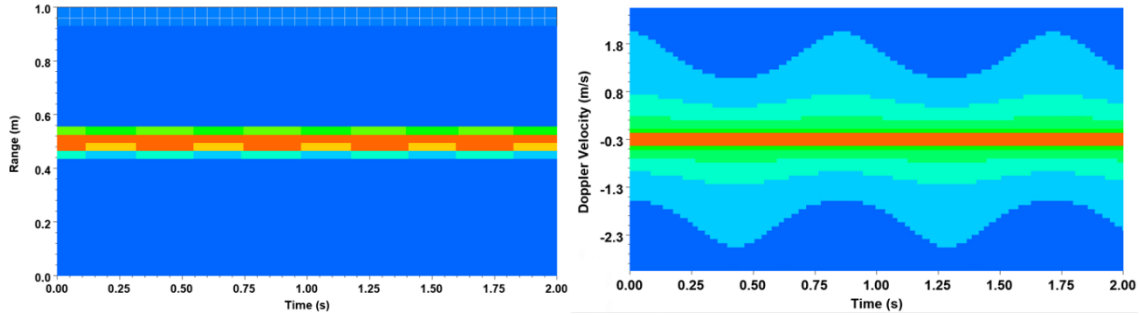
Figure 4-1 The result of the calibration large signal test case showing (a) Range, and (b) Doppler Velocity as a function of time.

The next step was to reduce the size of the displacement to something more relevant to our target application, Thus, we reduced the amplitude of the sine wave to 50 µm. Figure 4-2 shows the result of the reduced amplitude displacement. As observed in the range plot, the radar was unable to detect the motion of the plate at the reduced displacement. This can be explained by the fact that the peak-to-peak displacement was only 100 um which is more than two orders of magnitude lower than the 3 cm range resolution of the radar.

In the Doppler velocity plot, on the other hand, the main bin was zero velocity. However, due to the windowing effect, there are fringes surrounding the main bin. Moreover, these fringes seemed to represent the sinusoidal shape of the motion. This behavior exhibited by the simulation may explain reports of similar radar modules in the literature [7], [43], despite it being beyond the official specifications of the radar modules. In subsection 4.1.2, we will present an approach to reconstructing the motion waveform from these fringes. However, In the remainder of this subsection, we will present the setup results for the pulse waveform.

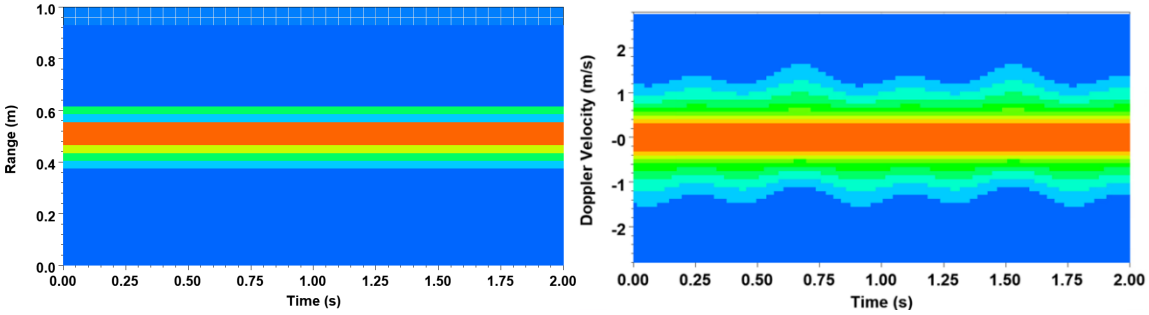
The next step was to change the waveform from a pure sinusoidal wave to the dual harmonic pulse waveform described by (3-1) with the maximum displacement and heart rate set to 50 um and 70 bpm respectively. Figure 4-3 shows the simulation results, as with the calibration

case, the range plot has a very poor correlation with the input waveform. However, the velocity waveform does have some fringes that resemble the derivative of the displacement waveform where there are two peaks with different amplitudes.



(a) (b)

Figure 4-2 The result of the reduced displacement calibration test case showing (a) Range, and (b) Doppler Velocity as a function of time.



(a) (b)

Figure 4-3 The result of the pulse waveform test case showing (a) Range, and (b) Doppler Velocity as a function of time.

The next step was to make the setup more realistic by including a model of a human hand as shown in Figure 4-4. Then, we selected one of the triangles making up the surface of the wrist and added the pulse waveform motion to it so that it mimics the vibrations of the radial artery. Figure 4-5 shows the result for the testbench shown in Figure 4-4, as expected the range is reduced because the target is much closer to the radar but still there is no correlation between the motion and the range bins. The velocity, on the other hand, still shows some resemblance to the motion. However, unlike the results shown in Figure 4-3, there is a slight asymmetry between the top and bottom fringes. This may be due to the asymmetry in the shape of the

artery, and it being not perfectly aligned with the radar beam. In this test case, The radar's antennas were placed 80 mm away from the surface of the skin to avoid the wrapping of the range fringes over the range period creating a phantom at the max range as shown in Figure 4-6 where the distance was reduced to 1 cm. Although the Doppler velocity waveforms show fringes representing the skin displacement, more fundamental tests would be required to verify if the calculation method is valid at such proximity.

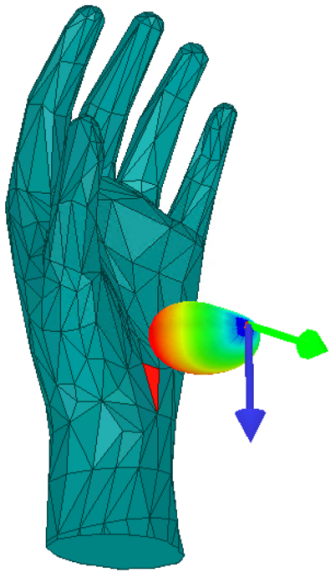
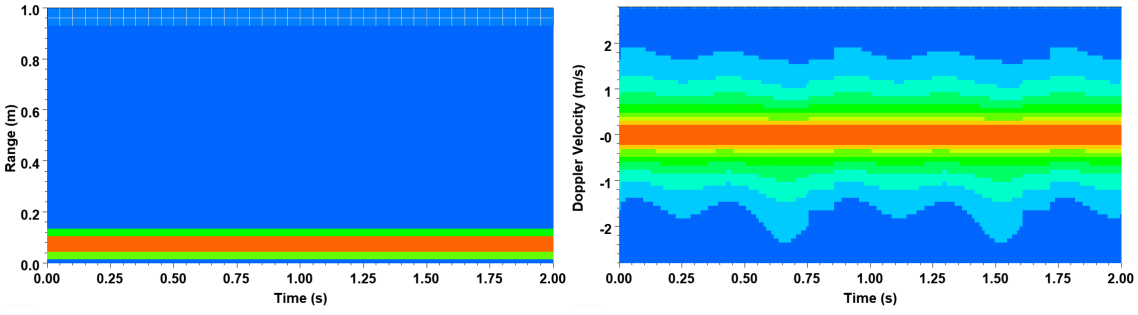
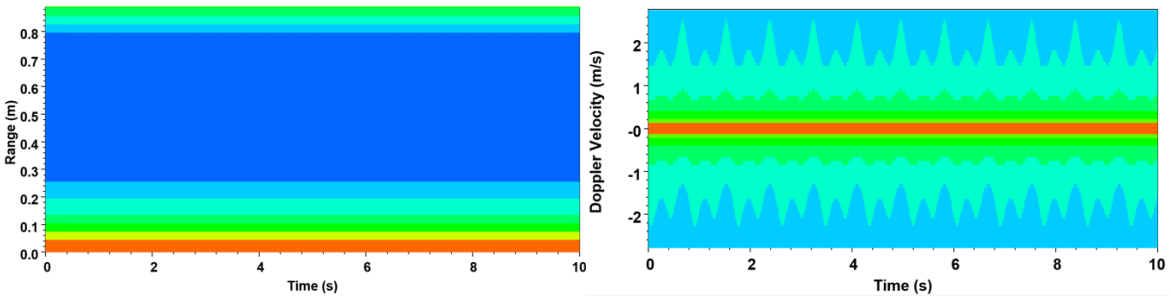


Figure 4-4 The setup for the pulse SBR+ simulation, showing the hand model, and radar beam pattern. The red triangle represents the oscillating object that corresponds to the pulsating radial artery.



(a) (b)

Figure 4-5 The result of the pulse on wrist test case showing (a) Range, and (b) Doppler Velocity as a function of time.



(a) (b)

Figure 4-6 The result of the pulse on wrist test 1 cm away from the skin case showing (a) Range, and (b) Doppler Velocity as a function of time.

4.1.2 Waveform Reconstruction

In the previous section, we showed some preliminary results for calibration test cases and obtained the range-doppler maps vs time. However, we observed that since the motion is less than the range and velocity resolutions, tracking the highest power would not be sufficient. Instead, the information is more clearly presented in the fringes surrounding the main bin. To verify that these fringes truly correspond to the wanted input signal and that they can accurately represent changes in amplitude/frequency of the input signal.

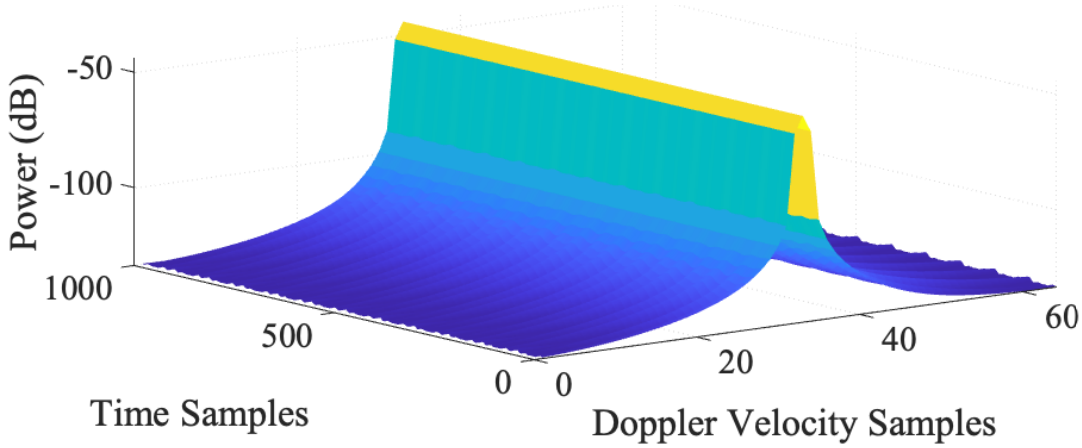


Figure 4-7 Imported data from HFSS showing power vs velocity & time.

First, we exported the Doppler velocity vs time graphs and imported them into MATLAB v.2023b as shown in Figure 4-7. The imported data consists of 64 Doppler Velocity samples corresponding to the ratio between the velocity range and resolution. Moreover, the simulation

time was increased to 10 seconds with a sampling rate of 100 Hz so a total of 1000 samples. The power values are exported in dB. In Figure 4-7, we can see the maximum around the middle velocity bin which corresponds to zero Doppler velocity. Then, we used the built-in contour detection function to extract 20 contours, 10 on either side of the maximum. The number of contours is flexible, however, we found that 10 was sufficient to have a clear and visible waveform as shown in Figure 4-8. Next, we selected the outermost contour and removed the DC component (due to the contour offset) by doing a Fast Fourier Transform (*fft*) and replacing the DC component with 0 then an Inverse FFT (*ifft*). This is valid as we know that this is a purely oscillating motion without a net displacement.

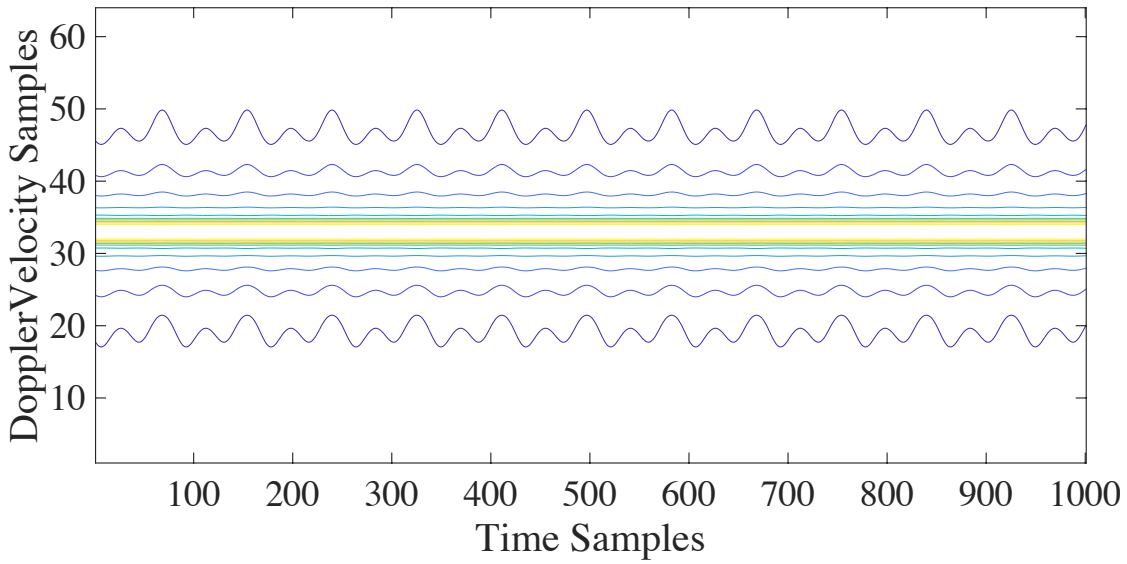


Figure 4-8 The Detected 20 Contours, 10 on each side of the zero-velocity bin.

Figure 4-9 shows the resulting velocity plot. It is worth noting, that there is uncertainty in the scale/unit of the reconstructed velocity waveform as it is highly dependent on the selected contour, thus, the arbitrary unit (a.u.) label. With that said it should be straightforward to calibrate if the transformation is linear. Then, we integrated the velocity w.r.t. time using the cumulative trapezoidal method to obtain the displacement as shown in Figure 4-10.

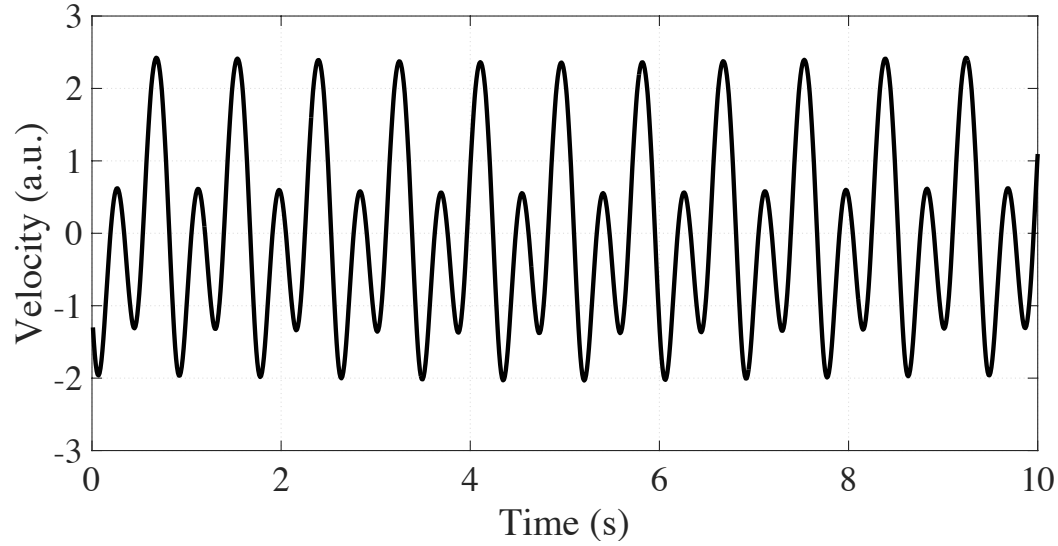


Figure 4-9 Reconstructed velocity plot after DC offset removal.

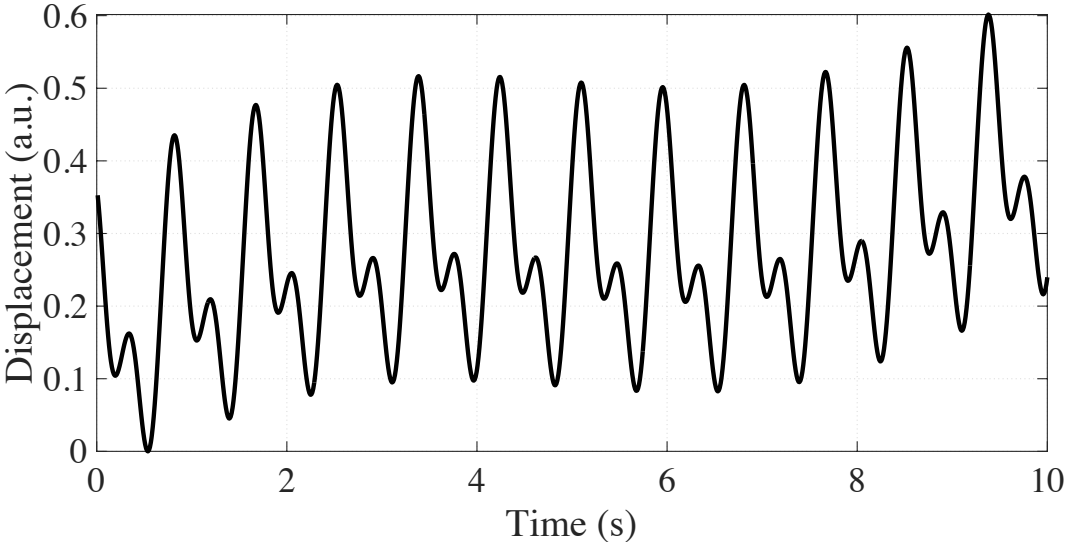


Figure 4-10 Reconstructed displacement waveform obtained from integration of velocity with the minimum set to zero.

As observed in Figure 4-10, the waveform was reconstructed. However, there is a low-frequency signal added due to the accumulation of error from the cumulative integration. Consequently, we used curve fitting to restore the extracted velocity to a dual harmonic function before integration. Thus, the noise is reduced, and the displacement waveform can be accurately reconstructed as shown in Figure 4-11. It is worth noting that the curve fitting assumes the function to be in a dual harmonic form, this is valid for an ideal waveform.

However, it may cause a loss of information if the waveforms are distorted due to a medical condition. Nonetheless, the timing of the pulses should remain intact so that the heart rate and heart rate variability can be extracted. Moreover, during the integration process, the resulting constant was selected such that the minimum displacement was zero for comparison with the input waveforms.

Figure 4-12 shows a comparison between the reconstructed displacement waveform and the input 50-um displacement waveform. There is an excellent agreement between both waveforms. However, there is a slight misalignment around the 2nd peak which may be explained by the quantization-induced error due to the velocity resolution. It is worth noting that for both graphs to match, the reconstructed waveform was scaled by a factor of 119.37.

To verify that the scaling is linear, thus, only one calibration step would be required, we repeated the waveform reconstruction algorithm on a similar test with a peak displacement of 70-um while maintaining the same scaling factor obtained from the 50-um test case. Figure 4-13 shows a comparison between the reconstructed and input waveforms for both maximum displacement values. There is an excellent agreement between the 70 um waveforms, thus, confirming that the scaling is indeed linear and that a single graph is sufficient for amplitude calibration.

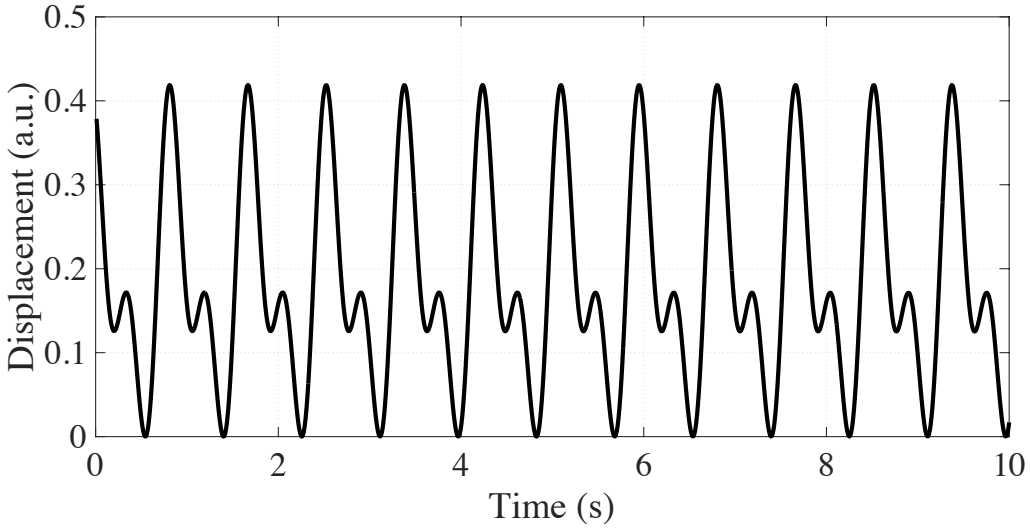


Figure 4-11 Reconstructed displacement waveform after applying curve fitting.

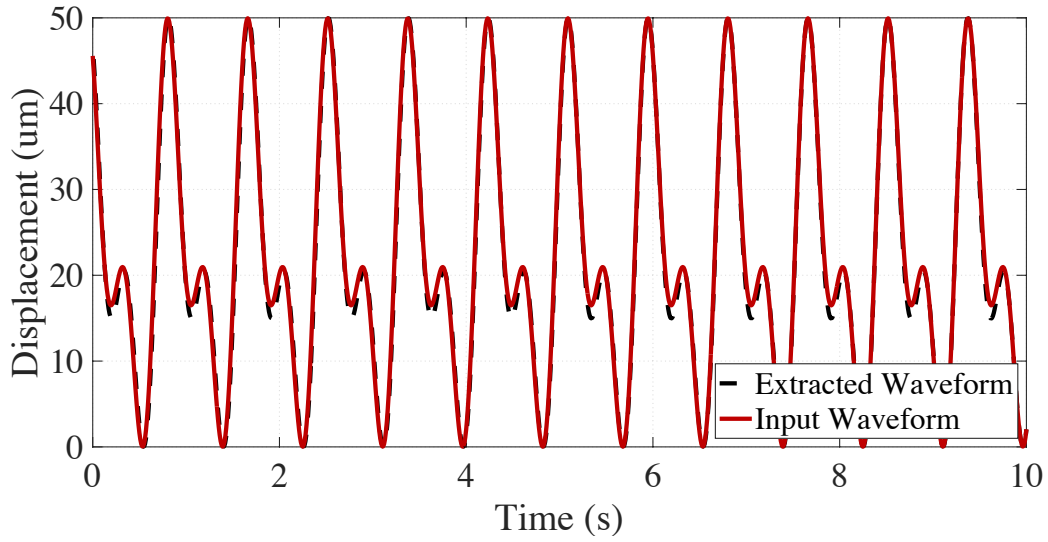


Figure 4-12 Comparison between the reconstructed and original displacement waveform after scale calibration.

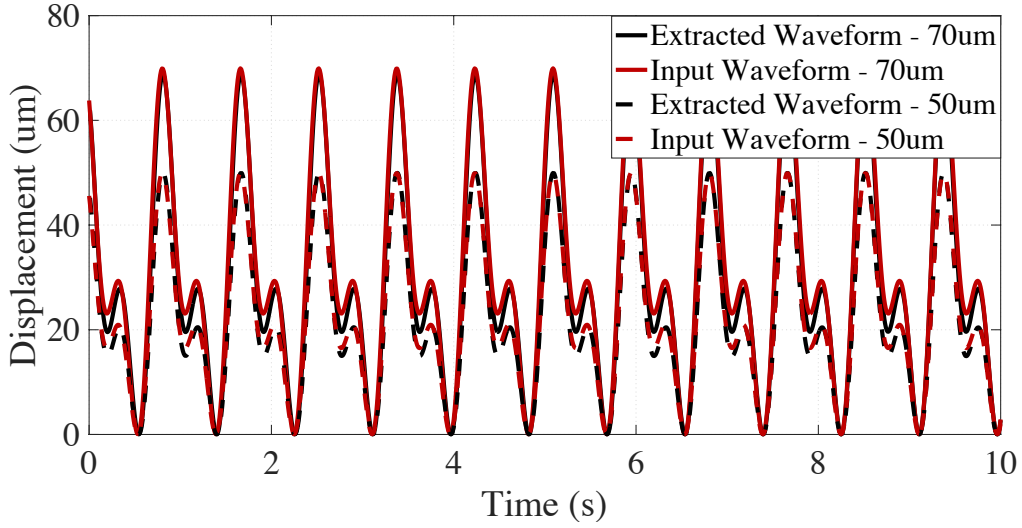


Figure 4-13 Comparison between the reconstructed and original displacement waveform with two different maximum distension while maintaining the same scaling factor.

4.2 Numerical-based Radar Simulations

In Chapter 3, we have referred to the performance of the radar, superstrate, and sensors in terms of S-parameters. However, a point that needs to be investigated is whether S-parameters in terms of frequency can accurately represent a linear circuit's time domain response. Moreover, how do these S-parameters map to actual measurements obtainable from an FMCW radar? It is well understood that the S-parameters represent the response of the circuit to a

continuous wave stimulus, thus, fully representing a linear time-invariant system. In this section, we are introducing the foundational code to map the results from Chapter 3 to the output of the radar during measurements.

4.2.1 Calculation Method

Although the phenomenon under investigation is time-varying in nature, it is fair to assume the system is stationary if the chirp duration is much smaller than changes in the system. This process creates two types of time scales, the first is the fast-time which represents the RF chirp waveform for the chirps, and another slow time for the S-parameters where the system is considered stationary for the duration of the chirp. In this section, we use the S-parameters obtained from EM simulations from HFSS. Then, we will use numerical calculations to transform them into beat frequency signals like those obtained from the measurement. This process will allow us to predict the response of the sensor to different stimuli and sensor designs. Moreover, it can be used to generate training datasets for machine learning / neural network models.

To start the modeling process, we used MATLAB v.2023b to generate a chirp. The waveform of the transmitter chirp is described by (4-1) for the duration of the chirp. In our radar specifications, the starting frequency (f_o) is 58.5 GHz, the bandwidth is 5 GHz, and the chirp duration is 64 us. It is worth noting that the chirp duty cycle was 14% i.e. for the rest of the frame duration, the transmitter was off.

$$T_x(t) = \sin\left(2\pi t \cdot \left(f_o + kt\right)\right) \tag{4-1}$$

The next stage was to obtain the frequency domain spectrum of the transmitted signal (T_x) using Fast-Fourier-Transform (*fft*) as shown in (4-2).

$$T_x(f) = fft\left(T_x(t)\right) \tag{4-2}$$

Next, the spectrum of the received signal is obtained by multiplying the spectrum of the transmitted signal with the S-parameters obtained from the HFSS simulation as shown in (4-3). However, it is worth noting that it is not feasible to obtain the necessary number of points required for the multiplication directly from HFSS. Therefore, we chose the parameters of the frequency sweep to span from 50 to 70 GHz. Thus, it covers the whole spectrum of the

transmitted and received signals. Moreover, we interpolated the intermediary points to obtain one-to-one correspondence with our frequency vectors.

$$R_x(f) = T_x(f) \cdot S_{21}(f) \tag{4-3}$$

Next, it was necessary to obtain the time-domain representation of the received signal using an inverse-Fast-Fourier-Transform (*ifft*) as depicted in (4-4).

$$R_x(t) = ifft\left(R_x(f)\right) \tag{4-4}$$

The time-domain intermediate frequency signal (IF(t)) is the output of the mixer between the transmitted and received signals, thus, it could be represented by multiplying the time domain transmitted and received signals as shown in (4-5).

$$IF(t) = T_x(t) \cdot R_x(t) \tag{4-5}$$

Finally, the spectrum of the intermediate frequency signal also known as the beat frequency is obtained by *fft* as shown in (4-6). Figure 4-14 shows a block diagram of a basic FMCW radar RF frontend, where the S-parameters obtained from HFSS represent the linear network between radar's antennas passing through the target in general or in our case the superstrate. It is worth noting that the underlying image shown in Figure 4-14 was obtained from [44]. It is worth noting that since the IF signal is in the baseband, any subsequent frequency spectrums will have low-frequency axes.

$$IF(f) = fft(IF(t)) \tag{4-6}$$

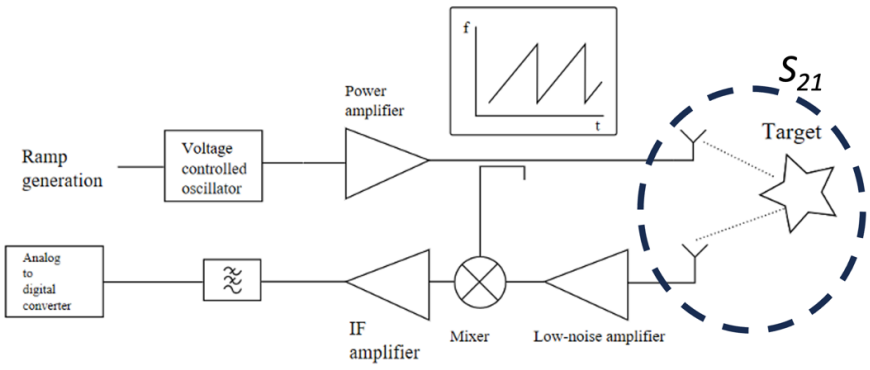
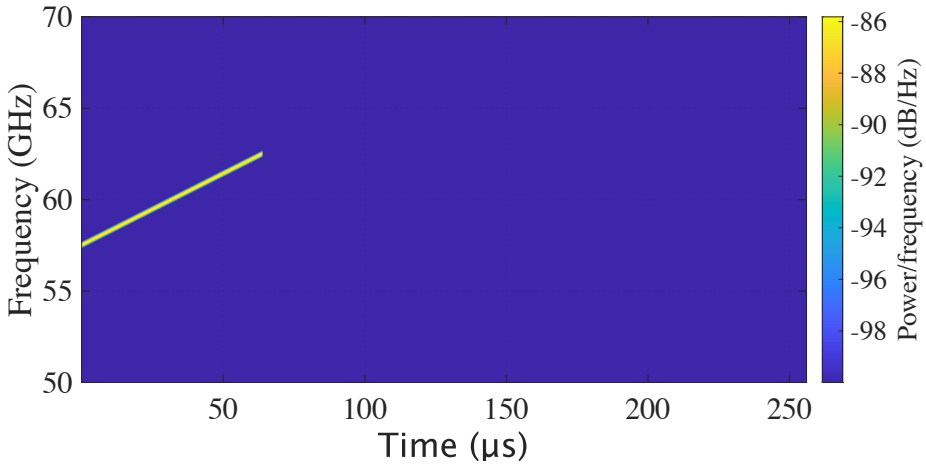


Figure 4-14 An overview of the general system architecture of an FMCW radar, the highlighted portion represents the Tx/Rx antennas and target that could be represented by the S-parameters.

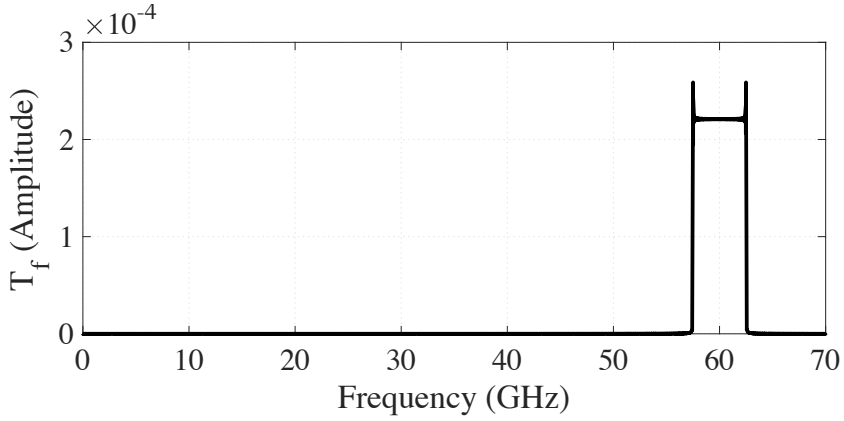
It is worth noting that the remainder of the components were considered ideal. Moreover, the noise effects were ignored. As these effects including noise and non-linearity would complicate the model significantly without contributing to our primary target of calibration and prediction. The codes generated and used in this section are provided in 0.

4.2.2 Verification Tests

Before attempting to apply the described calculation method to the S-parameters of the proposed sensor, it was crucial to conduct a series of verification tests to make sure that the concept and implementation were accurate. First of all, Figure 4-15 shows the spectrogram and spectrum of the generated Tx signal.



(a)



(b)

Figure 4-15 The (a) spectrogram, and (b) spectrum; of the generated Tx chirp.

As previously mentioned, the chirp has a duration of 64 us and spans a 5 GHz bandwidth around 60 GHz. Moreover, the duty chirp duty cycle is 14.6% resulting in a frame duration of around 440 us. However, in our calculations, a calculated frame duration of 250 us was selected to improve the computational power required. The reduced frame duration is acceptable given the small velocity/range values of our use case.

In the first verification test, we wanted to verify a simple case of a metallic reflector placed at a distance L from the radar. This scenario is analogous to the case of a short-circuit terminated transmission line of length L as shown in Figure 4-16. For simplicity, it is assumed that the transmission is matched to the characteristic impedance of the transmission line. Consequently, we are expecting to observe a single reflection with a time delay equivalent to the round-trip transient time of the transmission line.

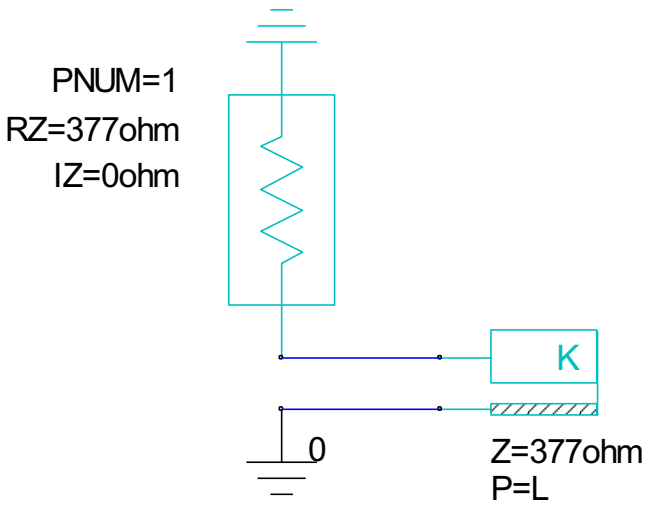


Figure 4-16 Circuit diagram of a transmission line with length L terminated by a short circuit.

The reflection coefficient from this scenario is described by (4-7), where Z_o is port impedance which equals the characteristic impedance of the transmission line Z_{TL}, and β is the propagation constant. It is worth noting that the choice of denoting the reflection coefficient of this one-port network as S_{21} was intentional to generalize to the case of different receiver and transmitter antennas. In our first test case, the S-parameter was calculated using (4-7) within the MATLAB script.

$$S_{21} = \frac{iZ_o \tan(\beta l) - Z_o}{iZ_o \tan(\beta l) + Z_o} \tag{4-7}$$

Figure 4-17a shows the spectrogram of the received signal when L = 200 meters, there is a very small time delay that's barely visible as it is equivalent to 1.33 us which is much smaller than the duration of the chirp/frame. Moreover, Figure 4-17b shows the amplitude of the spectrum of the received signal which is identical to that of the transmitted signal shown in Figure 4-15b. This is expected as in this test case, the transmission line is lossless i.e. ignoring free-space spreading loss (FSL), thus, only the phase would be affected. The spectrum of the IF signal, on the other hand, is sensitive to the time delay as the beat frequency corresponds to the range bin as described by (4-8); where c_o is the speed of light in vacuum, f_{IF} is the frequency of the beat frequency, and f_{chirp} is the instantaneous frequency of the chirp.

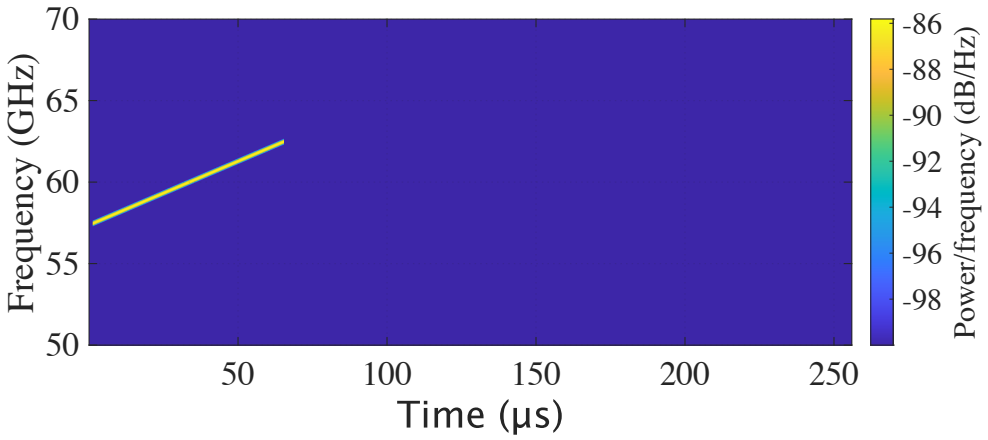
Figure 4-18a shows the amplitude of the spectrum of the IF signal for the short-circuit terminated transmission line test case when L=200 meters. As expected, there is a single beat frequency corresponding to a single target. Moreover, the frequency was 0.1041 GHz which correctly corresponds to a range of 200 meters as per (4-8). Then, we repeated the test for 400, and 600 meters which results are shown in Figure 4-18b and Figure 4-18c respectively. Similarly, the obtained beat frequencies corresponded to the correct range bins.

At this stage, we confirmed that the calculation could retrieve the range correctly. The next step is to check whether it can detect multiple targets from different ranges simultaneously. We have added a small change to the previous test by creating a mismatch between the transmission line characteristic impedance and the impedance of the port, resulting in the expression for the reflection coefficient depicted in (4-9). In this case, we are expecting there to be multiple reflections each a round trip delay apart. Moreover, we expect each reflection to be weaker in amplitude. Figure 4-19 shows the spectrogram of the received signal as well as the spectrum of the amplitude of the IF signal. As observed, there are multiple peaks (reflections), with decaying amplitude and at regular equal intervals corresponding to the 600-meter distance.

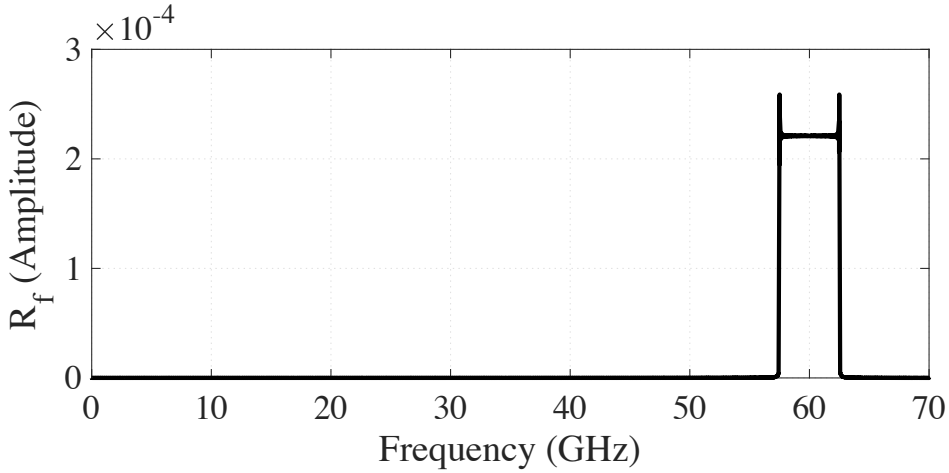
Now we have verified that our calculations can decode the information implicit within the phase of the S-parameters including multiple reflections and their amplitudes. The next step is

to verify that it can detect changes encoded in the amplitude of the S-parameters such as in the case of filters. In the next example, we added a bandpass filter between two sections of transmission lines connecting the transmitter and receiver as shown in Figure 4-20a.

it is worth noting that in this test case, we used the circuit simulator included in Ansys Electronics Desktop (the simulation suite of which HFSS is part). This circuit simulator provides the simulation results in the same format as HFSS, consequently, it also verifies some features of the code including file import, interpolation, and extrapolation.

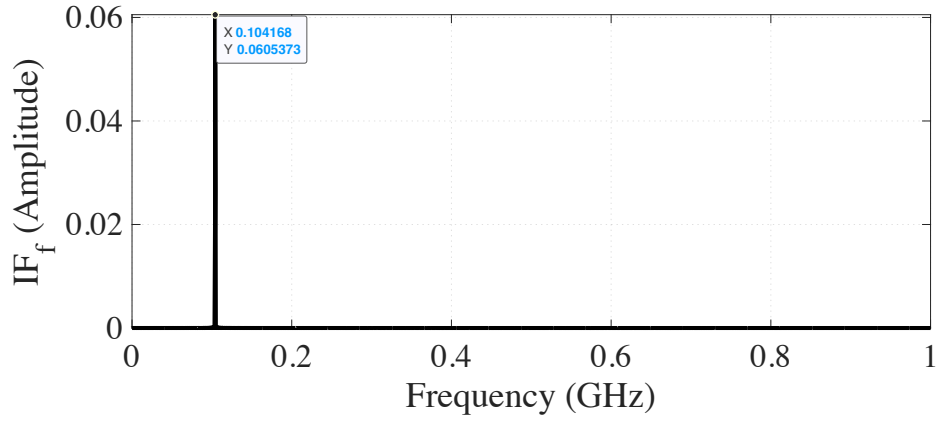


(a)

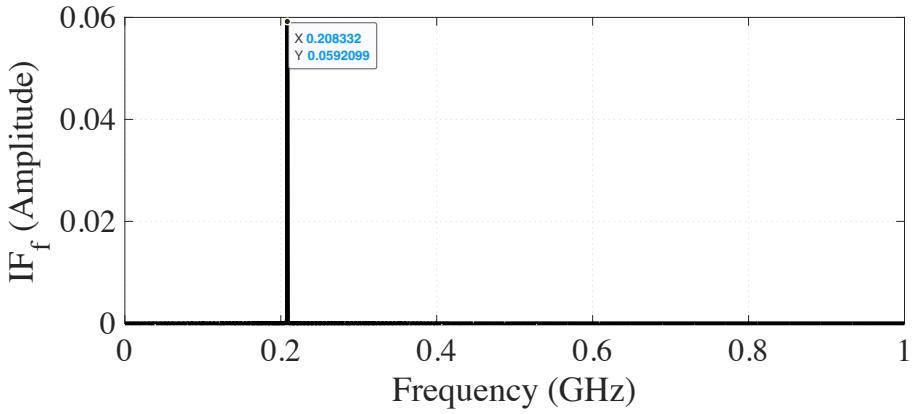


(b)

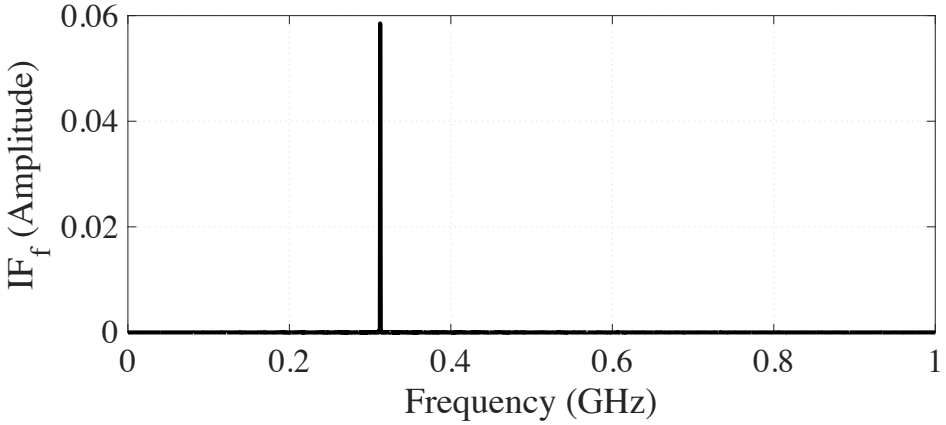
Figure 4-17 The (a) spectrogram, and (b) spectrum; of the calculated Rx chirp for L=200 meters.



(a)



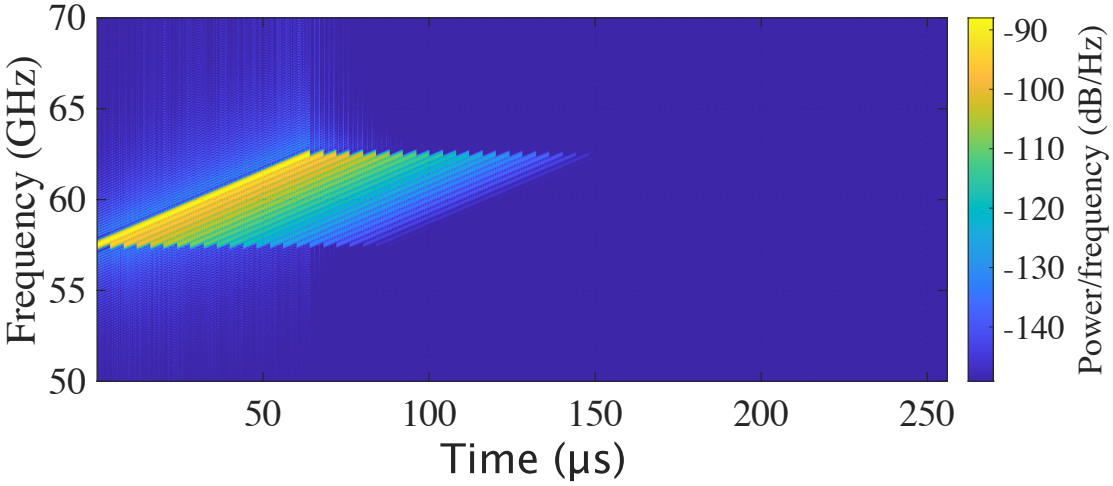
(b)



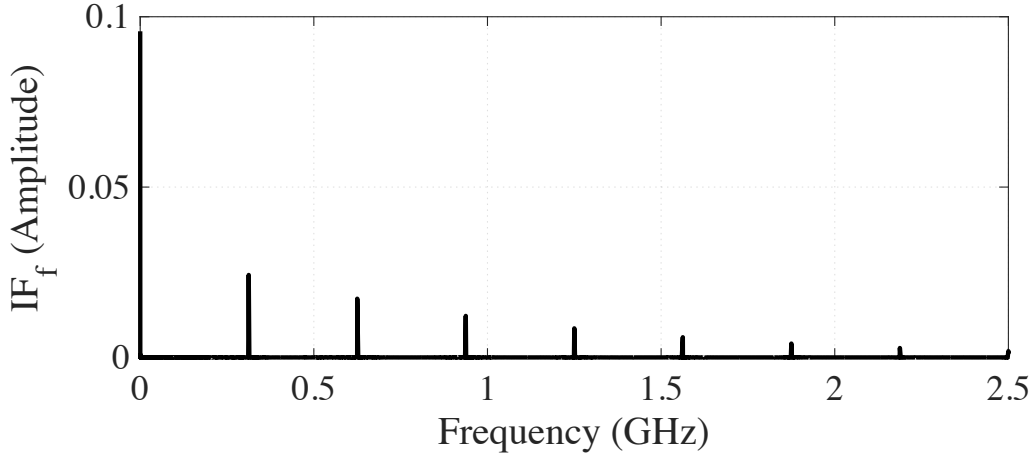
(c)

Figure 4-18 Spectrum of the calculated IF signal for the shorted transmission line test case at (a) L=200 meters, (b) L=400 meters, (c) L=600 meters.

$$R = \frac{1}{2} \cdot \frac{c_o \cdot f_{IF}}{\frac{\partial f_{chirp}}{\partial t}} \tag{4-8}$$



(a)

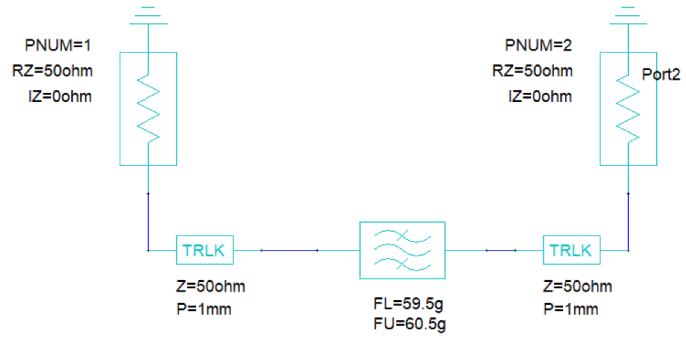


(b)

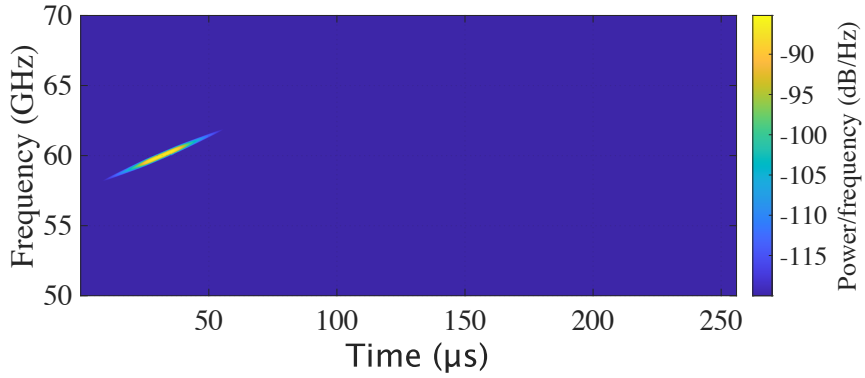
Figure 4-19 The (a) spectrogram of the Rx, and (b) spectrum of the IF; signals for the mismatched transmission line test case showing multiple reflections with decaying amplitudes.

$$S_{21} = \frac{iZ_{TL}\tan(\beta l) - Z_o}{iZ_{TL}\tan(\beta l) + Z_o},\ Z_{TL} \neq Z_o \tag{4-9}$$

Figure 4-20b shows the spectrogram of the received signal, as expected only a portion of the chirp around 60 GHz was transmitted to the receiver. Moreover, looking at the spectrum of the IF signal, we can see a single beat frequency at a very low frequency when the length of the transmission line sections is very small as in Figure 3-20a when the *L* (the total length) was just 2 mm. Moreover, when the *L* was increased to 100 meters, we can see the main peak at 0.026 GHz which corresponds to a round trip of 100 meters total as seen in Figure 3-20b. However, we can also observe some smaller phantom reflections that don't correspond to anything in the circuit. These phantom reflections were due to under-sampling in the phase of the S-parameters as the 100-meter length created phase wrapping transitions much quicker than the 20,001 frequency points of the circuit simulation captured. Nonetheless, this effect is not significant for this work the distances would be in the mm range, thus, this effect should not be a concern.

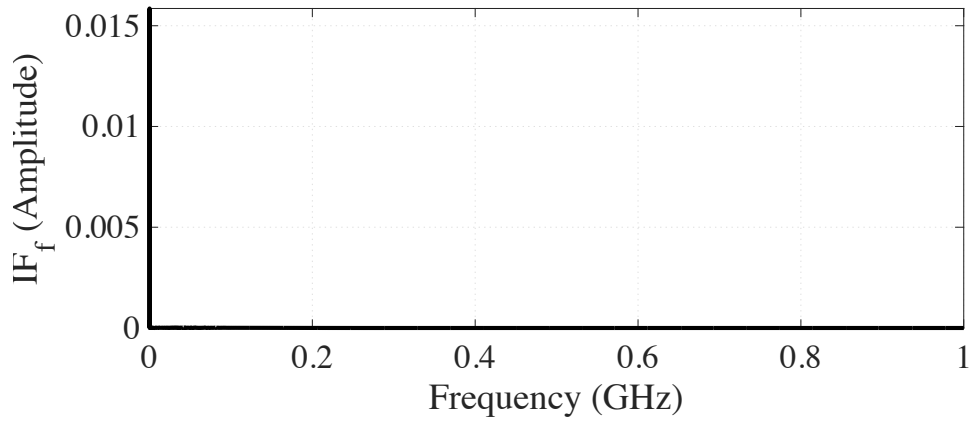


(a)

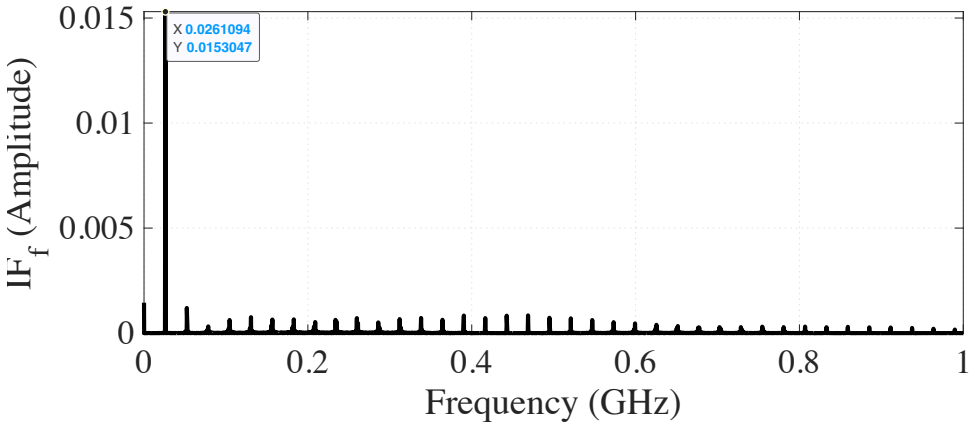


(b)

Figure 4-20 The (a) schematic, and (b) calculated spectrogram of the Rx signal, for the bandpass filter test case.



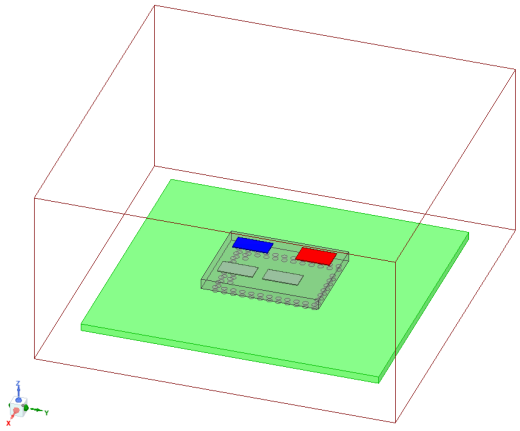
(a)



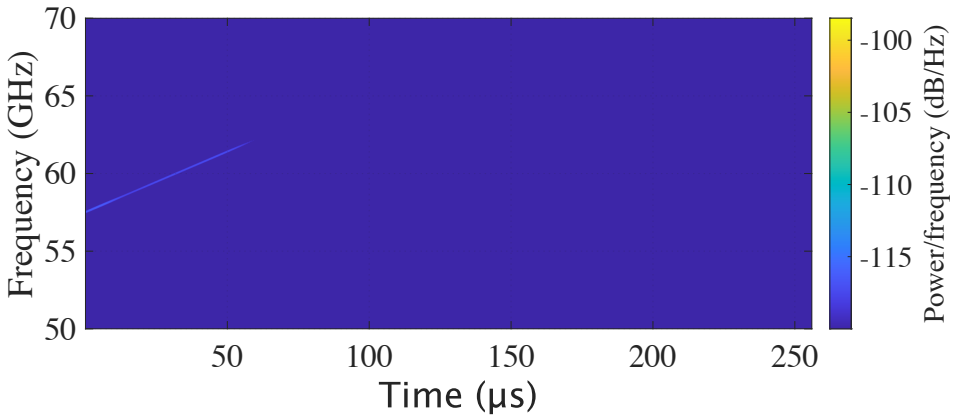
(b)

Figure 4-21 Spectrum of the calculated IF signal for the bandpass filter test case at (a) L=1 mm, and (b) L=100 meters.

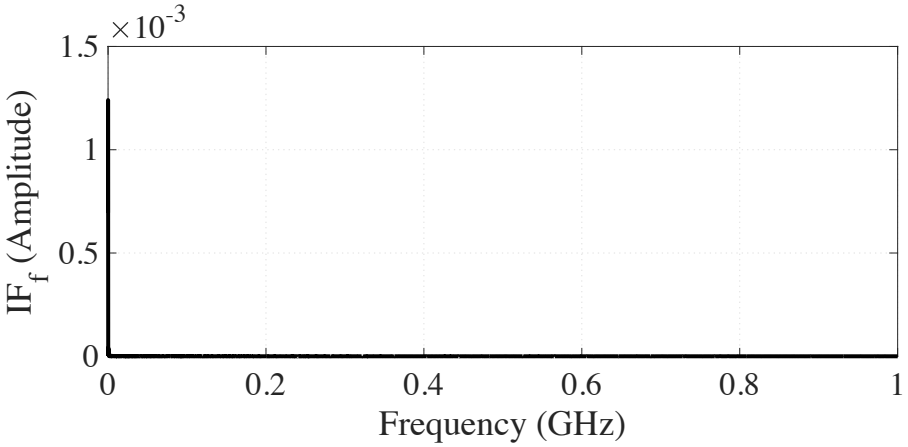
At this stage, we are confident in the model and can switch to results obtained from EM simulations through HFSS. The first test case was that of the bare Infineon radar using the model described in Chapter 3 and shown in Figure 4-22a. Then, we exported the transmission coefficient between the transmitter and 2nd receiver antenna ($S_{RX2,\ TX}$) and imported it into MATLAB v.2023b for calculation. As seen in Figure 4-22 (b) & (c), there is a very low power coupling occurring between the transmitter and receiver with the radiation boundary conditions. Moreover, this coupling had a very low beat frequency due to the proximity between both antennas.



(a)



(b)



(c)

Figure 4-22 The (a) 3D-model, (b) spectrogram of the Rx signal, and (c) spectrum of the IF signal; for the bare radar test case.

Unlike circuit simulations and ideal mathematical formulations, EM simulations allow for the exploration of the performance of the radar under near-field stimuli. Therefore, for our next test case, we are placing a metal plate in very close proximity to the radar. In this test case, we aim to confirm whether our model is capable of accurately representing changes in the near-field of the radar as our proposed sensor is in the near-field. Figure 4-23a shows the 3D model of the radar aboard along with a suspended metal plate at 12 mm. Figure 4-23b shows the calculated IF spectrum for the 12 mm plate test case, there is a single visible beat frequency at 19.53 kHz which corresponds to 37.5 mm. However, this difference between the calculated and actual ranges can be attributed to the decreased propagation constants in the near field which could result in distance over-estimation. This is not a limitation of the mapping between the S-parameters and IF spectrum, instead, the expression for range calculation shown in (4-8) is simply not valid in the near-field. Consequently, we increased the separation between the plate and the radar to 25 mm, and indeed we could see that the beat frequency has shifted as shown in Figure 4-23c. There was an additional beat frequency peak that is due to the direct path between the transmitter and receiver as shown by comparing it to the bare radar response as shown in Figure 4-23d. The new beat frequency is 27.34 kHz which corresponds to 52.5 mm which is 15 mm further than the 12 mm case. Provided that the range resolution of the radar module is 3 mm, the 15 mm value represents the closest range bin to the 13 mm actual displacement, thus, it is very acceptable.

4.2.3 Sensor Calculation

Now, we are confident that the calculation method along with the EM simulations provides us with reasonable and accurate results even in the near field, we can apply them to the results of the sensor presented in Chapter 3. Figure 4-24 shows the spectrum of the IF signal at different points of the design stage. First, we had the bare radar that showed a very attenuated power level due to the coupling between the transmitter and receiver antenna. Introducing the superstrate with the bridge significantly increases the coupling between the transmitter and the receiver as the power flows from the Tx antenna through the couplers and bridge to the receiving antenna. Finally, the defective ground structure (DGS) resonator presented in section 3.3.2, exhibits a

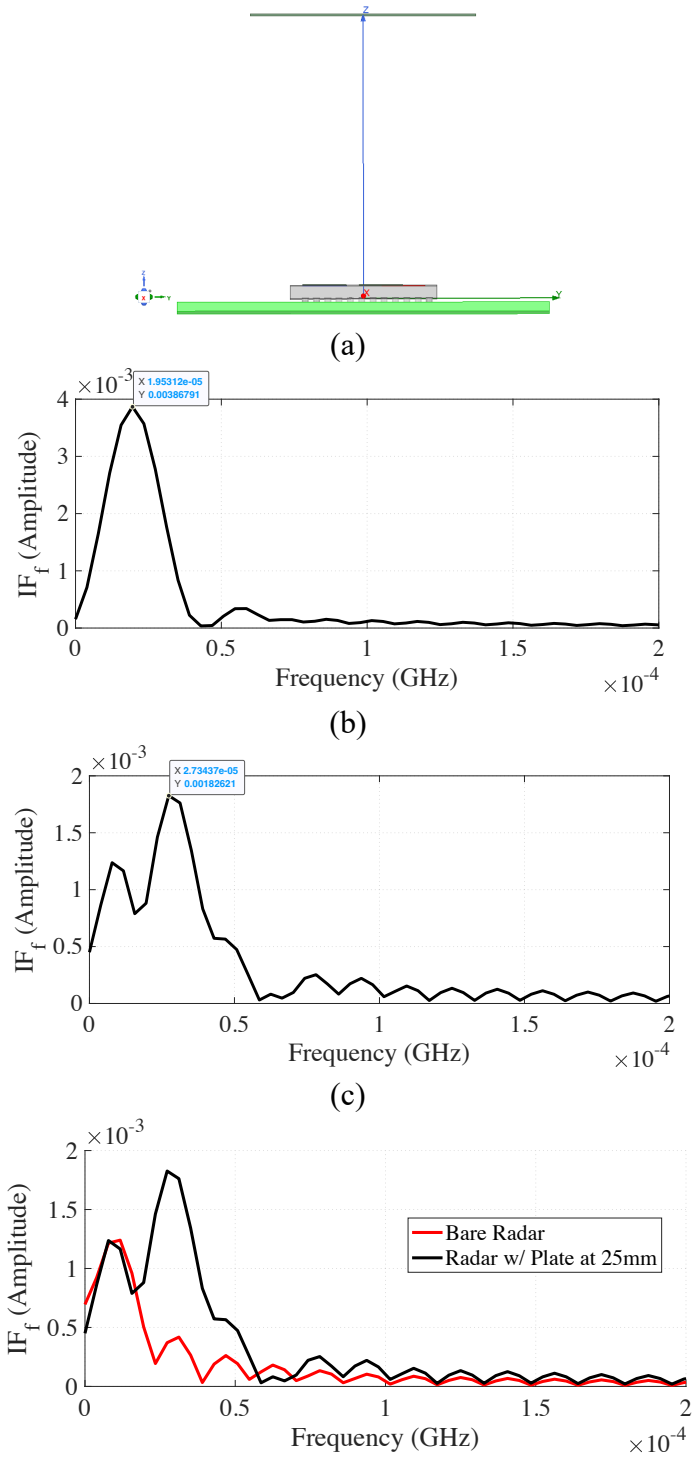


Figure 4-23 (a) 3D model of the radar w/plate test case, and The IF spectrums with the plate at (b)12 mm, (c) 25 mm, and (d) comparison with the bare radar.

stop band behavior at its resonance frequency, thus, the total power coupled to the receiver decreases as shown in Figure 4-24.

It is worth noting that the superstrate design consists of multiple resonating structures whose fundamental principle of operation is multiple reflections. However, the compact size of the superstrate structure relative to the specifications of the radar consolidates most of these reflections into a single beat frequency. This beat frequency's amplitude and phase have all the system's response encoded. Consequently, it could be feasible to extract the pulse waveform as it alters the response of the superstrate.

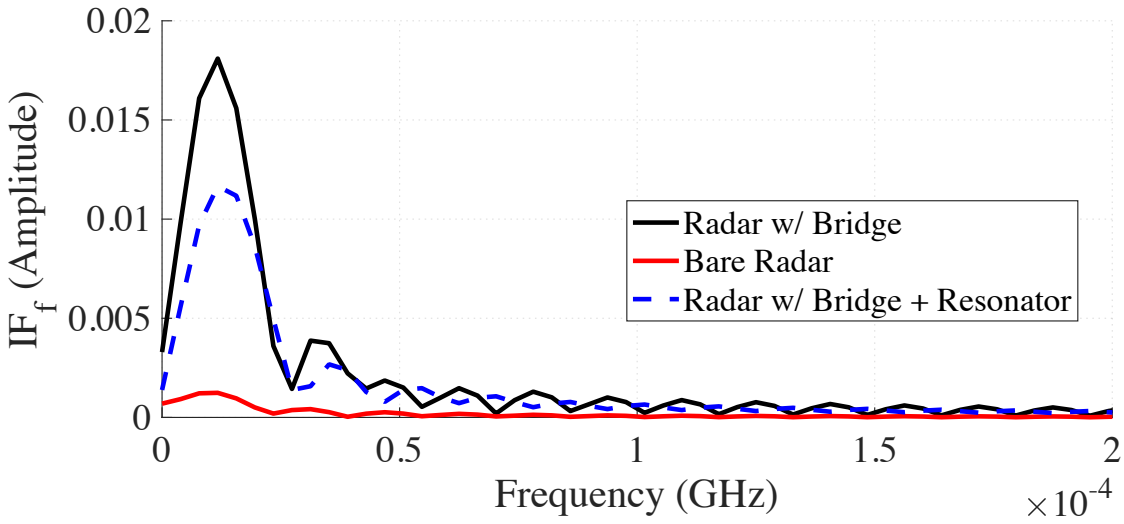


Figure 4-24 The Spectrum for the IF signal w/ & w/o different superstrate elements.

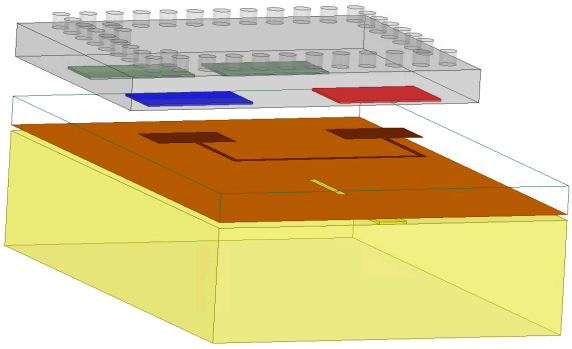
In the next step, we added the skin layer to the simulation model including the radar module and superstrate as shown in Figure 4-25a. The thickness of the box representing the pulse was swept vs time as described by (3-1) to simulate a typical pulse waveform. Then, we applied the described algorithm to the resulting transmission coefficient, thus, obtaining the IF spectrum shown in Figure 4-25b. Moreover, the IF spectrum showed a noticeable change in the amplitude/power of the primary beat frequency v.s. time. Figure 4-25c shows a change in the amplitude of the IF spectrum peak vs time in comparison with the input pulse waveform. It is observed that there is a clear correlation between the displacement and the response of the radar. Therefore, this amplitude could be used for a sensing decision and pulse waveform reconstruction. It is worth noting that there is some calculation noise in the signal due to

residual numerical error in the EM simulation. Table 4-2 shows the simulation options used in these simulations.

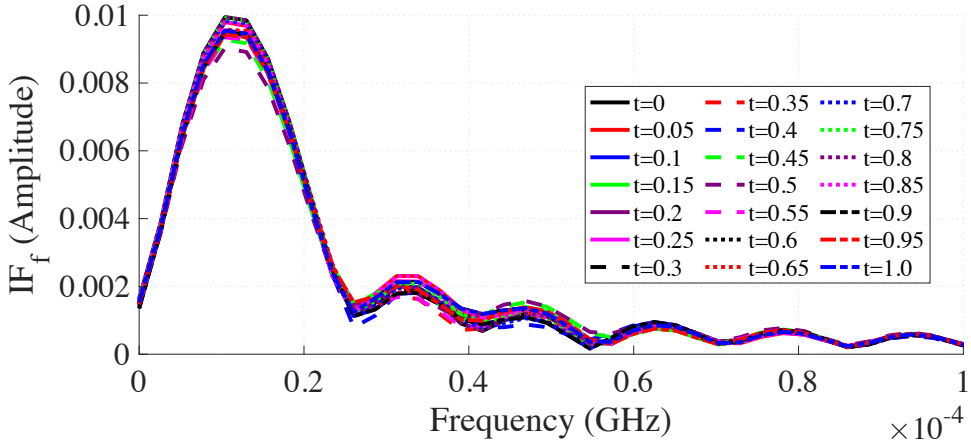
Thus far, we have shown how the sensor with the superstrate would perform under the pulse stimuli. However, it is important to investigate whether there is an improvement in the performance that would justify the added complexity. Figure 4-26 shows the amplitude of the IF spectrum vs time under the pulse stimuli for both the radar w/ & w/o the superstrate. It is clearly shown that there is an excess of an order of magnitude difference in the power level of either case. Consequently, there are significant benefits in terms of signal-to-noise ratio and the overall ability to sense. Moreover, the amount of change in the amplitude is also improved with the introduction of the superstrate compared to the case of the bare radar. Therefore, in Chapter 5, we present the manufactured prototype and conduct a measurement campaign using the superstrate-enhanced radar to verify its real-world performance.

Table 4-2 HFSS simulation parameters.

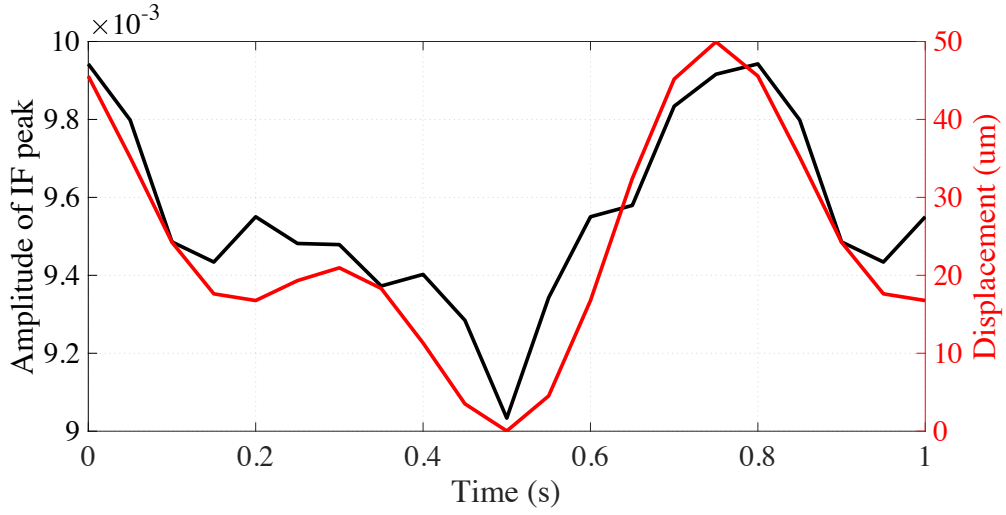
	Parameter	Value	Unit
Setup	Solution Frequency	70	GHz
	Maximum ΔS	0.005	-
	Consecutive Converged Passes	2	-
Frequency Sweep	Start	50	GHz
	End	70	GHz
	Number of points	20001	-
	Type	Interpolating	-
	Error	0.01	%
Time Sweep	Start	0	Seconds
	End	1	Seconds
	Step	0.05	Seconds



(a)

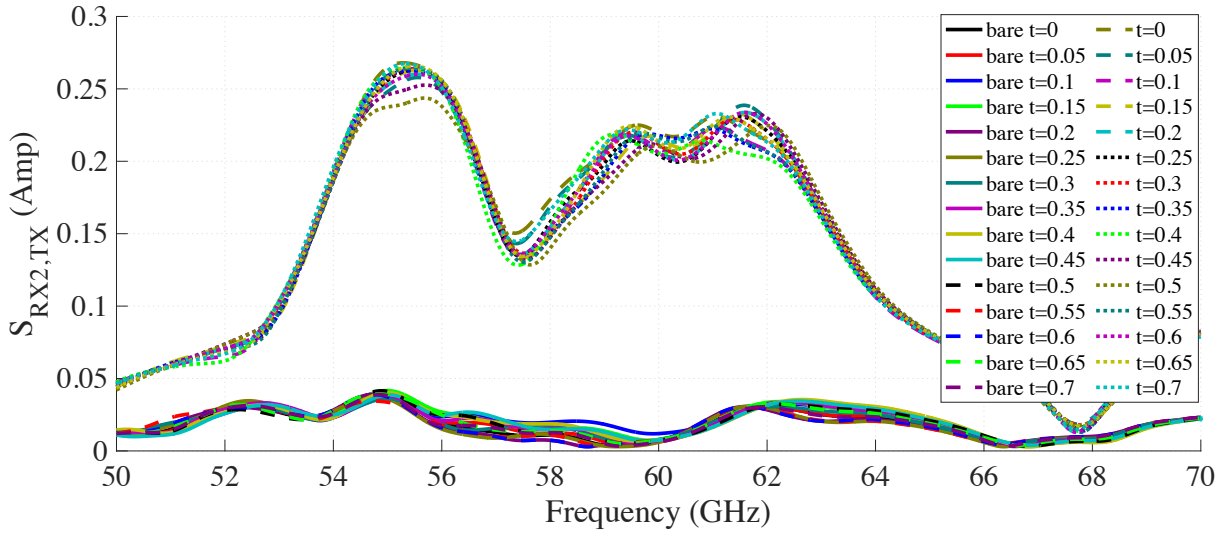


(b)

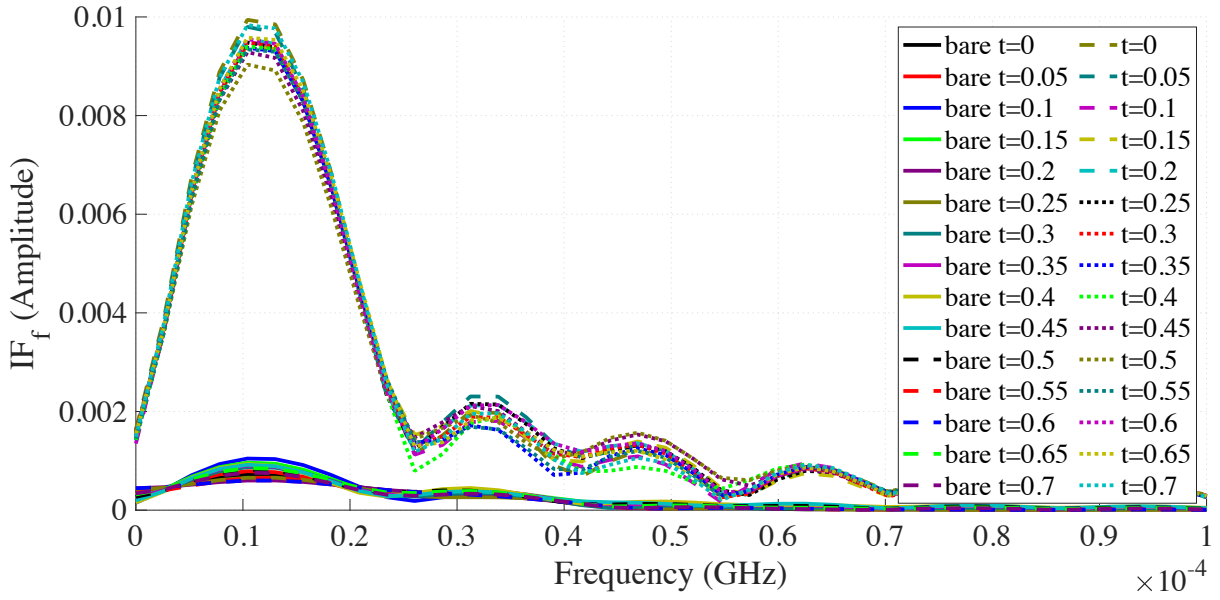


(c)

Figure 4-25 (a) The 3D model of the proposed DGS superstrate including the skin layer and pulse box. (b) The amplitude of the IF spectrum at different slow time points, and (c) The amplitude of the IF spectrum peak compared to the input displacement waveform.



(a)



(b)

Figure 4-26 A comparison between the (a) S-parameters, and (b) IF spectrum in the response of the superstrate vs bare radar in response to the pulse stimuli.

Chapter 5

Measurement Campaign & Results

5.1 Hardware Equipment & Experimental Setup

In this section, we will describe the equipment used in the measurement campaign including the sensor prototype assembly as well as the commercial device used to measure the ground truth electrocardiogram (ECG) used to capture a reference ground truth.

5.1.1 Frontier X activity monitor

The Fourth Frontier's Frontier X is a patented health monitoring belt designed to provide real-time feedback on cardiac and respiratory health during exercise. The belt is worn around the torso, beneath the pectoralis muscle, as depicted in Figure 5-1. It was used in this study to provide a benchmark for comparing data collected by radar for Heart Rate (HR). Furthermore, the Frontier X was used to continuously capture ground truth Heart Rate Variability (HRV), and electrocardiogram (ECG) data, which was then mapped against radar cardiac displacement waveforms to correlate cardiac events during the cardiac cycle. The ECG data was collected using a single-lead dry electrode. Although this method is not as accurate as those commonly used in clinical settings, it is still reasonably accurate for comparison purposes [45].

Several factors influenced the choice of the Frontier X belt despite its torso location. First, its placement on the torso guarantees that it does not interfere with the placement of our sensor which significantly influences the results as shown in section 5.2.2. Moreover, its ECG capabilities provide sufficient information to evaluate the obtained signals in terms of HR, and HRV. In future work, a more specialized sensor like the CNAP blood pressure monitor [46] used in [8] may be used in tandem with the frontier belt.

The Frontier X transmits the collected biometric data to both a mobile and web application, where users can view data analytics or download the raw data for plotting. The system calculates the heart rate by detecting the timing between ECG R-peaks as shown in Figure 5-2 within an approximately 20-second window interval. The root mean square of the successive differences (RMSSD) method, as described in (5-1), is used to calculate HRV. This method finds the time difference between successive heartbeat intervals (HBI), where N represents the number of heartbeats in each window [47]. It's worth noting that HRV, the variation in time intervals between successive heartbeats, provides valuable insights into the activity of the autonomic nervous system, which regulates the heartbeat [48]. The resulting RMSSD value represents the magnitude of short-term variability in HBI, with higher values indicating greater variability and stronger parasympathetic activity.



Figure 5-1 Frontier X2 health monitor by Fourth Frontier [47].

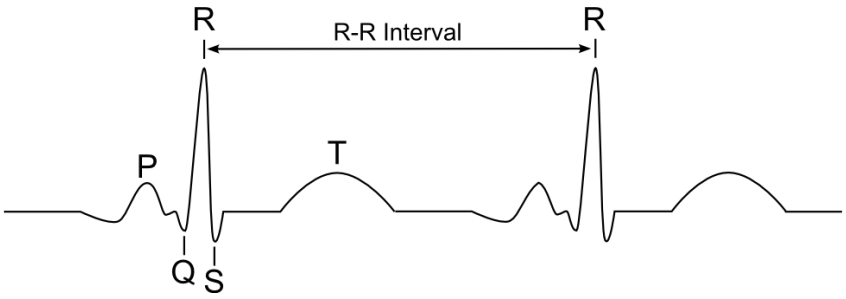


Figure 5-2 The definition of R-R Interval in ECG [49].

$$RRMSD = \sqrt{\frac{1}{N-1}\sum_{i=1}^{N}\left(RR_{i+1} - RR_i\right)^2} \tag{5-1}$$

5.1.2 Manufactured Prototype

In the previous chapters, we presented a design of a PCB superstrate that would be suspended above the Infineon radar module for pulse sensing. In this section, we will describe the fabrication and assembly process for the proposed sensor.

The first step is to capture the physical dimensions of the radar module and its companion USB evaluation board. A vernier caliper with a precision of 0.01 mm was used in measuring the dimensions as shown in Figure 5-3 where L_{PCB} =40.68mm, W_{PCB}= 25.41mm, $W_{h\text{-}h}$=*20mm*, $\varnothing_{hole}$= *2mm*, r_{edge}= *1.4mm*, t_{total}= *4.57mm, and* t_{PCB} = *1.2mm*. These dimensions were then used to extend the layout of the superstrate PCB to match that of the radar evaluation board including the three through holes whose position would guide the alignment of the couplers and their corresponding antennas on the radar as shown in Figure 5-4.

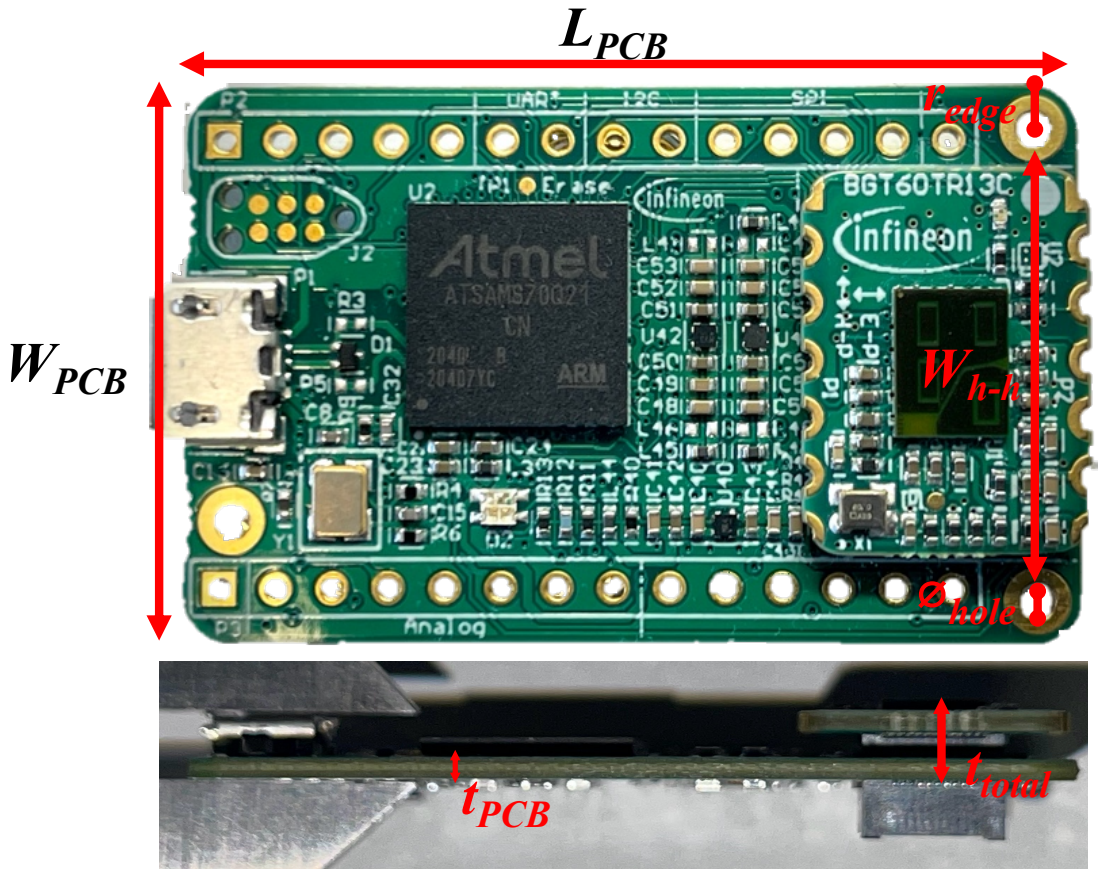


Figure 5-3 Photograph of the radar PCB including the USB evaluation board.

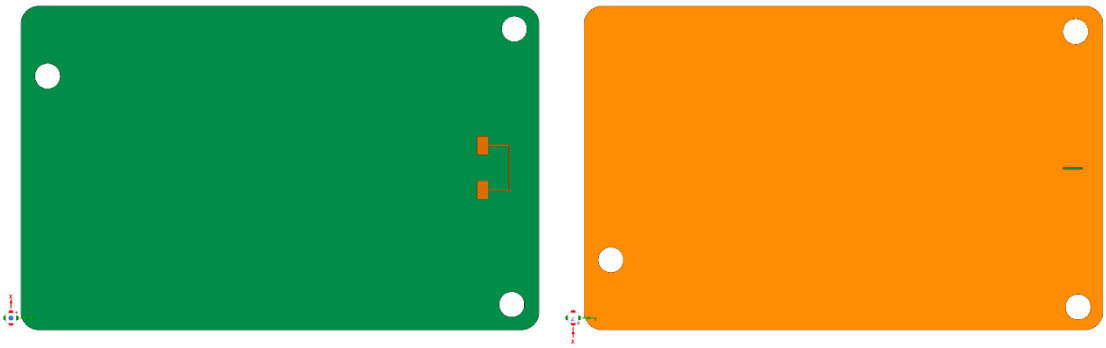


Figure 5-4 Layout of the PCB superstrate sent for fabrication.

The layout was then fabricated on a Rogers 4003C substrate, with a dielectric thickness of 0.508 mm, and a conductor thickness is 40.6 um, thus, the total thickness of the PCB is 0.60 mm +/- 0.1mm. To improve the post-fabrication design tunability to account for the dispersive nature of the dielectric properties of the substrate, the length of the slot was extended. Moreover, several ($0.3x0.3mm^2$) cut-outs were created in the solder mask of the bottom layer, hence exposing the copper layer, these cut-outs had a period of 0.5 mm as shown in Figure 5-5.

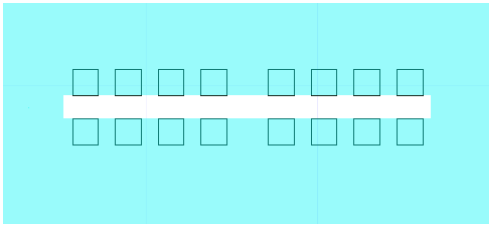


Figure 5-5 Layout of the solder mask cut-outs relative to the slot.

To fix the relative location of the superstrate to the radar module, we designed a mounting bracket to attach the radar and the superstrate. Moreover, it would suspend the superstrate above the radar module's PCB for contactless coupling. The bracket would also include placeholders for the straps to be worn around the participant's wrist. Figure 5-6 shows the 3D model for the mounting bracket. The bracket has 3 holes corresponding to the PCB's holes. The thickness of the bracket is 4 mm, which leaves a 0.66 mm separation between the radar antennas and the superstrate similar to the 0.7 mm included in the simulations. Moreover, there is a cut-out for the Micro-USB type B port of the evaluation board. Finally, there are cut-outs

on the edges of the bracket to be attached to the Velcro strap tied around the arm. Finally, the assembled prototype is shown in Figure 5-7.

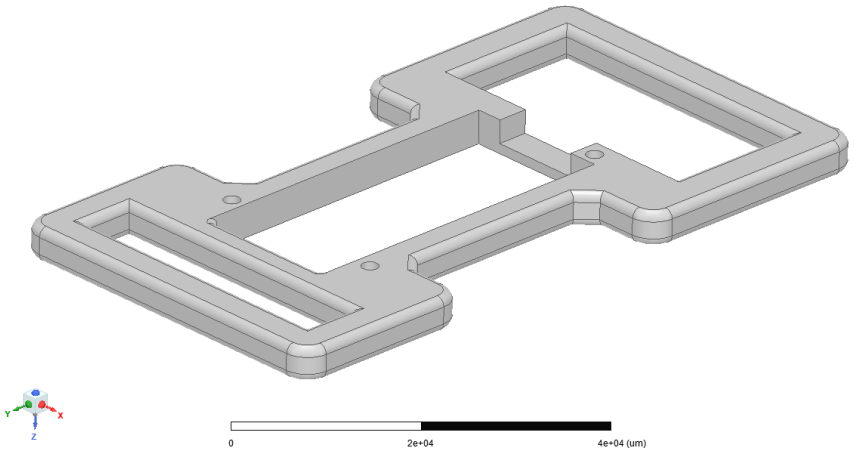


Figure 5-6 3D Model of the PCB standoff and mounting bracket.

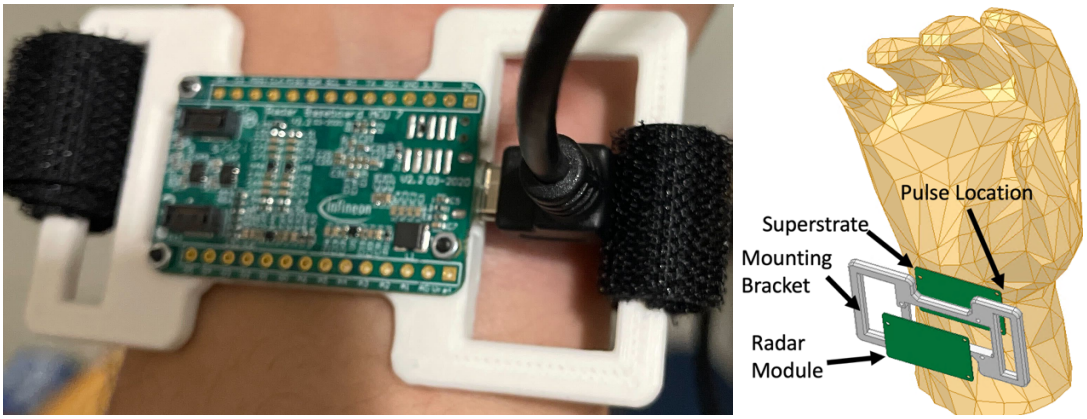


Figure 5-7 A photograph of the assembled prototype.

5.2 Radar Measurements and Pulse Waveform Extraction

This section presents the process of verification for the manufactured prototype. Moreover, it presents preliminary results for the pulse waveform measurement and extraction on 6 healthy participants.

5.2.1 The Effect of the Superstrate on the Radar Response

The first verification step is to measure the effect of the superstrate on the measured chirps before the introduction of the skin. To conduct this test, the radar module was placed on a flat surface with the antennas facing the ceiling 2 meters away. Using the Radar Fusion Kit and

Radar Fusion GUI [50] provided by Infineon, the radar parameters are set to the configuration summarized in Table 5-1. The bandwidth was set to the maximum of 5 GHz so that it corresponds to a range resolution of 3 cm. Moreover, the frame duration was set to 100 ms to match the sampling time step in the simulations. Additionally, it provides an exact number of frames for the capturing duration of 10 seconds. It is worth noting that an older version of the Radar Fusion GUI, specifically V3.3, is required as the functionality to export RAW CSV output was removed in later versions.

Table 5-1 Radar Configuration in Measurements.

Parameter	Value	Unit
Start Frequency	58	GHz
End Frequency	63	GHz
Bandwidth	5	GHz
Tx Power Level	-2 (10/31)	dBm
IF Amplifier Gain	18	-
Number of Chirps per frame	64	-
Number of Samples per Chirp	64	-
Frame Duration	100	ms
ADC Sampling Rate	2	MHz

Figure 5-8 shows a comparison between the normalized ADC output for a single chirp before and after the introduction of the superstrate to the radar module. As observed in Figure 5-8, the power level measured by the radar is higher after the introduction of the superstrate. Moreover, there is a pattern resembling the S-parameters such as the band stop at the start of the chirp followed by a somewhat flat response then finally, it declines again towards the end of the spectrum. This is unlike the direct coupling between the transmitter and receiver in the absence of a reflection which is relatively flat.

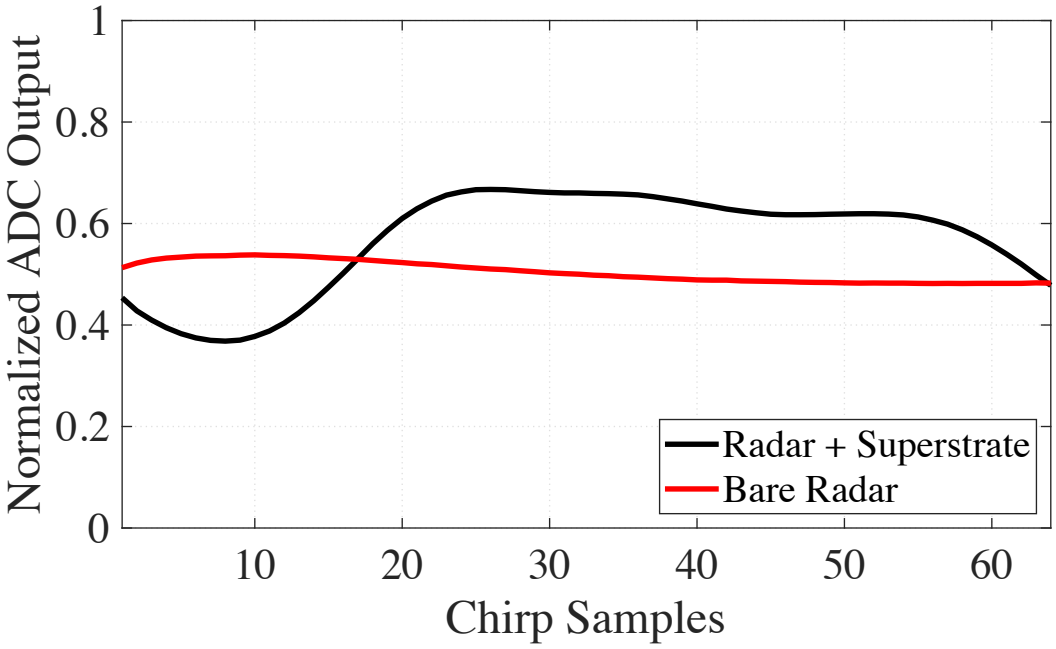


Figure 5-8 Comparison between the raw output of the radar before and after the introduction of the superstrate.

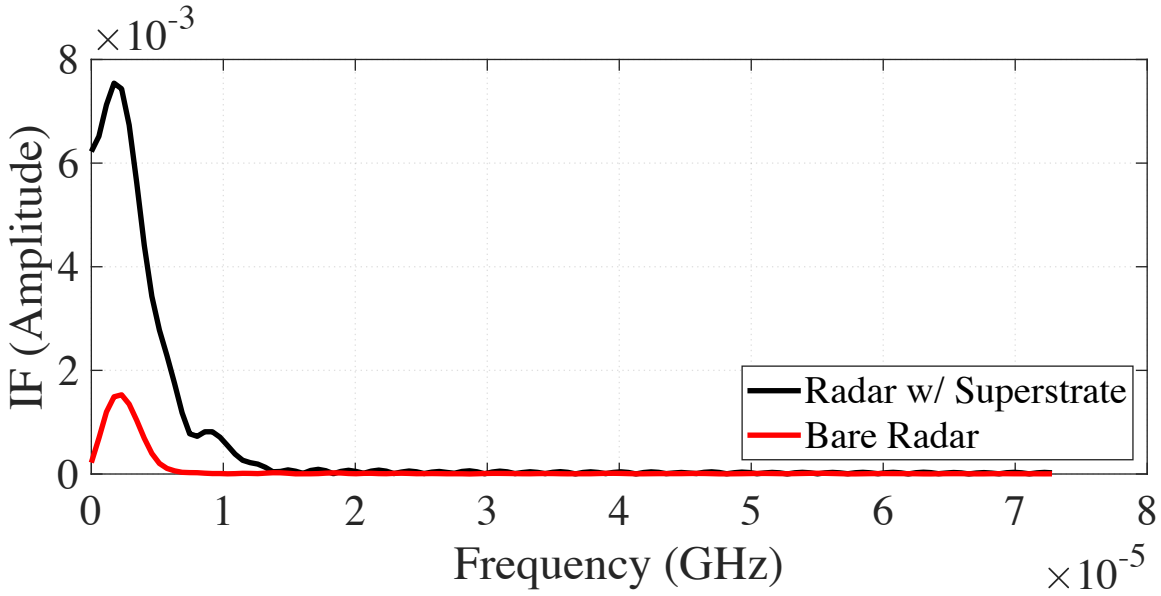


Figure 5-9 The measured IF spectrum after mean removal w/ & w/o superstrate.

Then, the RAW ADC output was imported into MATLAB v.2023b, where a Fast Fourier Transform (FFT) was conducted to obtain the IF spectrum as shown in Figure 5-9. The number of FFT points is 256 with a hamming windowing. Moreover, the mean in the time domain was

removed for DC suppression in the spectrum. The obtained IF spectrum matches our expectation of the similar spectrum shown in Figure 4-24 where the IF peak is significantly higher after the introduction of the superstrate due to the coupling path created between the transmitter and receiver through the couplers and the bridge.

One of the main motivations for implementing the superstrate is to isolate the radar from the harsh environment of direct skin contact. This is due to the dielectric constant of the skin being drastically different than the air interface it was designed for. To test whether this hypothesis was correct. The radar module was placed on the side of the abdomen where it would be in contact with the skin without a significant skin vibration being present. Figure 5-10 shows a comparison between the response of the bare radar and radar w/ superstrate before and after the placement on the skin.

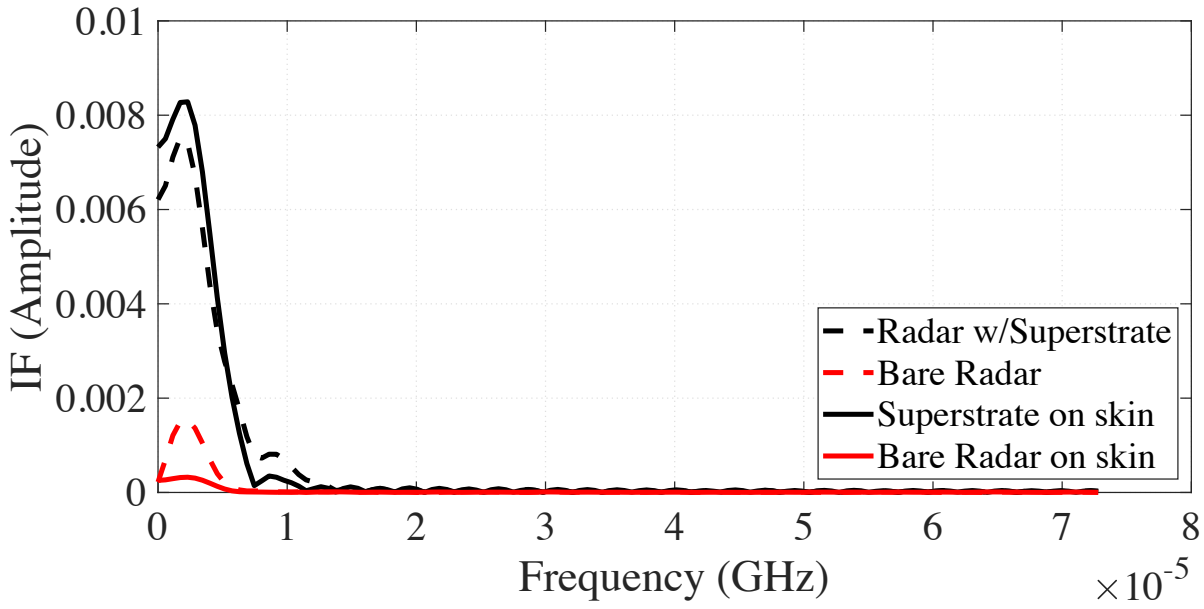


Figure 5-10 A comparison between the response of the radar before and after contact with the skin.

As observed in Figure 5-10, the amplitude of the IF peak deteriorated significantly for the bare radar compared to its performance in free space. In contrast, the response of the radar with the superstrate remained fully functional after the introduction of the skin. The increase in the peak power can be explained by increased transmission due to the decreased quality factor of

the resonator. This shows how the superstrate isolated the main operation of the radar from the environment while maintaining sensitivity.

5.2.2 Pulse Waveform Measurement and Reconstruction

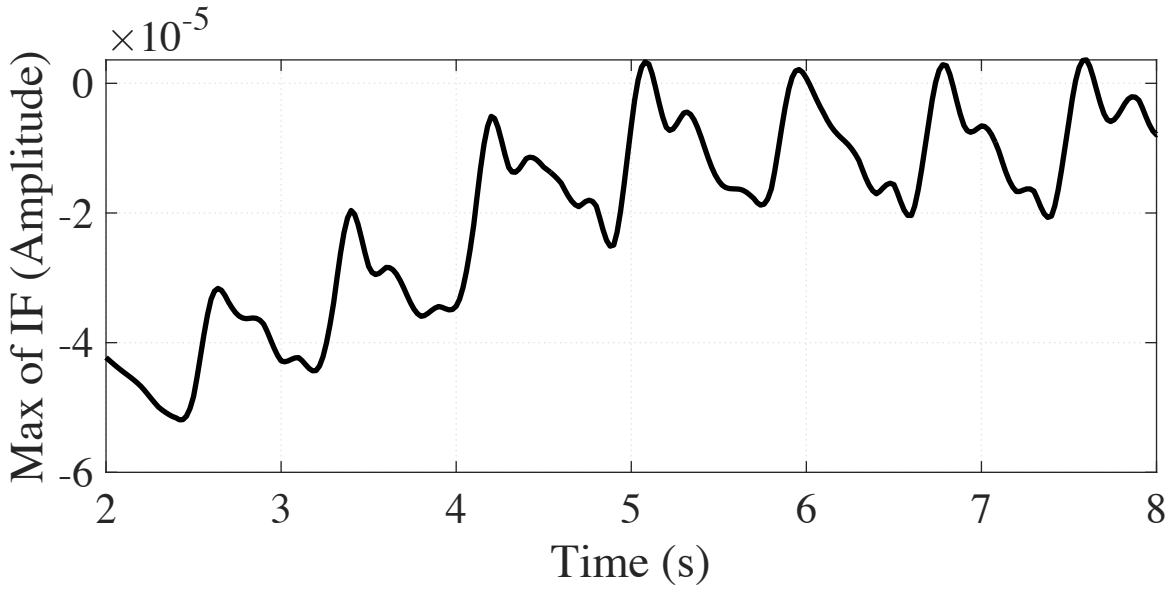
In the previous section, we have shown that the proposed superstrate protected the radar from the detrimental effect of direct skin contact. Moreover, it remained sensitive, and a change could be observed when it came in contact with the skin. The next step is to attempt to capture the pulse of a human participant when the sensor is worn on the wrist as shown in Figure 5-7

To decide on the placement of the sensor, the location of the pulse was first sensed using my fingers. The location of the pulse is then marked, and the sensor is placed such that the slot of the superstrate is aligned with the pulse. In the first measurement, we captured 10 seconds and repeated the measurement 3 times each moving the sensor slightly to capture the best alignment.

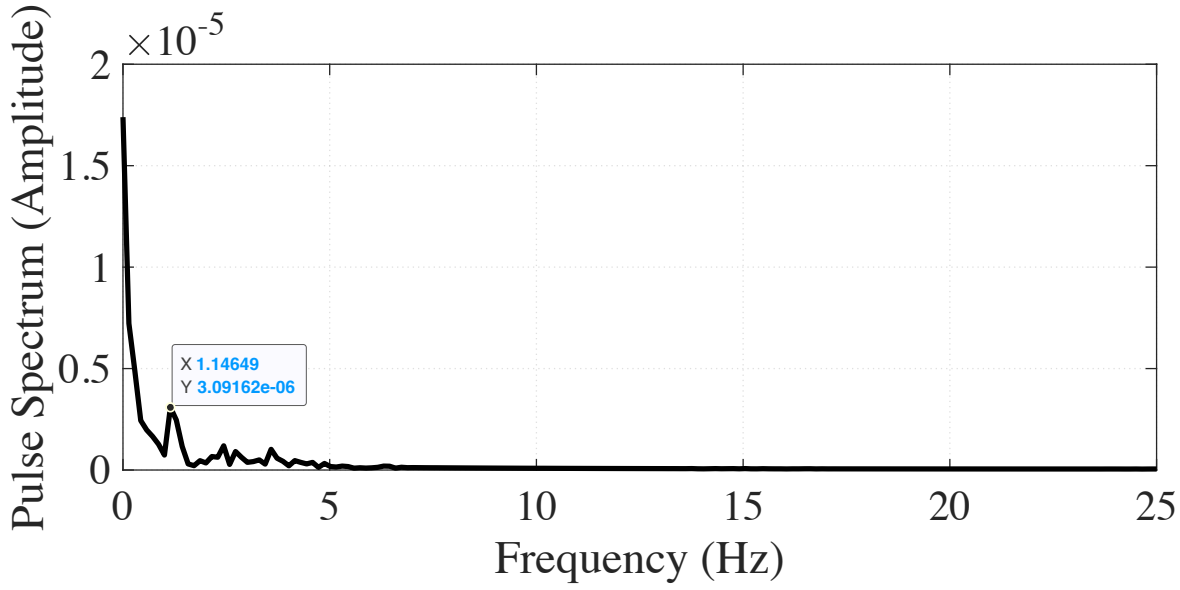
Figure 5-11a shows the resulting amplitude of the peak of the IF spectrum obtained from one of the measurements. As observed in the results, we can see multiple dual harmonic signals resembling the theoretical waveform described by (3-1). Moreover, by doing an FFT we can see that the main frequency of this signal is 1.146 Hz corresponding to 68.76 bpm as shown in Figure 5-11b. This frequency is realistic and makes physiological sense.

Next, the measurement is repeated now the ground truth was also captured using the Frontier X described in section 5.1.1. The same procedure is repeated where the pulse is first located manually, then the measurement is repeated 3 times, each time the sensor is moved slightly.

Figure 5-12 shows a comparison between the captured signal and the corresponding reference ECG signal. As seen, there is a perfect correlation between the period or repetition time of the measured signal and the ground truth. Hence, the sensor could be used to accurately estimate the R-R interval. In the 10sec window shown in Figure 5-12, both the measured pulse and ECG had an average peak-to-peak (r-r in ECG and systolic-systolic in pulse) interval of 0.68s i.e. 87 bpm. Moreover, the pulse still resembles a similar waveform to the expected theoretical PPG waveform. It is worth noting that a higher frame rate may be required to accurately capture the RRMSD as the 0.1s frame interval is too large compared to typical RRMSD values.



(a)



(b)

Figure 5-11 (a) the amplitude of the peak for the pulse measurement on the wrist and (b) the corresponding spectrum of the signal obtained in (a).

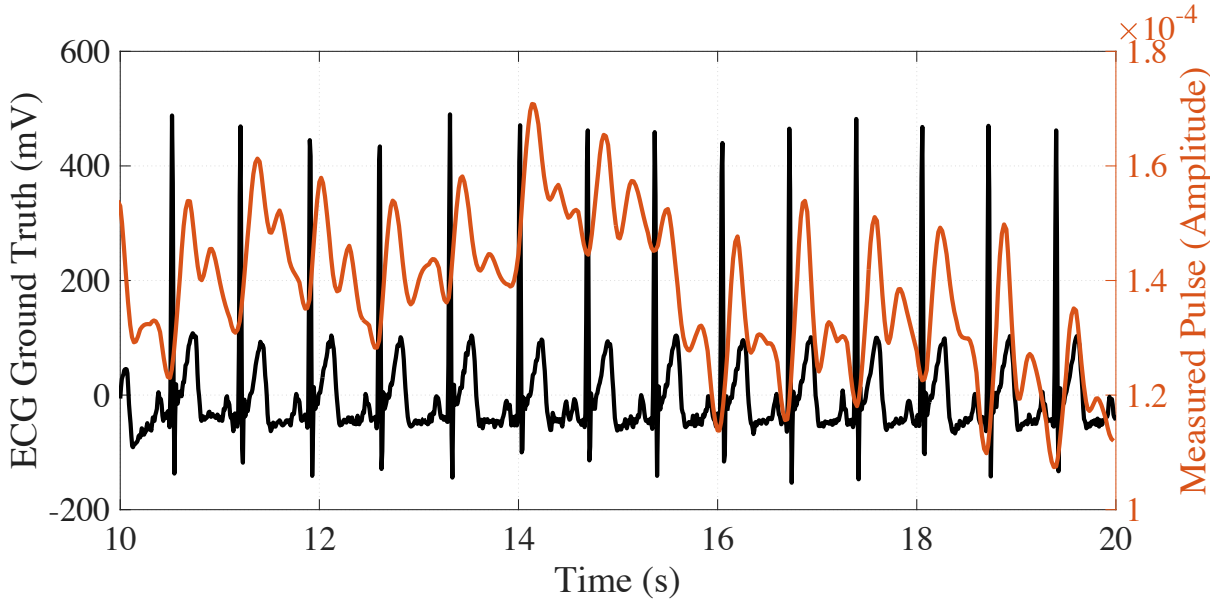


Figure 5-12 Measured pulse signal compared to the corresponding ECG ground truth for PT#1.

An interesting observation can be seen in Figure 5-12 in the pulse starting at t = 14s. Compared to the previous cardiac cycle, the ECG shows an additional peak. At the same time, the captured PPG waveform exhibited a similar additional peak in the same cardiac cycle. As per our understanding, the additional peak in the ECG may correspond to P-wave Bifid (P mitrale) [51], while the additional peak in the pulse may correspond to a late systolic pressure [52]. A Bifid P wave may indicate an enlargement in the left atrium of the heart [53]. The late systolic pressure, on the other hand, is related to Left Ventricular Hypertrophy (LVH) [54]. A 2019 study has found a correlation between LVH and enlarged atriums [55]. However, P mitrale and LVH are complex health conditions that should be examined by the appropriate cardiovascular expert before a conclusion can be made. Nonetheless, the occurrence was noted to be investigated in future clinical studies subject to oversight from a cardiovascular expert.

Alternatively, it is possible to extract the pulse waveform simply by tracking the amplitude changes for one of the samples in the chirp. This is similar to tracking changes in the amplitude of the transmission (S_{21}) at a specific frequency as presented in some of the results in Chapter 3. Figure 5-13 shows the amplitude of the 40th sample (corresponding to 61.125 GHz) in the last chirp of each frame compared to the corresponding ECG measurements. There is very good agreement between the timing of the measured pulse and the ECG measurements. This

real-time technique provides an enhanced computational and memory efficiency for measuring the pulse compared to the peak of the IF spectrum which required FFT and max operations as well as storage of all the samples. Moreover, it emphasizes that the sensing mechanism is raw power measurements as opposed to range bin amplitude/phase.

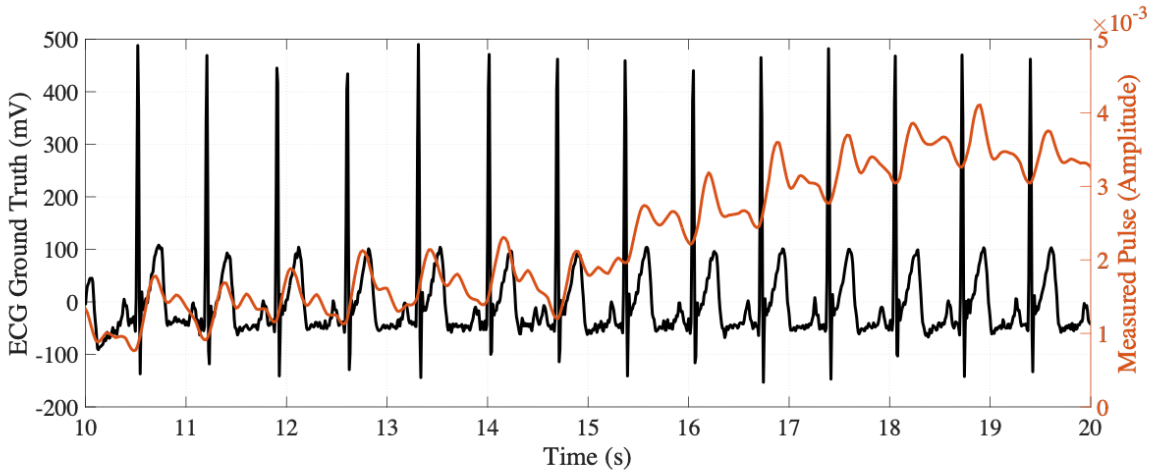
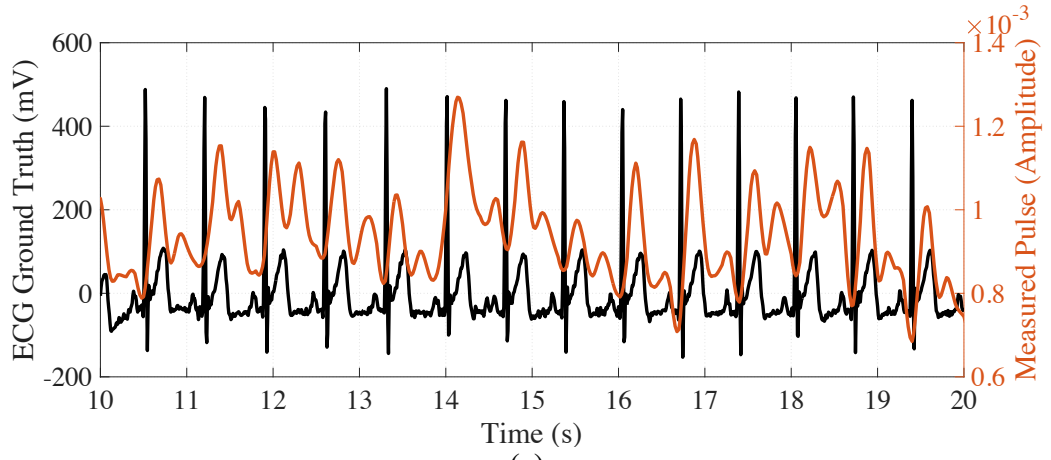
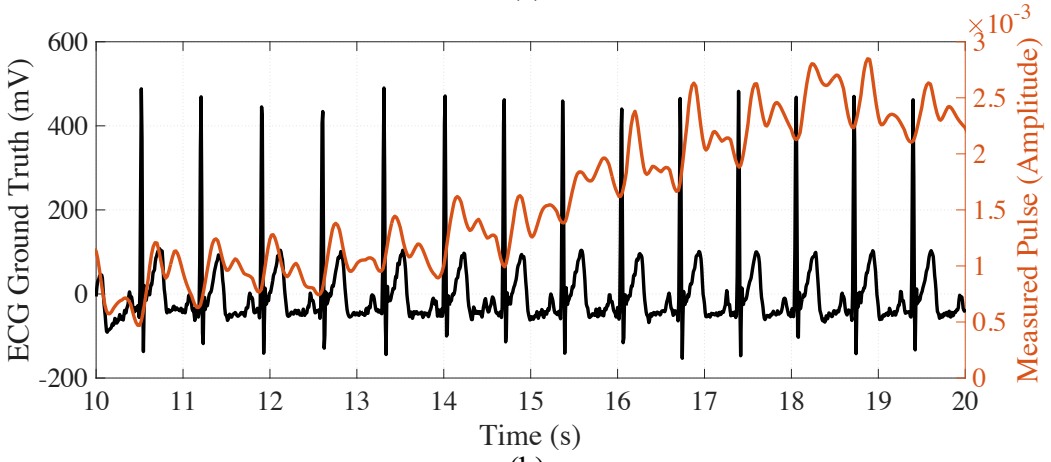


Figure 5-13 The power of the received signal at 61.125 GHz compared to the corresponding ECG ground truth for PT#1.

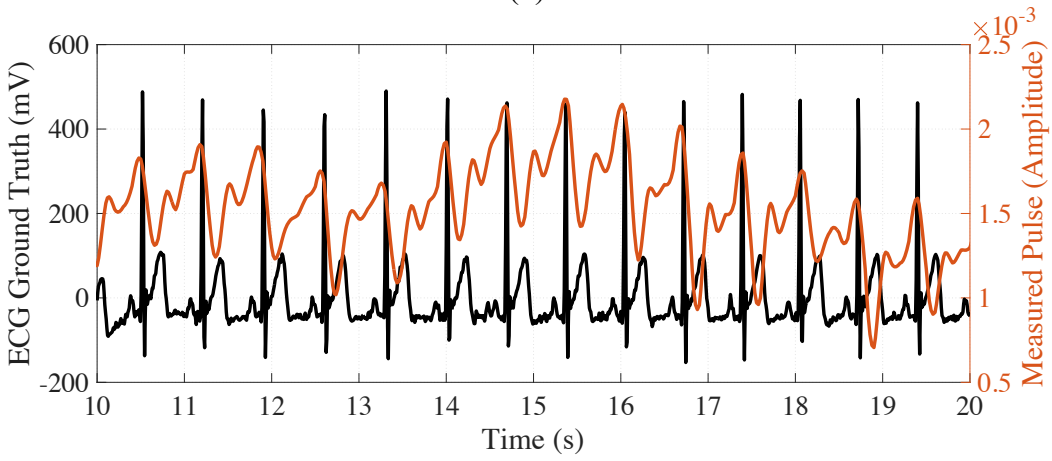
However, it is important to remember that despite them measuring the same phenomena, the responsivity of the amplitude to the pulse displacement is frequency dependent. Hence, a separate calibration curve may be required for each frequency. Moreover, some frequencies may capture more details than others. Figure 5-14 shows the waveform obtained at different frequencies; 60.34 GHz (30th sample), 60.5 GHz (32nd sample), and 62.6 GHz (59th sample). Although the 30th and 32nd samples are very close, they offered distinctly different-looking waveforms. The 59th sample, on the other hand, had a negative responsivity with the skin displacement causing the amplitude to decrease. More information is required before a decision can be made on which frequency offers a more physiologically accurate waveform that would be a part of future studies.



(a)



(b)



(c)

Figure 5-14 The measured pulse waveform for PT#1 using three different samples at different frequencies; (a) 60.34/30, (b) 60.5/32, and (c) 62.6/59; GHz/Sample.

The final step is about addressing a limitation in the current design of the sensor which is its sensitivity to placement. As mentioned in the superstrate design, the length of the slot is around 1.5 mm. Moreover, the size of the artery is estimated to be less than 0.1 mm. Consequently, the sensing region is quite limited and hence, it is quite sensitive to alignment. Figure 5-15 shows a comparison between the response of the sensor between the different locations on the wrist. The locations were only a couple of millimeters apart, but we can see how the pulse signal disappears in the absence of proper alignment between the pulse and the sensing slot. However, it is possible to increase the footprint of the sensing area by using longer a slot, an array of cascaded slots, or another shape such as a complementary split ring resonator (CSRR).

Moreover, a possible solution is to create a feedback system where the user is alerted if the sensor needs re-alignment. This may be achieved using spectral analysis comparing the peak frequency with the expected range of 40 to 200 bpm.

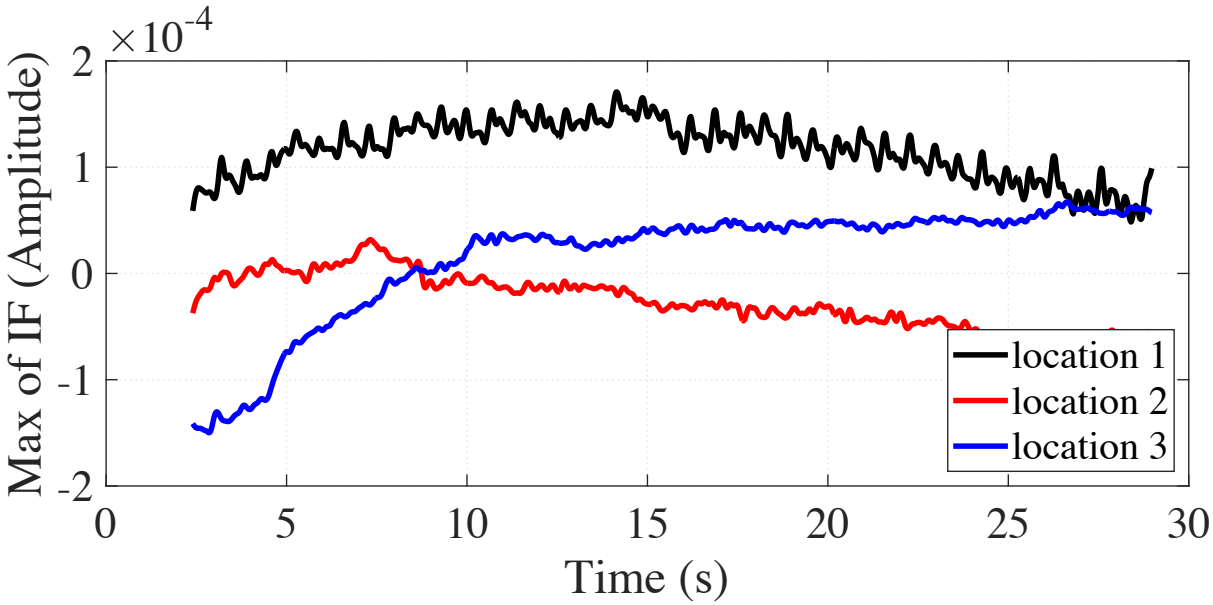


Figure 5-15 A comparison between the performance of the sensor at different locations on the wrist for PT#1.

5.2.3 Multiple Participant Study

The experiment was then repeated on 5 additional healthy participants. First, the participants are asked to wear the Frontier X ECG belt described in section 5.1.1 on their upper abdomen. Then the general location of the pulse on the participants' wrists was marked by using the two-

finger method [56] shown in Figure 5-16, where the radar module was placed with the slot of the superstrate facing the skin. The pulse was measured continuously for 60 seconds intervals, and the measurements were repeated three times, at slightly different locations on the wrist.

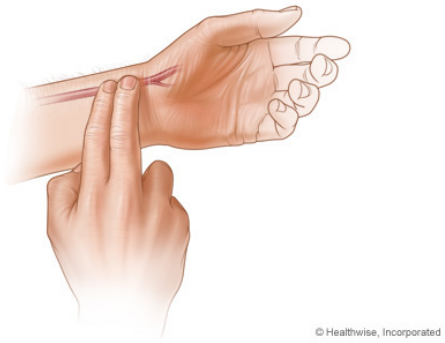


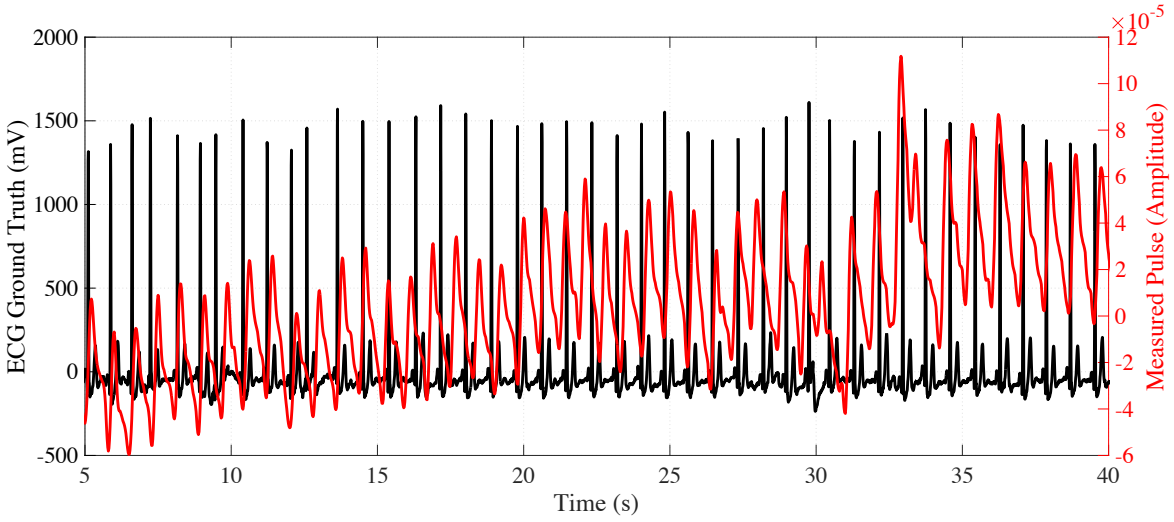
Figure 5-16 The two-finger technique used in locating the pulse on the wrist [56].

The measurements were then imported into MATLAB v.2023b and post-processed using the procedure described in section 5.2.2. Figure 5-17 (a) & (b) shows the results for PT#2, and PT#3 respectively. As observed in the results, the timing of the measured pulse was highly correlated with the timing of the corresponding ECG ground truth. Moreover, PT#2 had a very stable and consistent amplitude response throughout the measurement. Although PT#3 had some more variation over time which can be attributed to micromotions by the participant. Nonetheless, the pulse waveform was still distinctly detectable.

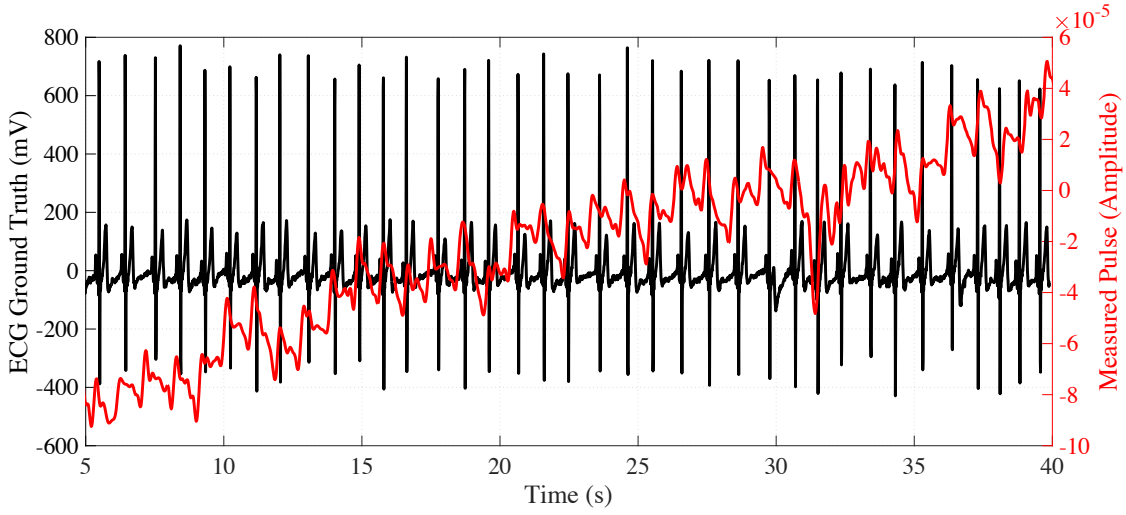
Using the built-in peak detection function in MATLAB v.2023b, we detected the R-wave peaks in the ECG signal measured by the Frontier X belt as shown in Figure 5-18a. Moreover, the systolic peaks of the measured pulse waveform were also detected as shown in Figure 5-18b. Then, the pulse interval was calculated by comparing the timing of the consecutive peaks in both the measurements and ground truth.

Table 5-2 presents a summary of the values of the measured heart rate interval and r-r intervals for participants 1-3. The error in the heart rate value obtained of the heart rate is less than 1.5% for all three participants. It is not realistic to expect the error to be zero, it is just that the 60s average heart rate was the same. However, there is an expected error in the durations of each pulse as shown in Figure 5-19 which shows a scatter plot inspired by the Bland-Altman statistical analyses [57] of the difference between the pulse interval and the r-r interval vs the

r-r interval for participants 2 and 3 (PT#2 & PT#3). This demonstrates there is still a realistic expectation of error in the timing of the individual pulses. However, this error can be averaged out when the pulse interval is averaged over a window of time. Hence, the size of the averaging window would cause dictate a natural trade-off between the throughput of the sensor, and error. It is also worth noting that there could be an error in the exact timing of the ECG results, hence, the values shown in Figure 5-19 are due to combined error.

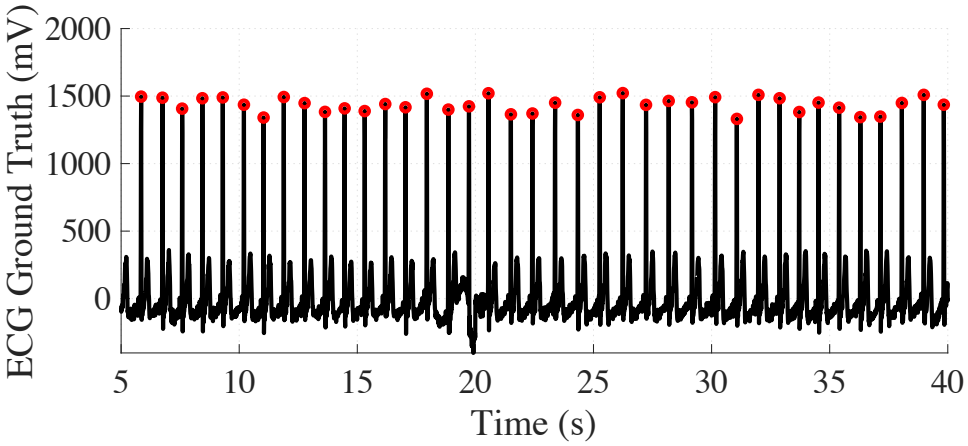


(a)

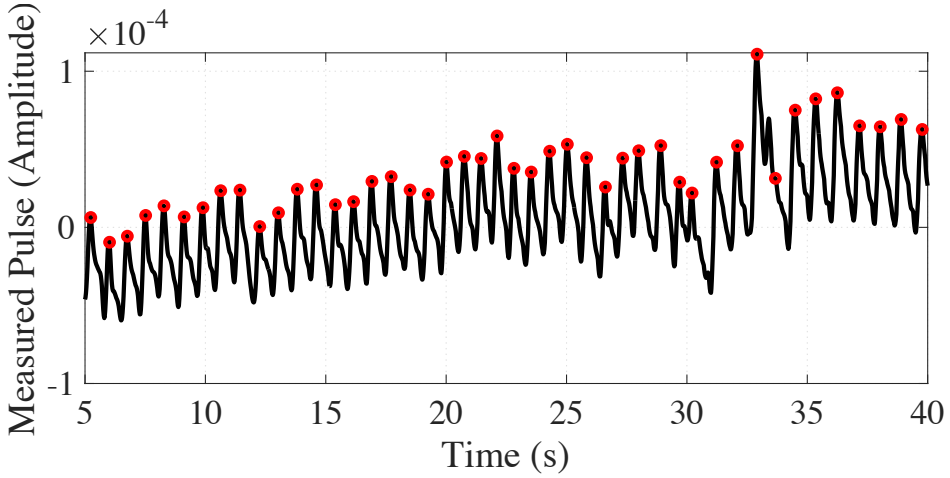


(b)

Figure 5-17 Measured pulse signal compared to the corresponding ECG ground truth for (a) PT#2, and (b) PT#3.



(a)



(b)

Figure 5-18 The detected peaks in the (a) ECG and (b) Pulse waveforms for PT#2.

Table 5-2 Summary of the heart rates obtained in the experiment.

Participant Number	Avg. Measured Pulse Interval (s)	Avg. ECG R-R Interval (s)	Heart Rate (Pulse/ECG) (bpm)	Error (%)
1	0.6833	0.6833	87.8/87.8	0
2	0.7828	0.7828	76.6/76.6	0
3	0.9627	0.9520	62.3/63	1.11

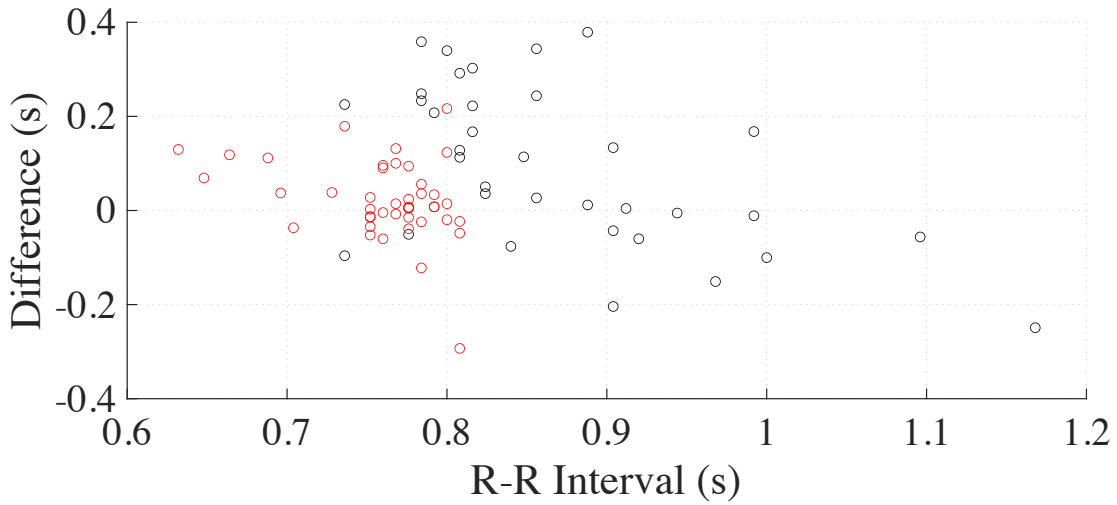


Figure 5-19 The error distribution of the measured pulse against its ECG benchmark for PT#2, and PT#3.

For the rest of the participants (PT#4-6), the measured pulse was very weak, hence, it had a very poor signal-to-noise ratio. This could be attributed to either a bad placement of the sensor relative to the location of the pulse as discussed in section 5.2.2 or a weak pulse of the participant. Another variable that was not investigated is the pressure applied on the skin of the participant, As the Velcro strap may not provide sufficient pressure for a good seal given the rigid geometry of the mounting bracket. An example of a poor signal-to-ratio measurement is for PT#4 shown in Figure 5-20 where the pulse waveform could be observed in some pulses (for example between t=31.5s and 35s). However, due to the small amplitude of the pulse signal, it gets dominated by the noise in most of the pulse cycles. As mentioned previously, it could be due to a small actual skin displacement or a misalignment.

There are two possible solutions for this problem; first, a more objective and deterministic method for placement may be required. Second, a flexible/conformal material could be used for the superstrate and/or mounting bracket which would allow a better fit and hence, an even mounting pressure according to the participant's wrist width and circumference.

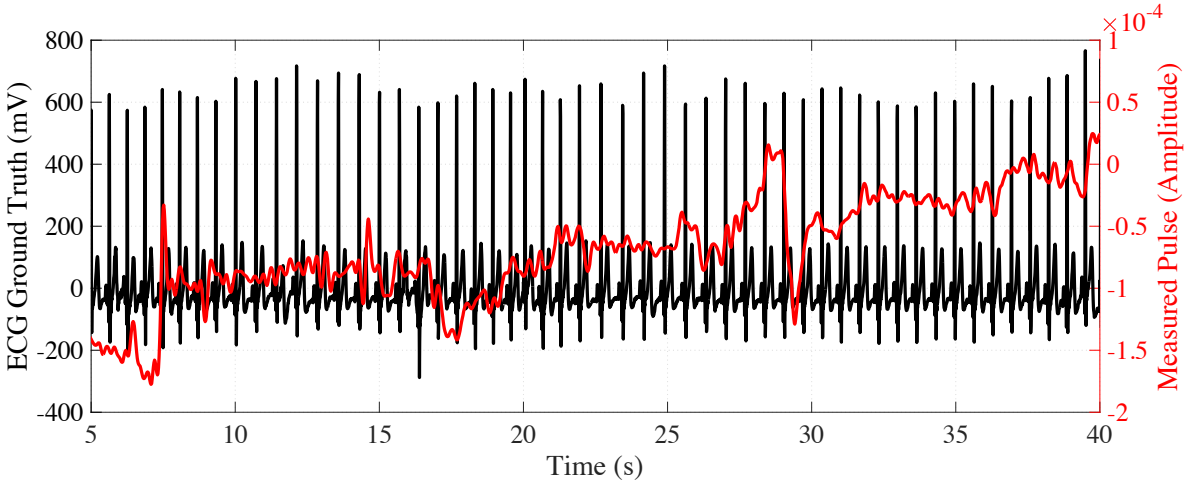


Figure 5-20 Measured pulse signal compared to the corresponding ECG ground truth for PT#4 as an example of a poor signal-to-noise ratio measurement.

Chapter 6

Conclusion & Future Work

6.1 Summary

This work proposes using a PCB superstrate as an add-on to an off-the-shelf commercial radar developed by Infineon for time-domain pulse sensing. The principle of operation of the superstrate is to couple the power from the transmitter through a microstrip line toward the designated receiver. The transmission coefficient of the microstrip line is perturbed by the movement of the pulse on the surface of the skin through the fringing fields of a defective ground structure, hence, changes in the power level of the received signal could be correlated to the pulse signal. A prototype was fabricated and tested on a human participant. The obtained pulse waveforms resembled the expected shape of the typical PPG waveform. Moreover, there is a very high correlation between the measured signal and the ECG ground truth. Moreover, this thesis also presents a numerical-based model to map the output of Commercial EM CAD tools (Ansys HFSS) to a radar's output. Thus, enabling us to accurately predict the response of the radar in the presence of near-field objects.

Additionally, this work provided a proof-of-concept for using highly efficient simulation methods such as SBR+ in generating digital twins for the problem of pulse sensing. The waveforms extracted from the output of the simulations accurately matched the input displacement waveforms despite the theoretically insufficient radar specifications.

6.2 Ongoing and Future Work

There are different aspects of how this work can inspire future work in this area. This work lays the foundation for using PCB-based microwave sensors with radars, to do this a simple sensor design was used as a proof-of-concept. However, the sensor design itself could be

optimized further for sensitivity by using more complex sensor designs such as ring resonators, and differential sensors. Moreover, there is the possibility of leveraging the multiple receiver channels used by the Infineon radar to gather more information by adding additional coupler ports to the superstrate.

Some challenges were highlighted in this work, including the optimum placement of the sensor and its effect on the sensing performance. An area of future work could be coming up with an objective and deterministic feedback system for an inexperienced user to place the sensor correctly. Moreover, the ergonomics of the sensor can be improved by using conformal/ flexible materials for the PCB, and mounting bracket so that it provides an even and comfortable pressure required for accurate measurements. An example of flexible 3D printing material is Thermoplastic Polyurethane (TPU) as it is soft and flexible while having high chemical stability. Moreover, flexible substrates have been commonly used in other high-frequency printed circuit boards.

Additionally, this sensor was tested on a limited number of healthy participants, and gathering more data from more participants including those suffering from cardiovascular illness is crucial for training robust machine learning models required for the detection of abnormalities in the pulse waveform.

Finally, microwave PCB sensors have been used in many other biomedical sensing applications, such as hydration or glucose sensing. The principle of this work could be applied to those applications, hence, improving the versatility of the technology.

6.3 Publications

1. **M. M. Y. R. Riad**, and G. Shaker, " Radar-Based Human Pulse Sensing Through a Resonator-Based Superstrate," Accepted for presentation at *2024 IEEE MTT-S International Microwave Biomedical Conference (IMBioC)*, Montreal, Canada, 2024.
2. **M. M. Y. R. Riad**, and G. Shaker, "Radar-based Human Pulse Sensing," Accepted for presentation at *2024 IEEE International Symposium on Antennas and Propagation and USNC-URSI Radio Science Meeting (APS/URSI*), Florence, Italy, 2024.

Other Publications within degree duration:

3. A. N. Sayed, **M. M. Y. R. Riad**, O. M. Ramahi and G. Shaker, "A Methodology for UAV Classification using Machine Learning and Full-Wave Electromagnetic Simulations," *2022 International Telecommunications Conference (ITC-Egypt)*, 2022, pp. 1-2, doi: 10.1109/ITC-Egypt55520.2022.9855753.
4. H. Abedi, S. Luo, V. Mazumdar, **M. M. Y. R. Riad,** and G. Shaker, "AI-Powered In-Vehicle Passenger Monitoring Using Low-Cost mm-Wave Radar," in *IEEE Access*, vol. 10, pp. 18998-19012, 2022, doi: 10.1109/ACCESS.2021.3138051.
5. A. Gharamohammadi, M. O. Bagheri, **M. M. Y. R. Riad**, S. Abu-Sardanah, H. Abedi, A. Ansariyan, K. Wang, A. Saragadam, D. Chumachenko, S. Abhari, P. P. Morita, A. Khajepour, and G. Shaker, "Smart Furniture Using Radar Technology for Cardiac Health Monitoring,", *Submitted to Nature Electronics*, 2024. (Under-Review)
6. A. N. Sayed, **M. M. Y. R. Riad**, A. Ansariyan, L. Salman, O. Ramahi, G. Shaker, "UAV Classification using Neural Networks and CAD-generated Radar Datasets.", 2024 (Under-Review)

References

[1] Y. Szekely *et al.*, "Cardiorespiratory Abnormalities in Patients Recovering from Coronavirus Disease 2019," *Journal of the American Society of Echocardiography*, vol. 34, no. 12, pp. 1273-1284.e9, Dec. 2021, doi: 10.1016/J.ECHO.2021.08.022.

[2] "Cardiovascular diseases (CVDs)." Accessed: Apr. 25, 2024. [Online]. Available: https://www.who.int/news-room/fact-sheets/detail/cardiovascular-diseases-%28cvds%29

[3] "World Heart Report 2023: Full Report - World Heart Federation." Accessed: Apr. 25, 2024. [Online]. Available: https://world-heart-federation.org/resource/world-heart-report-2023/

[4] "Heart Disease in Canada - Canada.ca." Accessed: Apr. 25, 2024. [Online]. Available: https://www.canada.ca/en/public-health/services/publications/diseases-conditions/heart-disease-canada.html

[5] M. Kebe, R. Gadhafi, B. Mohammad, M. Sanduleanu, H. Saleh, and M. Al-qutayri, "Human Vital Signs Detection Methods and Potential Using Radars: A Review," *Sensors 2020, Vol. 20, Page 1454*, vol. 20, no. 5, p. 1454, Mar. 2020, doi: 10.3390/S20051454.

[6] S. Abu-Sardanah, A. Gharamohammadi, O. M. Ramahi, and G. Shaker, "A Wearable Mm-Wave Radar Platform for Cardiorespiratory Monitoring," *IEEE Sens Lett*, 2023, doi: 10.1109/LSENS.2023.3277365.

[7] J. E. Johnson, O. Shay, C. Kim, and C. Liao, "Wearable Millimeter-Wave Device for Contactless Measurement of Arterial Pulses," *IEEE Trans Biomed Circuits Syst*, vol. 13, no. 6, pp. 1525–1534, Dec. 2019, doi: 10.1109/TBCAS.2019.2948581.

[8] N. Vysotskaya *et al.*, "Continuous Non-Invasive Blood Pressure Measurement Using 60 GHz-Radar—A Feasibility Study," *Sensors 2023, Vol. 23, Page 4111*, vol. 23, no. 8, p. 4111, Apr. 2023, doi: 10.3390/S23084111.

[9] A. E. Omer, G. Shaker, and S. Safavi-Naeini, "Portable Radar-Driven Microwave Sensor for Intermittent Glucose Levels Monitoring," *IEEE Sens Lett*, vol. 4, no. 5, May 2020, doi: 10.1109/LSENS.2020.2986208.

[10] M. M. Y. R. Riad and A. R. Eldamak, "Low-Cost Wi-Fi-based System Using Passive Microwave Sensors for Liquid Characterization," in *2021 28th IEEE International Conference on Electronics, Circuits, and Systems (ICECS)*, IEEE, 2021, pp. 1–4. doi: 10.1109/ICECS53924.2021.9665550.

[11] D. Mohrman and L. Heller, *Cardiovascular Physiology*, 9th ed. McGraw-Hill Education, 2018. Accessed: Dec. 24, 2023. [Online]. Available: https://accessmedicine.mhmedical.com/book.aspx?bookID=2432

[12] "12-Lead ECG Vs Single Lead ECG: The Superior Choice." Accessed: Mar. 08, 2024. [Online]. Available: https://www.tricog.com/12-lead-ecg-vs-single-lead-ecg/

[13] T. J. Hodgetts, G. Kenward, I. G. Vlachonikolis, S. Payne, and N. Castle, "The identification of risk factors for cardiac arrest and formulation of activation criteria to alert a medical emergency team," *Resuscitation*, vol. 54, no. 2, pp. 125–131, 2002, doi: 10.1016/S0300-9572(02)00100-4.

[14] C. Brüser, C. H. Antink, T. Wartzek, M. Walter, and S. Leonhardt, "Ambient and unobtrusive cardiorespiratory monitoring techniques," *IEEE Rev Biomed Eng*, vol. 8, pp. 30–43, 2015, doi: 10.1109/RBME.2015.2414661.

[15] R. L. Armentano and L. J. Cymberknop, "Pulse propagation in arteries," *Biomechanical Modeling of the Cardiovascular System*, pp. 8-1-8–22, Apr. 2019, doi: 10.1088/2053-2563/AAFB0DCH8.

[16] K. Kouz, T. W. L. Scheeren, D. De Backer, and B. Saugel, "Pulse Wave Analysis to Estimate Cardiac Output," *Anesthesiology*, vol. 134, no. 1, pp. 119–126, Jan. 2021, doi: 10.1097/ALN.0000000000003553.

[17] "VolumeView System | Edwards Lifesciences." Accessed: Mar. 08, 2024. [Online]. Available: https://www.edwards.com/gb/healthcare-professionals/products-services/hemodynamic-monitoring/volumeview

[18] "PiCCO • LITFL • CCC Equipment." Accessed: Mar. 08, 2024. [Online]. Available: https://litfl.com/picco/

[19] S. N. Myatra, N. R. Prabu, J. V. DIvatia, X. Monnet, A. P. Kulkarni, and J. L. Teboul, "The Changes in Pulse Pressure Variation or Stroke Volume Variation After a 'Tidal Volume Challenge' Reliably Predict Fluid Responsiveness During Low Tidal Volume Ventilation," *Crit Care Med*, vol. 45, no. 3, pp. 415–421, Mar. 2017, doi: 10.1097/CCM.0000000000002183.

[20] D. Zhang, W. Zuo, and P. Wang, "Comparison Between Pulse and ECG," *Computational Pulse Signal Analysis*, pp. 301–318, 2018, doi: 10.1007/978-981-10-4044-3_16.

[21] "CardieX - Home." Accessed: Mar. 08, 2024. [Online]. Available: https://cardiex.com/

[22] A. Davies and A. Scott, *Starting to Read ECGs*. Springer London, 2013. doi: 10.1007/978-1-4471-4962-0.

[23] Y. Wu, H. Ni, C. Mao, J. Han, and W. Xu, "Non-intrusive Human Vital Sign Detection Using mmWave Sensing Technologies: A Review," *ACM Trans Sens Netw*, vol. 20, no. 1, Nov. 2023, doi: 10.1145/3627161.

[24] F. Wang, X. Zeng, C. Wu, B. Wang, and K. J. R. Liu, "Driver Vital Signs Monitoring Using Millimeter Wave Radio," *IEEE Internet Things J*, vol. 9, no. 13, pp. 11283–11298, Jul. 2022, doi: 10.1109/JIOT.2021.3128548.

[25] X. Zhang, X. Yang, Y. Ding, Y. Wang, J. Zhou, and L. Zhang, "Contactless Simultaneous Breathing and Heart Rate Detections in Physical Activity Using IR-UWB Radars," *Sensors 2021, Vol. 21, Page 5503*, vol. 21, no. 16, p. 5503, Aug. 2021, doi: 10.3390/S21165503.

[26] F. Wang, F. Zhang, C. Wu, B. Wang, and K. J. R. Liu, "ViMo: Multiperson Vital Sign Monitoring Using Commodity Millimeter-Wave Radio," *IEEE Internet Things J*, vol. 8, no. 3, pp. 1294–1307, Feb. 2021, doi: 10.1109/JIOT.2020.3004046.

[27] D. Zhang, Y. Hu, and Y. Chen, "MTrack: Tracking Multiperson Moving Trajectories and Vital Signs with Radio Signals," *IEEE Internet Things J*, vol. 8, no. 5, pp. 3904–3914, Mar. 2021, doi: 10.1109/JIOT.2020.3025820.

[28] S. Abu-Sardanah, "Cardio-respiratory Health Monitoring Using a Wearable Radar System," Sep. 2023, Accessed: Mar. 10, 2024. [Online]. Available: https://uwspace.uwaterloo.ca/handle/10012/19857

[29] "BGT60TR13C | XENSIV™ 60GHz radar sensor for advanced sensing - Infineon Technologies." Accessed: Oct. 02, 2022. [Online]. Available: https://www.infineon.com/cms/en/product/sensor/radar-sensors/radar-sensors-for-iot/60ghz-radar/bgt60tr13c/

[30] "Ansys HFSS | 3D High Frequency Simulation Software." Accessed: Jul. 06, 2023. [Online]. Available: https://www.ansys.com/products/electronics/ansys-hfss

[31] "Home: Soli." Accessed: Jul. 06, 2023. [Online]. Available: https://atap.google.com/soli/

[32] C. Liao, O. Shay, E. Gomes, and N. Bikhchandani, "Noninvasive continuous blood pressure measurement with wearable millimeter wave device," *2021 IEEE 17th International Conference on Wearable and Implantable Body Sensor Networks, BSN 2021*, vol. 2021-January, Jul. 2021, doi: 10.1109/BSN51625.2021.9507020.

[33] "Yole Group - Follow the latest trend news in the Semiconductor Industry." Accessed: Jul. 06, 2023. [Online]. Available: https://www.yolegroup.com/product/report/infineons-radar-technology-and-knowles-machine-learning-drive-google-pixel-4xl-gesture-recognition/

[34] P. Velez, J. Munoz-Enano, K. Grenier, J. Mata-Contreras, D. Dubuc, and F. Martin, "Split Ring Resonator-Based Microwave Fluidic Sensors for Electrolyte Concentration Measurements," *IEEE Sens J*, vol. 19, no. 7, pp. 2562–2569, Apr. 2019, doi: 10.1109/JSEN.2018.2890089.

[35] A. M. Albishi and O. M. Ramahi, "Highly Sensitive Microwaves Sensors for Fluid Concentration Measurements," *IEEE Microwave and Wireless Components Letters*, vol. 28, no. 4, pp. 287–289, Apr. 2018, doi: 10.1109/LMWC.2018.2805866.

[36] N. Chahat, M. Zhadobov, R. Augustine, and R. Sauleau, "Human skin permittivity models for millimetre-wave range," *Electron Lett*, vol. 47, no. 7, pp. 427–428, Mar. 2011, doi: 10.1049/EL.2011.0349.

[37] T. Wu, T. S. Rappaport, and C. M. Collins, "The human body and millimeter-wave wireless communication systems: Interactions and implications," *IEEE International Conference on Communications*, vol. 2015-September, pp. 2423–2429, Sep. 2015, doi: 10.1109/ICC.2015.7248688.

[38] M. Maeda, "An Analysis of Gap in Microstrip Transmission Lines," *IEEE Trans Microw Theory Tech*, vol. 20, no. 6, pp. 390–396, 1972, doi: 10.1109/TMTT.1972.1127768.

[39] M. M. Y. R. Riad, M. A. Ateyya, A. R. Eldamak, and A. M. E. Safwat, "Highly Sensitive Bi-Transmission Line-based Sensors for Liquid Characterization," *2023 International Microwave and Antenna Symposium, IMAS 2023*, pp. 203–206, 2023, doi: 10.1109/IMAS55807.2023.10066907.

[40] A. N. Sayed, M. M. Y. R. Riad, O. M. Ramahi, and G. Shaker, "A Methodology for UAV Classification using Machine Learning and Full-Wave Electromagnetic Simulations," *International Telecommunications Conference, ITC-Egypt 2022 - Proceedings*, 2022, doi: 10.1109/ITC-EGYPT55520.2022.9855753.

[41] A. N. Sayed, M. M. Y. R. Riad, O. M. Ramahi, and G. Shaker, "UAV Classification using Neural Networks and CAD-generated Radar Datasets," Jun. 2022, doi: 10.36227/TECHRXIV.20085920.V1.

[42] "BGT60TR13C | XENSIV™ 60GHz radar sensor for advanced sensing - Infineon Technologies." Accessed: Jul. 26, 2023. [Online]. Available: https://www.infineon.com/cms/en/product/sensor/radar-sensors/radar-sensors-for-iot/60ghz-radar/bgt60tr13c/

[43] J. Johnson, C. Kim, and O. Shay, "Arterial pulse measurement with wearable millimeter wave device," *2019 IEEE 16th International Conference on Wearable and Implantable Body Sensor Networks, BSN 2019 - Proceedings*, May 2019, doi: 10.1109/BSN.2019.8771037.

[44] "Third version of homemade 6 GHz FMCW radar - Henrik's Blog." Accessed: Feb. 24, 2024. [Online]. Available: https://hforsten.com/third-version-of-homemade-6-ghz-fmcw-radar.html

[45] C. McCormack *et al.*, "Pulmonary hypertension and home-based (PHAHB) exercise intervention: Protocol for a feasibility study," *BMJ Open*, vol. 11, no. 5, p. e045460, May 2021, doi: 10.1136/BMJOPEN-2020-045460.

[46] "CNAP® Blood Pressure - CNSystems Medizintechnik GmbH." Accessed: Mar. 14, 2024. [Online]. Available: https://www.cnsystems.com/technology/cnap-blood-pressure/#

[47] "Frontier X2 Smart Heart Monitor | Real Time Wearable Heart Rate Monitor | Continuous ECG Chest Strap - Fourth Frontier Technologies LLC." Accessed: Dec. 22, 2023. [Online]. Available: https://fourthfrontier.com/products/frontier-x

[48] F. Shaffer and J. P. Ginsberg, "An Overview of Heart Rate Variability Metrics and Norms," *Front Public Health*, vol. 5, p. 258, Sep. 2017, doi: 10.3389/FPUBH.2017.00258.

[49] "File:Ecg.png - Wikimedia Commons." Accessed: Dec. 24, 2023. [Online]. Available: https://commons.wikimedia.org/wiki/File:Ecg.png

[50] "Radar Fusion GUI - Infineon Developer Center." Accessed: Feb. 02, 2024. [Online]. Available: https://softwaretools.infineon.com/tools/com.ifx.tb.tool.radarfusiongui

[51] A. R. Levin, M. Frand, and H. A. Baltaxe, "Left Atrial Enlargement," *Radiology*, vol. 104, no. 3, pp. 615–621, Jul. 2023, doi: 10.1148/104.3.615.

[52] K. S. Heffernan, A. G. Kasprowicz, B. J. Tarzia, J. E. Davies, and D. P. Casey, "Sex Differences in Peripheral Augmentation Index and Arterial Reservoir Pressure during Upper Limb Postural Shifts," *Physiol J*, vol. 2014, pp. 1–10, Jan. 2014, doi: 10.1155/2014/971906.

[53] "Left Atrial Enlargement • LITFL Medical Blog • ECG Library Basics." Accessed: Mar. 10, 2024. [Online]. Available: https://litfl.com/left-atrial-enlargement-ecg-library/

[54] J. Hashimoto *et al.*, "Enhanced radial late systolic pressure augmentation in hypertensive patients with left ventricular hypertrophy," *Am J Hypertens*, vol. 19, no. 1, pp. 27–32, Jan. 2006, doi: 10.1016/J.AMJHYPER.2005.06.017/2/.

[55] J. T. Kühl *et al.*, "Left ventricular hypertrophy identified by cardiac computed tomography and ECG in hypertensive individuals: A population-based study," *J Hypertens*, vol. 37, no. 4, pp. 739–746, Apr. 2019, doi: 10.1097/HJH.0000000000001962.

[56] "Taking a Pulse (Heart Rate)." Accessed: Apr. 11, 2024. [Online]. Available: https://myhealth.alberta.ca/Health/pages/conditions.aspx?hwid=hw201445

[57] J. Martin Bland and D. G. Altman, “Statistical Methods for Assessing Agreement Between Two Methods of Clinical Measurement,” *The Lancet*, vol. 327, no. 8476, pp. 307–310, Feb. 1986, doi: 10.1016/S0140-6736(86)90837-8.

Appendices

Appendix A: MATLAB Scripts

In this appendix, we present the portions of the work that were conducted using MATLAB scripts.

SBR+ Waveform Reconstruction

```
% Import data from the file exported from HFSS
fileData =
importfile_SBR_Velocity("../Heart_doppler_velocity_10_cycles.csv", [2,
Inf]);

% Calculate the number of time points, maximum time
numVelocityPoints= 64;
numTimePoints = length(fileData(:, 3)) / numVelocityPoints;
maxTime = max(fileData(:, 1));
timePerStep = maxTime / numTimePoints;

% Reshape the data into a matrix
powerData = reshape(fileData(:, 3), numTimePoints, numVelocityPoints);

% Create a surface plot of the power data
surf(powerData, "EdgeColor", "none")
ylabel("Time Samples")
xlabel("DopplerVelocity Samples")
zlabel("Power (dB)")
figure

% Generate a contour plot of the power data with a specified number of
contours
numContours = 10;
contourMatrix = contour(powerData', numContours);
xticks(0:100:1000)
yticks(0:10:64)
xlabel("Time Samples")
ylabel("DopplerVelocity Samples")
figure

% Extract the x-values and contours from the contour plot and store them
in separate matrices

%Calculating size of countour vectors
x1 = find(contourMatrix(1, :) == 1);
x2 = find(contourMatrix(1, :) == numTimePoints);

%Intilizaing Variables

xValues = NaN(2000, numContours * 2);
contours = NaN(2000, numContours * 2);
```

```
for i = 1:numContours * 2
    if floor(i / 2) == i / 2
       xValues(1:x1(i) - x2(i) + 1, i) = timePerStep * flip(contourMatrix(1,
x2(i):x1(i)))';
        contours(1:x1(i)  -  x2(i)  +  1,  i)  =  flip(contourMatrix(2,
x2(i):x1(i)))';
    else
        xValues(1:x2(i) - x1(i) + 1, i) = timePerStep * contourMatrix(1,
x1(i):x2(i))';
        contours(1:x2(i) - x1(i) + 1, i) = (contourMatrix(2, x1(i):x2(i)))';
    end
end

% Calculate the velocity by selecting a column of the contours matrix and
removing any NaN values
Select_countour_number = 1;
velocity = contours(:, Select_countour_number);
firstNaNIndex = find(isnan(velocity));
xValuesNoDC = xValues(1:firstNaNIndex(1) - 1,Select_countour_number);


% Perform a Fourier transform on the velocity data, remove the DC
component, and perform an inverse Fourier transform to obtain the velocity
without the DC component
velocityFFT = fft(velocity(1:firstNaNIndex(1) - 1));
velocityFFT(1) = 0;
velocityFFT(end) = 0;
velocityNoDC = real(ifft(velocityFFT));

% Fit the velocity data to a two harmonic sine function using a custom
function named "Fit_to_sines" and evaluate the fitted function to obtain
the velocity fit
[velocityCoefficients, goodnessOfFit] = Fit_to_sines(xValuesNoDC,
velocityNoDC);
velocityFit = feval(velocityCoefficients, xValuesNoDC);

% Calculate the displacement by integrating the velocity fit using the
cumulative trapezoidal rule
displacement = cumtrapz(xValuesNoDC, velocityFit);
displacement = displacement - min(displacement);

% Generate plots of the velocity fit and displacement
plot(xValuesNoDC, velocityFit)
xlabel("Time (s)")
ylabel("Velocity (a.u.)")
figure
plot(xValuesNoDC, (displacement))
xlabel("Time (s)")
ylabel("Displacement (a.u.)")
```

```
% Save all open figures in EPS format using a for loop. Each figure is
saved to a separate file with a filename that includes the figure number.
figs = findobj('Type', 'figure'); % find all open figures
for k = 1:length(figs)
    filename = sprintf('figure%d.eps', k); % create a filename for each
figure
    print(figs(k), '-depsc', filename); % print each figure to a separate
EPS file
end
```

Numerical-Based Simulations

Function to import S-parameters

```
function SReflect = importing_S_param(name)
filepath= strcat('D:\Users\!m6riad\OneDrive - University of
Waterloo\Documents\Ansoft\',name,'.csv');
direct_import = importfile(filepath, [2, Inf]);
Complex_import=direct_import(:,1).*exp(-1i*(direct_import(:,2))*pi/180);
SReflect= (Complex_import');
End
```

Function to calculate the required property

```
function [xaxes,result] = Calculate(xaxes_name,result_name,name)

%% Radar Properties
n_frames=1;
n_chirp_frame=4;
n_chirp=n_frames*n_chirp_frame;
t_chirp=64e-6;
f1=57.5e9;
f2=62.5e9;
fs=140e9;


%% frame generation
t=0:1/fs:(n_chirp*t_chirp+(n_chirp-1)/fs);
f=0:1/(n_chirp*t_chirp+(n_chirp-1)/fs):fs;
size_f=size(f);
t2=0:1/fs:t_chirp;
T_t=zeros(size(t));
T_t(1:length(t2))=chirp(t2,f1,t_chirp,f2);
T_f=fft(T_t)./length(T_t);
f2=f(1:end/2);
clear t2 f
f=f2;
xaxes=eval(xaxes_name);
```

```
clear t f

%% Get S-parameters
SReflect=importing_S_param(name);
SReflect_interp = interp1(SReflect(1,:), SReflect(2,:), f2, 'linear',
'extrap');
clear SReflect

%% Calculate Received Signal
if(ismember(result_name, ["IF_t" , "IF_f" , "R_t" , "R_f"]))
    R_f=zeros(size_f);
    R_f(1:end/2)= T_f(1:end/2).*conj((flip(SReflect_interp)));
    R_f(end/2+1:end)= T_f(1+end/2:end).*SReflect_interp;
    clear SReflect_interp T_f
    R_t=(real(ifft(R_f))).*length(R_f);
end

if(ismember(result_name, ["IF_t" , "IF_f"]))
    %% Calculate IF signal
    clear R_f
    IF_t= R_t.*T_t;
    clear R_t T_t
    IF_f= fft(IF_t)./length(IF_t);
end

%% return required property
result=eval(result_name);

end
```

Main script with user input

```
% Close all open figures
close all

% Clear all variables from the workspace
clear all

%% Specify Y-axes
% Define the result property
result_property="R_t";

% Check if the result property is in the specified list
if(ismember(result_property, ["T_f" , "R_f" , "IF_f"]))
    % If it is frequency domain, set the axes property and plot type
accordingly
    axes_property="f";
    plot_type= "2D";
else
    % If it is timedomain, set different axes property and plot type
    axes_property="t";
    plot_type= "Spectrogram";
```

```
end

%% File Range
% Define the vector of file names to process
file_names=["S21_WG_Circuit"];

%% Extract loop
% Loop over each file in the name vector
for i=1:length(file_names)
    % Calculate the axes and result values for the current file

[x_axes,result]=Calculate(axes_property,result_property,file_names(i));

    %% Data Plot
    % Check the plot type
    if(plot_type=="2D")
        % If it's a 2D plot, create a new figure and plot the data
        figure;
        plot(x_axes/1e9, abs(result));
        % Label the y-axis with the result property and units
        ylabel(strcat(result_property," (Amplitude)"))
        % Label the x-axis with frequency in GHz
        xlabel("Frequency (GHz)")
    end

    if(plot_type=="Spectrogram")
       % If it's a spectrogram, set up parameters for the spectrogram
function
       windowlength = 1000;
       noverlap = 100;
       nfft = 10000;
       fs=140e9;
       % Generate and display the spectrogram of the result data

spectrogram((result),windowlength,noverlap,nfft,fs,'reassigned','MinThresh
old', -120 ,'yaxis')
       % Set y-axis limits for the spectrogram display
       ylim([50 70])
    end

end
```

Measurements post-processing

```
% Clear all figures
close all;

%% Initialization and variable definitions
num_chirps_per_frame = 64; % Number of chirps per frame
num_frames = 300; % Number of frames
num_samples_per_chirp = 64; % Number of samples per chirp
chirp_repetition_time_s = 0.0004362; % Chirp repetition time in seconds
```

```
nfft = 256; % Number of points in the FFT

%% Time and Frequency Vectors
total_samples = num_frames * num_chirps_per_frame * num_samples_per_chirp;
% Total number of samples
time_between_samples = chirp_repetition_time_s / num_samples_per_chirp; %
Time between samples
time_vector = 0:time_between_samples:(total_samples*time_between_samples -
time_between_samples); % Time vector
time = time_vector(1:64); % Time vector for one chirp
f = 0:1/(nfft*time_between_samples):1/time_between_samples-
(1/(nfft*time_between_samples)); % Frequency vector
clearvars total_samples time_between_samples time_vector % Clear
unnecessary variables

%% Import and segment data
allData = textread('Repeat_right_wrist_loc2(2).raw.txt', '%s',
'delimiter', '\\n'); % Read data from file
numericalArray = cellfun(@(s) sscanf(s,'%f').', allData, 'un', 0); %
Convert string data to numerical array
header = allData(cellfun('isempty',numericalArray)); % Extract header
information
data = vertcat(numericalArray{:}); % Combine all numerical data into one
array
Chirps = reshape(data,[],num_chirps_per_frame,num_frames); % Reshape data
into a 3D array (Chirps)
clearvars allData numericalArray header data % Clear unnecessary variables

%% Remove Mean and Calculate IF Spectrum
Chirps_no_mean = Chirps - mean(Chirps,1); % Remove the mean from the data
IF_spectrum =
(fft(Chirps_no_mean(:,:,:).*hamming(num_samples_per_chirp),nfft))/nfft; %
Calculate the IF spectrum
clearvars Chirps_no_mean % Clear unnecessary variables

%% Sweep over frames and Chirps to plot figures
counter = 1; % Initialize counter
figure; % Create new figure
for i = 1:num_frames
    for j = 1:num_chirps_per_frame
        plot(f(1:end/2)/1e9,abs(IF_spectrum(1:end/2,j,i))); % Plot the IF
spectrum
        xlabel("Frequency (GHz)")
        ylabel("IF (Amplitude)")
        legend("Data on skin")
        [maxi(counter), maxi_index] = max(abs(IF_spectrum(1:end/2,j,i)));
% Find the maximum of the IF spectrum
        counter = counter + 1; % Increment the counter
        pause(1)
    end
end

%% Resample and interpolate the maximum IF spectrum
```

```
time_frames = 0:0.1:30-0.1; % Create time vector for the frames
resampled_max = -1*resample(maxi,1,64) + mean(resample(maxi,1,64)); %
Resample the maximum IF spectrum
resampled_max_interp = interp(resampled_max(100:200),5); % Interpolate the
resampled maximum IF spectrum
time_frames_interp = interp(time_frames(100:200),5); % Interpolate the
time frames
figure; % Create new figure
plot(time_frames_interp,resampled_max_interp) % Plot the interpolated
maximum IF spectrum
xlim([10 20])
xlabel("Time (s)")
ylabel("Max of IF (Amplitude)")

%% Calculate and plot the spectrum of the interpolated maximum IF spectrum
f_frames_interp = (0:length(time_frames_interp)-
1)/(length(time_frames_interp)*(time_frames_interp(2) -
time_frames_interp(1))); % Create the frequency vector
spectrum = abs(fft(resampled_max_interp))/length(resampled_max_interp); %
Calculate the spectrum of the interpolated maximum IF spectrum
figure; % Create new figure
plot(f_frames_interp(1:end/2),spectrum(1:end/2)) % Plot the spectrum
xlabel("Frequency (Hz)")
ylabel("Pulse Spectrum (Amplitude)")
xlim([0 25])

%% Import ECG DATA Seperately
% import the data from parse ECG folder as numeric vectors
pulse_segment = Pulse303030045154(12501:13751,2); % Extract pulse segment
time_segment = Pulse303030045154(12501:13751,1); % Extract time segment
time_segment = time_segment - 100 + 10; % Adjust time segment
plot(time_segment,pulse_segment) % Plot ECG ground truth
ylabel("ECG Ground Truth (mV)")
yyaxis right
plot(time_frames_interp,resampled_max_interp) % Plot measured pulse
ylabel("Measured Pulse (Amplitude)")
xlim([10 20])
xlabel("Time (s)")
```